Simulations of Critical Currents in Polycrystalline Superconductors Using Time-Dependent Ginzburg–Landau Theory

BLAIR, ALEXANDER,IAN

BLAIR, ALEXANDER,IAN (2021) *Simulations of Critical Currents in Polycrystalline Superconductors Using Time-Dependent Ginzburg–Landau Theory*, Durham theses, Durham University. Available at Durham E-Theses Online: http://etheses.dur.ac.uk/13993/

Simulations of Critical Currents in Polycrystalline Superconductors Using Time-Dependent Ginzburg–Landau Theory

Alexander Ian Blair

A thesis presented for the degree of
Doctor of Philosophy

Department of Physics
Durham University
United Kingdom
4th May 2021

To my parents.

Simulations of Critical Currents in Polycrystalline Superconductors Using Time-Dependent Ginzburg–Landau Theory

Alexander Ian Blair

Abstract

In this thesis, we investigate the in-field critical current density $J_\mathrm{c}(B)$ of polycrystalline superconducting systems with grain boundaries modelled as Josephson-type planar defects, both analytically and through computational time-dependent Ginzburg–Landau (TDGL) simulations in 2D and 3D. For very narrow SNS Josephson junctions (JJs), with widths smaller than the superconducting coherence length, we derive what to our knowledge are the first analytic expressions for $J_\mathrm{c}(B)$ across a JJ over the entire applied magnetic field range. We extend the validity of our analytic expressions to describe wider junctions and confirm them using TDGL simulations. We model superconducting systems containing grain boundaries as a network of JJs by using large-scale 3D TDGL simulations applying state-of-the-art solvers implemented on GPU architectures. These simulations of $J_\mathrm{c}(B)$ have similar magnitudes and dependencies on applied magnetic field to those observed experimentally in optimised commercial superconductors. They provide an explanation for the $B^{-0.6}$ dependence found for $J_\mathrm{c}(B)$ in high temperature superconductors and are the first to correctly provide the inverse power-law grain size behaviour as well as the Kramer field dependence, widely found in many low temperature superconductors.

Supervisors: Prof. Damian Hampshire and Prof. Ray Sharples

Acknowledgements

I first wish to thank my supervisor, Prof. Damian Hampshire, for all the guidance and support he has given me over my time at Durham, with regards to both my research and my broader professional development. I also wish to thank all of the other members of Durham University Superconductivity Group that I have had the pleasure of working alongside over the course of my Ph.D. studies; Mark Raine, Yeekin Tsui, Guanmei (Mona) Wang, Paul Branch, Francis Ridgeon, Jack Greenwood, Andrew Smith, Simon Chislett-McDonald, Adel Nader, Charles Gurnham, and Brad Din, for all the lively office conversations we have shared about superconductivity, life, and current affairs. Whilst every one of them has been an irreplaceable part of my Ph.D. journey, I wish to extend particular thanks to Mark Raine, for his level-headed outlook and for all I have learned from our many diverse discussions; and to Paul Branch, for being an enthusiastic teammate at outreach events, and for his friendship and support over the years.

In addition, I wish to thank all those involved with the Fusion Centre for Doctoral Training (CDT). The opportunities and courses provided within the CDT were a highlight of my Ph.D. programme, and it has been a privilege to be part of a cohort of such remarkable individuals from different research fields. I cannot hope to list here every individual in the CDT with whom I have shared invaluable conversations about research frontiers in fusion, for the list is too long. However, I do wish to extend a special thanks to Sam Ward, for his enlightening discussions about CUDA programming for GPU simulation that laid the foundations for the implementation of the large-scale 3D vortex dynamics solver used in this work. I also wish to thank Dr. Chengtian Lin and all other members of the Crystal Growth Group and Thin Film Laboratory at the Max Plank Institute for Solid State Research in Stuttgart, Germany, for their kind hospitality and tutelage during my CDT collaboratory project that took place there.

On a personal level, I would like to offer thanks to the Graduate Common Room of Ustinov College, and to all the friends I have made during my time involved with it. The peer support of its postgraduate community has been the emotional bedrock on which this work has been completed, and conversations shared there have broadened my horizons immeasurably. I am particularly grateful to Samantha Franks, for her boundless optimism, enthusiasm, and care over the last few years, and for all the adventures we have shared together over that time! Finally, I would like to thank my parents, Ian and Teresa Blair, for their love and support throughout my studies. I am sincerely grateful for all their positivity and encouragement during all the highs and lows of this project, and for all their reminders to see the light at the end of the tunnel!

This work is funded by EPSRC grant EP/L01663X/1 that supports the EPSRC Centre for Doctoral Training in the Science and Technology of Fusion Energy. This work has also been carried out within the framework of the EUROfusion Consortium and has received funding from the Euratom research and training programme. Computational work in this thesis made use of the facilities of the Hamilton HPC Service and the NVIDIA CUDA Centre (NCC) of Durham University.

Contents

Declaration

The work in this thesis is based on research carried out at Durham University Superconductivity Group, Department of Physics, University of Durham, England. No part of this thesis has been submitted elsewhere for any other degree or qualification, and it is the sole work of the author unless referenced to the contrary in the text.

Some of the work presented in this thesis has been previously published in journals and presented at conferences - the relevant publications and conferences are listed below.

Publications

Modeling the Critical Current of Polycrystalline Superconducting Films in High Magnetic Fields, Blair, A. I. and Hampshire, D. P.; *IEEE Trans. Appl. Supercond.* **29**(5): 1 (2019)

Time-Dependent Ginzburg–Landau Simulations of the Critical Current in Superconducting Films and Junctions in Magnetic Fields, Blair, A. I. and Hampshire, D. P.; *IEEE Trans. Appl. Supercond.* **28**(4): 1 (2018)

Conference Presentations

Ginzburg–Landau Critical Currents in High Fields for Polycrystalline Superconductors (Oral), Blair, A. I. and Hampshire, D. P.; EUCAS 2019, Glasgow, UK (2019)

Modelling the Critical Current of Surfaces and Grain Boundaries in Superconducting Films at High Magnetic Fields (Poster), Blair, A. I. and Hampshire, D. P.; ASC 2018, Seattle, WA, USA (2018)

Modelling Superconductors for Fusion Applications using Ginzburg–Landau Theory (Poster), Blair, A. I. and Hampshire, D. P.; KSTAR Conference, Muju, KR (2018)

Measuring and Modelling High Magnetic Field Superconductors for Fusion Applications (Oral), Blair, A. I. et al.; NFRI, Daejeon, KR (2018)

Time-Dependent Ginzburg–Landau Simulations of the Critical Current in Superconducting Films and Junctions in Magnetic Fields (Poster), Blair, A. I. and Hampshire, D. P.; EuCAS 2017, Geneva, CH (2017)

Modelling Superconductors for Fusion Applications (Poster), Blair, A. I., Greenwood, J. R., Smith, A. and Hampshire, D. P.; Joint Nuclear CDT Conference, York, UK (2017)

Calculating the Supercurrent Across Grain Boundaries using Ginzburg–Landau Theory (Poster), Blair, A. I. and Hampshire, D. P.; Applied Superconductivity Conference, Denver, CO, USA (2016)

Modelling the Critical Current of Technological Superconductors in High Magnetic Fields (Poster), Blair, A. I. and Hampshire, D. P.; Fusion Frontiers and Interfaces Conference, York, UK (2016)

4th May 2021

Alexander Ian Blair

Courses

As part of the funding conditions for this Ph.D. project, the author is a student on the “Materials Strand” of the EPSRC Centre for Doctoral Training in the Science and Technology of Fusion Energy, hereafter referred to as the “Fusion CDT”. The Fusion CDT comprises of a collaboration of five UK universities; the University of York, the University of Oxford, the University of Manchester, the University of Liverpool and the University of Durham, along with a number of industrial partners and research institutes such as Culham Centre for Fusion Energy (CCFE), ITER, and Fusion for Energy. Its primary purpose is to provide training in fusion energy for Ph.D. candidates in related disciplines through a series of modules located at member universities. The course of Fusion CDT modules is designed to be full-time for the first academic year of study, comprising of around 9 months of full-time work concluding in mid-June. To accommodate the extra time required to complete the first year modules, Ph.D. projects within the Fusion CDT are funded for 4 years. An outline of the first year courses in the Fusion CDT is provided in Table 1.

In the second year, students plan and take part in a funded collaboratory research project for up to ten weeks at an institution of their choice, which may be outside the UK. For this, the author completed an eight week collaboratory project under the supervision of Dr. Chengtian Lin in the Crystal Growth Group of the Max Planck Institute for Solid State Research in Stuttgart, Germany, investigating surface effects on the upper critical fields of single crystal samples of YBCO, measuring the magnetic hysteresis of samples using a Quantum Design Magnetic Property Measurement System (MPMS).

Course Name	**Location**
Introduction to Plasma Physics	York
Introduction to Materials	York
Computational Techniques	York
High Performance Computing	York (Remote)
Materials Applications in Fusion	Oxford
Radiation Damage	Oxford
Fusion Technology	York
Plasma Surface Interactions	Liverpool
Analytical and Characterisation Techniques	Oxford and Manchester
Finite Element Method and Design Codes	Manchester
Integrated Systems and Project Management	Durham

Table 1: First year courses attended as part of the Fusion CDT.

Chapter 1

Introduction

1.1 Background

We live in an electric world. Today, modern society relies on the ability to manipulate and control the flow of electric currents to transmit power to our homes and make our everyday electronic devices function. However, the conventional conductors through which we carry these currents, like copper, generate heat when an electric current passes through them, due to their electrical resistance. Sometimes, resistance is desirable – for example, in the heating element of a kettle when boiling water. Usually, however, it is not, and the energy lost to heat is an undesirable waste of energy that could otherwise be used for useful work. The resistance of conventional conductors makes this heating inevitable, and limits the efficiency in practical applications.

However, in 1911, Kamerlingh Onnes made the remarkable observation that the resistance of metallic mercury dropped abruptly to immeasurably low values when cooled below a critical temperature of 4.2 K [1]. It would later be understood that this was the first observation of the superconducting state, and mercury would become the first of a long series of 'superconductors' discovered which hold the ability to carry electric currents without measurable resistance or the dissipation of energy as heat. In the periodic table, superconductors are not even particularly rare; the majority of stable elements display superconductivity at some temperature or pressure [2]. Over the years following Onnes' discovery of superconductivity in mercury, superconductivity was observed at progressively higher temperatures in a range of compounds and alloys, spurring the hunt for room temperature superconductivity. Notably, in 1986, superconductivity in the cuprate system $Ba_2LaCu_3O_{7-\delta}$ at record high critical temperatures above 30 K was observed [3], followed by the first observation of 'high-temperature' superconductivity at temperatures above the boiling point of liquid nitrogen at atmospheric pressure (77 K) in $YBa_2Cu_3O_{7-\delta}$ near 92 K the following year [4]. At the time of writing, superconductivity in the carbonaceous sulfur hydride system at 'room' temperatures close to 288 K (15 °C) has recently been reported, but only under extreme pressures near 270 GPa [5].

However, just because a material is superconducting at a given temperature and pressure does not mean it will be useful in practice under those conditions. A finite superconductor cannot carry an unlimited amount of current without the onset of observable resistances. Instead, a superconductor can only carry electrical currents with negligible resistance provided the current per unit area flowing within the superconductor is below a maximum, 'critical' current density. Indeed, just below the critical temperature of the superconductor, this critical current density is zero, and the superconductor will not be able to carry any electric currents without the appearance of an electrical resistance! For a superconductor to be useful, therefore, the critical current density of the material under practical conditions must be sufficiently large for a given application. Technological scalability of the superconductor is also necessary, in order for high critical current densities observed in small samples of a superconductor to translate to practically useful large-scale conductors and components. As a result, whilst a large number of materials have now been found to become superconducting under sufficiently low temperatures and high pressures, only a handful are commonly used in large-scale conductors for technological applications. These include the niobium alloys NbTi and Nb_3Sn; the inexpensive intermetallic MgB_2; the cuprate bismuth strontium calcium copper oxide (BSCCO) high-temperature superconductors; and the high-temperature superconducting rare-earth barium copper oxide (RE)BCO materials commonly used in the form of thin films (typically $\sim 1\,\mu\mathrm{m}$ thick) deposited on metallic tapes.

Nevertheless, these technological materials carry exceptionally large electric current densities before significant resistances begin to appear, with typical engineering critical current densities of the order of $\mathrm{kA\,mm^{-2}}$ at 4.2 K in the absence of strong magnetic fields or strains. Such current densities enable applications that would be excessively expensive if only conventional conductors were available. Because of their unparalleled ability to carry large current densities without prohibitive power requirements, superconducting coils are used in the world's strongest continuous field electromagnets, capable of generate enormous continuous magnetic fields of up to 45.5 T [6] and routinely over 10 T. Superconducting magnets have found widespread use in the medical sector in Magnetic Resonance Imaging (MRI), which uses the relaxation of the alignment of the nuclear spins of ^{1}H nuclei (protons) in strong magnetic fields to non-invasively image soft tissues and fluids in the body that have high densities of ^{1}H [7]. Over 40,000 superconducting magnets have now been installed in hospitals worldwide [8]. The parent technique to MRI, Nuclear Magnetic Resonance (NMR), has revolutionised analytical chemistry by providing a highly effective tool for the identification of the structure and connectivity of complex molecules, and superconducting magnets are used routinely to provide the high magnetic field strengths, uniformity, and stability necessary to obtain the high resolution in NMR spectra that is required to distinguish between different chemical environments [9].

One particularly important application for driving the scale and performance of technological superconductors is their use in Magnetic Confinement Fusion (MCF) devices. Fusion – which releases energy via nuclear reactions that can occur between energetic light nuclei – is a highly attractive option for meeting the long-term energy demands of our planet. It provides the prospect of producing vast amounts of electrical energy from abundant fuel sources, without the direct production of greenhouse gases nor long-lived high activity radioactive waste. Our Sun is primarily powered by fusion reactions between protons, at temperatures around 15 million °C and extreme gravitational pressures in excess of 150 billion bar; on earth, where such pressures are unachievable, the most promising reaction for the commercial production of electrical energy is based on fusion between deuterium and tritium nuclei at temperatures over 150 million °C and a few bar of pressure [10]. To attain such high temperatures, strong magnetic fields are used to confine the charged particles that make up the plasma fuel and prevent the fuel from rapidly cooling down via collisions with the reactor walls. Strong magnetic fields are also used to shape and control the plasma for stability, and in tokamak designs, are used to drive large electric currents through the plasma for further stability and initial heating. Magnetic confinement fusion devices operate routinely around the world every day, but have not yet achieved the milestone of releasing more energy from the fusion reaction than put in to heat and stabilise the plasma and operate the magnet system. Superconductivity is therefore an enabling technology for commercially viable fusion energy, as it provides a mechanism by which these large magnetic fields can be generated without the prohibitive power demands required by coils constructed from conventional conductors [11]. A number of tokamaks using superconducting magnets are currently in operation around the world, including EAST, WEST, and KSTAR, and many more are under construction. Notably, the world's largest fusion reactor ITER, currently under construction in the south of France, that is planned to be the first device to produce net fusion power, will utilise Nb_3Sn in its eighteen toroidal field magnets and central solenoid, and will use six NbTi poloidal field magnets for plasma shaping [12]. Advances in the large-scale production of High Temperature Superconducting (HTS) tapes, which can operate under higher current densities at higher magnetic fields and temperatures than Nb_3Sn and NbTi, have recently spurred intense interest in the design of small magnetic confinement fusion reactors that take advantage of the effects of stronger magnetic fields on the fusion plasma, such as the SPARC tokamak under development between MIT and Commonwealth Fusion Systems [13]. For example, for a fixed ratio of the plasma pressure to the magnetic pressure – which is limited by plasma stability requirements – the fusion power density inside a tokamak scales as the fourth power of the toroidal magnetic field [14].

For these applications, understanding what limits the critical current densities in practical materials is therefore essential. Higher critical current densities allow smaller devices and magnets to be built whilst maintaining performance, which can significantly reduce their cost of use. As all technological superconductors are polycrystalline, understanding the role of grain boundaries in limiting critical current densities in these materials is particularly important for understanding possible methods by which these materials may be optimised in future.

In this thesis, we shall study the role of grain boundaries and grain boundary networks in limiting the critical current density of polycrystalline superconductors through the lens of Time-Dependent Ginzburg–Landau (TDGL) theory, both analytically, and with numerical simulations. In Chapter 2, we shall review the fundamental results of applied superconductivity, with focus on Ginzburg–Landau (GL) theory and its time-dependent extensions. In Chapter 3, we shall discuss the key numerical techniques used to solve the TDGL equations for studying vortex dynamics and critical currents from the literature, and outline the numerical algorithms implemented and used in simulations presented in the rest of the thesis. In Chapter 4, we tackle the problem of current flow across grain boundary structures in superconductors – modelled here as Josephson junctions – and find novel analytic expressions for how granular structures affect critical current densities in 2D systems. Finally, in Chapter 5, we present results of vortex dynamics simulations of 3D polycrystalline systems containing networks of grain boundaries, which are the first of their kind that show both the increase in critical current density with decreasing grain size and dependencies of the critical current on applied magnetic field that are widely observed in many commercial low temperature superconductors.

Chapter 2

Fundamentals of Superconductivity

2.1 Introduction

When a superconducting material is cooled below its critical temperature T_c, there are two characteristic properties associated with its entry into the superconducting state: the exhibition of zero electrical resistivity when subject to a DC current; and the expulsion of all magnetic flux from the superconducting bulk, known as the Meissner state [15]. Most of the practical applications of superconductors rely on the first of these properties – the ability to carry significant DC electric current density whilst displaying negligible electrical resistance. However, for real materials, the maximum current that can flow through a finite cross-sectional area of superconductor, the *critical current*, is not infinite, but depends sensitively on the local temperature, magnetic field, strain, and microstructure of the material. Furthermore, when cooled below T_c, all large-scale technological superconducting materials will display diamagnetism, but not all magnetic flux will be expelled from their bulk in high magnetic fields. Practical materials, therefore, are poorly described by these classic signatures of 'ideal' superconductors. What theories are available, then, to describe the phenomenology of the superconducting state in real systems?

In this chapter, we shall address this question by reviewing the key results in the literature that are used to predict and characterise the behaviour of superconductors for practical applications. In Section 2.2, we present an outline of the microscopic Bardeen–Cooper–Schrieffer (BCS) theory, which has proved successful in providing a mechanism for superconductivity in conventional low-temperature superconductors. Next, we present an overview of the phenomenological GL theory for superconductors in Section 2.3, including the role of vortices, and present derivations of the key parameters used in applied superconductivity. Finally, we discuss how the microstructure and the movement of vortices determines the critical current density of superconducting materials in Section 2.4.

2.2 BCS Theory

2.2.1 Introduction

The development of a microscopic theory describing the origin of the superconducting state remained elusive for over 45 years since its first observation by Kamerlingh Onnes in 1911 [1]. In 1950, Frohlich first suggested that the effective phonon interaction between electrons as a possible mechanism for superconductivity [16]. Such a proposal provided a potential explanation for the observation that good normal-state conductors do not become superconductors, since significant phonon-electron coupling in a material is associated with high resistances in such materials. Following this, in 1956, Cooper showed that the ground state of the electron gas is unstable with respect to the formation of at least one bound pair of electrons if there exists an attractive net electron-electron interaction, such as that originating from the effective phonon interaction, regardless of its magnitude [17]. This surprising result was extended to find the variational ground state of a system containing many bound pairs of electrons by Bardeen, Cooper and Schrieffer in 1957, that later won them the 1972 Nobel Prize in Physics [18]. Since its proposal, BCS theory has successfully predicted the quantitative properties of many low-temperature superconductors, with experimental support from measurements of the dependence of transition temperature on ion mass (the isotope effect), density of states, heat capacity, and the Knight shift in superconductors [19]. However, it now seems unlikely that BCS theory and its extensions can be used to describe the behaviour of many high-temperature superconducting compounds such as the copper-oxide superconductors, if a simple phonon-mediated mechanism is applied [20, 21]. Nevertheless, as the only comprehensive microscopic theory widely available, in this section we provide an overview of BCS theory and its key results.

2.2.2 BCS Pairing Mechanism and Hamiltonian

The exchange of phonons between electrons in the Fermi sea gives rise to an effective interaction potential between electrons, which may be either attractive or repulsive depending on the magnitude of the difference between the single-particle energies $\varepsilon_{\boldsymbol{k}}$. Notably, the direct interaction arising from single-phonon exchange is strongest between two electrons of opposite momentum [22, 23]. However, the full expression for the effective electron-electron interaction potential is difficult to manipulate analytically as it also contains contributions from the Coulomb repulsion between electrons. Therefore, in order to render the problem analytically tractable, BCS considered a simplified electron-electron interaction, proposing a model pair-interaction Hamiltonian of the form

$$\mathcal{H} = \sum_{\boldsymbol{k},\sigma} \varepsilon_{\boldsymbol{k}} c^{\dagger}_{\boldsymbol{k},\sigma} c_{\boldsymbol{k},\sigma} + \sum_{\boldsymbol{k},\boldsymbol{k}'} V_{\boldsymbol{k},\boldsymbol{k}'} c^{\dagger}_{\boldsymbol{k},\uparrow} c^{\dagger}_{-\boldsymbol{k},\downarrow} c_{-\boldsymbol{k}',\downarrow} c_{\boldsymbol{k}',\uparrow}. \tag{2.2.1}$$

Here the creation and annihilation operators $c^{\dagger}_{\boldsymbol{k},\sigma}$ and $c_{\boldsymbol{k},\sigma}$ represent the creation and annihilation respectively of a fermion in a state with wave vector $\boldsymbol{k}$ and spin $\sigma \in \{\uparrow, \downarrow\}$ [15]. By construction, in Eq. (2.2.1), only the electron-electron interaction terms corresponding to the scattering of an electron pair in states $(\boldsymbol{k}', \uparrow)$ and $(-\boldsymbol{k}', \downarrow)$ into states $(\boldsymbol{k}, \uparrow)$ and $(\boldsymbol{k}, \downarrow)$ have been considered, motivated by the earlier discussion of the phonon-phonon interaction. In order to maintain conservation of particle number when minimising the ground state energy of a many-body system, the zero of the single-particle energies $\varepsilon_{\boldsymbol{k}}$ is taken as the Fermi energy of the system. Of course, for Eq. (2.2.1) to be used to provide quantitative results, the form of the interaction potential $V_{\boldsymbol{k},\boldsymbol{k}'}$ must, in principle, be known. For simplicity, BCS assumed an isotropic, square-well type interaction of the form

$$V_{\boldsymbol{k},\boldsymbol{k}'} = \begin{cases} -V & \text{if } |\varepsilon_{\boldsymbol{k}}|, |\varepsilon_{\boldsymbol{k}'}| < \hbar\omega_{\mathrm{D}} \\ 0 & \text{otherwise} \end{cases} , \tag{2.2.2}$$

where the Debye energy $\hbar\omega_{\mathrm{D}}$ is used as an approximation to the average phonon energy and V is a constant parameterising the strength of the interaction [22]. It should be noted, however, that many of the key results of BCS theory depend only on the requirement that the effective electron-electron potential $V_{\boldsymbol{k},\boldsymbol{k}'}$ is attractive and not on the specific form of the interaction potential. Whilst the treatment of BCS theory is usually restricted for simplicity to the behaviour of the homogeneous electron gas described by the pair interaction Hamiltonian given in Eq. (2.2.1), the analysis can be generalised to include the effect of arbitrary external potentials, such as those imposed by impurities and/or magnetic fields. Such a method is based on a generalisation of the Hartree—Fock method to the superconducting state that was formalised by Bogoliubov and de Gennes, but a full discussion of this approach is outside the scope of the current presentation [23].

2.2.3 BCS Energy Gap and Density of States

Direct investigation of the BCS ground state directly is challenging, due to the two-body interaction in the pair-interaction Hamiltonian of Eq. (2.2.1). Therefore, to simplify the BCS pair-interaction Hamiltonian, mean field theory is employed. As the order parameter for the mean-field approach, BCS took the thermal average

$$b_{\boldsymbol{k}} = \langle c_{-\boldsymbol{k},\downarrow} c_{\boldsymbol{k},\uparrow} \rangle , \tag{2.2.3}$$

which is expected to be zero in the normal state [15]. The pair potential $\Delta_{\boldsymbol{k}}$ can then be similarly defined in terms of the BCS order parameter as

$$\Delta_{\boldsymbol{k}} = -\sum_{\boldsymbol{k}'} V_{\boldsymbol{k},\boldsymbol{k}'} \left\langle c_{-\boldsymbol{k}',\downarrow} c_{\boldsymbol{k}',\uparrow} \right\rangle \tag{2.2.4}$$

for convenience. The symmetries of $\Delta_{\boldsymbol{k}}$ are determined by the symmetries broken in the transition from the normal to the superconducting state. In a 'conventional' superconductor, only the global $U(1)$ phase rotation symmetry of the system is broken, and $\Delta_{\boldsymbol{k}}$ is isotropic. In an 'unconventional' superconductor, other symmetries are also broken, and the translational symmetry of the superconducting phase may differ from that of the normal state [24]. Such cases are likely important in modelling the behaviour of many high-temperature superconductors such as YBCO [15]. We shall predominantly restrict our discussion to conventional superconductors here, noting that the extension to the unconventional case is possible, if algebraically tedious. By substituting $b_{\boldsymbol{k}}$ and $\Delta_{\boldsymbol{k}}$ into Eq. (2.2.1) and assuming that terms bilinear in the fluctuation $(c_{-\boldsymbol{k},\downarrow} c_{\boldsymbol{k},\uparrow} - b_{\boldsymbol{k}})$ can be neglected, the effective Hamiltonian is obtained in the form

$$\mathcal{H}_{\text{eff}} = \sum_{\boldsymbol{k},\sigma} \varepsilon_{\boldsymbol{k}} c^{\dagger}_{\boldsymbol{k},\sigma} c_{\boldsymbol{k},\sigma} + \sum_{\boldsymbol{k}} \left(\Delta_{\boldsymbol{k}} c^{\dagger}_{\boldsymbol{k},\uparrow} c^{\dagger}_{-\boldsymbol{k},\downarrow} + \Delta^{*}_{\boldsymbol{k}} c_{-\boldsymbol{k},\downarrow} c_{\boldsymbol{k},\uparrow} - \Delta_{\boldsymbol{k}} b^{*}_{\boldsymbol{k}}, \right) \tag{2.2.5}$$

which is bilinear in the fermionic creation and annihilation operators. As a result, the effective Hamiltonian can be diagonalised via an arbitrary unitary transformation proposed by Bogoliubov and Valatin,

$$c_{\boldsymbol{k},\sigma} = u_{\boldsymbol{k}} \gamma_{\boldsymbol{k},\sigma} + \sigma v_{\boldsymbol{k}} \gamma^{\dagger}_{-\boldsymbol{k},-\sigma}, \tag{2.2.6}$$

where the new quasiparticle operators $\gamma^{\dagger}_{\boldsymbol{k},\sigma}$ and $\gamma_{\boldsymbol{k},\sigma}$ respectively represent the creation and annihilation of so-called Bogoliubov quasiparticles in the system [22]. Importantly, from Eq. (2.2.6), one can also show that $\gamma^{\dagger}_{\boldsymbol{k},\sigma}$ and $\gamma_{\boldsymbol{k},\sigma}$ satisfy fermionic anticommutation relations. Then, for an appropriate choice of the constants $u_{\boldsymbol{k}}$ and $v_{\boldsymbol{k}}$, the effective Hamiltonian of Eq. (2.2.5) can be diagonalised in the basis of the new quasiparticle operators [15], and can be finally expressed in the form

$$\mathcal{H}_{\text{eff}} = \sum_{\boldsymbol{k}} \left(\varepsilon_{\boldsymbol{k}} - E_{\boldsymbol{k}} - \Delta_{\boldsymbol{k}} b^{*}_{\boldsymbol{k}} \right) + \sum_{\boldsymbol{k},\sigma} E_{\boldsymbol{k}} \gamma^{\dagger}_{\boldsymbol{k},\sigma} \gamma_{\boldsymbol{k},\sigma}, \tag{2.2.7}$$

with $E_{\boldsymbol{k}}$ satisfying

$$E_{\boldsymbol{k}}^2 = \varepsilon_{\boldsymbol{k}}^2 + |\Delta_{\boldsymbol{k}}|^2 . \tag{2.2.8}$$

The first sum in Eq. (2.2.7) is independent of the state of the system, and acts as only a constant shift to the ground-state energy. In the second sum, the term $\gamma^\dagger_{\boldsymbol{k},\sigma}\gamma_{\boldsymbol{k},\sigma}$ can be identified as the number operator for the Bogoliubov quasiparticles, which implies that the quantity $E_{\boldsymbol{k}}$ represents the energy of an elementary excitation (quasiparticle) in the system. Furthermore, from Eq. (2.2.8), one can infer that $|\Delta_{\boldsymbol{k}}|$ represents the energy gap for elementary excitations with wave vector $\boldsymbol{k}$ in the system, since $|E_{\boldsymbol{k}}| \geq |\Delta_{\boldsymbol{k}}|$ for all $\boldsymbol{k}$. For conventional superconductors, the pair potential is isotropic, so $\Delta_{\boldsymbol{k}} = \Delta$. In this case, in the thermodynamic limit, the quasiparticle energy levels $E_{\boldsymbol{k}}$ can be approximated by the continuous variable E and used to calculate the BCS density of states $N(E)$ from the quasiparticle energy relation using Eq. (2.2.8)

$$N(E) = \begin{cases} 0 & |E| < |\Delta| \\ \frac{N(0)E}{\sqrt{E^2 - |\Delta|^2}} & |E| > |\Delta| \end{cases} , \tag{2.2.9}$$

where $N(0)$ is the density of states of the free electron model. The density of states has been well-studied experimentally via electron tunnelling measurements, and found to be in good agreement with the predictions of Eq. (2.2.9) for many superconductors, except close to the energy gap edge [19].

2.2.4 BCS Gap Equation and Transition Temperature

We next review the properties of the pair potential $\Delta_{\boldsymbol{k}}$ in BCS theory. In order to ensure self-consistency between the definition of the pair potential, Eq. (2.2.4), and the Bogoliubov transformation Eq. (2.2.6) which diagonalises the effective Hamiltonian Eq. (2.2.5), the condition

$$\Delta_{\boldsymbol{k}} = -\sum_{\boldsymbol{k}'} V_{\boldsymbol{k},\boldsymbol{k}'} \frac{\Delta_{\boldsymbol{k}'}}{2E_{\boldsymbol{k}'}} \left\langle 1 - \gamma^\dagger_{\boldsymbol{k}',\downarrow}\gamma_{\boldsymbol{k}',\downarrow} - \gamma^\dagger_{\boldsymbol{k}',\uparrow}\gamma_{\boldsymbol{k}',\uparrow} \right\rangle \tag{2.2.10}$$

must be satisfied. By defining the quasiparticle occupation number $f_{\boldsymbol{k}}$ as

$$f_{\boldsymbol{k}} = \left\langle \gamma^\dagger_{\boldsymbol{k},\sigma}\gamma_{\boldsymbol{k},\sigma} \right\rangle \tag{2.2.11}$$

and minimising over the free energy of the system, after application of the fermionic anticommutation relations for the quasiparticle operators, $f_{\boldsymbol{k}}$ is found to be the Fermi-Dirac distribution function [23]. This leads directly from Eq. (2.2.10) to the BCS Gap equation

$$\Delta_{\boldsymbol{k}} = -\sum_{\boldsymbol{k}'} V_{\boldsymbol{k},\boldsymbol{k}'} \frac{\Delta_{\boldsymbol{k}'}}{2E_{\boldsymbol{k}'}} \tanh\left(\frac{E_{\boldsymbol{k}'}}{2k_{\mathrm{B}}T}\right). \tag{2.2.12}$$

Once again, this may be considerably simplified by taking the BCS interaction potential of Eq. (2.2.2) and taking the thermodynamic limit, to obtain

$$\frac{1}{N(0)V} = \int_0^{\hbar\omega_{\mathrm{D}}} \frac{1}{\sqrt{\varepsilon^2 + |\Delta|^2}} \tanh\left(\frac{\sqrt{\varepsilon^2 + |\Delta|^2}}{2k_{\mathrm{B}}T}\right) \mathrm{d}\varepsilon. \tag{2.2.13}$$

The integral in Eq. (2.2.13) cannot generally be evaluated analytically except in particular limiting cases. In the weak coupling limit $N(0)V \ll 1$, the gap parameter at zero temperature $|\Delta|_{T=0}$ is

$$|\Delta|_{T=0} = \hbar\omega_{\mathrm{D}} \exp\left(-\frac{1}{N(0)V}\right). \tag{2.2.14}$$

It can be seen from Eq. (2.2.14) that $|\Delta|_{T=0}$ is not analytic in the coupling constant $N(0)V$, due to the presence of an essential singularity at the point where $N(0)V = 0$. This implies that the energy gap at zero temperature possesses no perturbative expansion in the coupling constant $N(0)V$, providing an explanation for the failure of previous attempts to formulate a theory of the superconducting state based on perturbation theory [22]. Similarly, by taking the limit of Eq. (2.2.13) close to T_{c}, when $|\Delta| \to 0$, one obtains in the weak coupling limit

$$2\,|\Delta|_{T=0} = 3.52 k_{\mathrm{B}} T_{\mathrm{c}}, \tag{2.2.15}$$

which provides a prediction for the transition temperature in terms of gap parameter at zero temperature. From Eqs. (2.2.14) and (2.2.15), and noting the ion mass $M \propto \omega_{\mathrm{D}}^{-2}$, one can also obtain a prediction for the isotope effect with $T_{\mathrm{c}} \propto M^{-1/2}$. Whilst this expression for the isotope effect and Eq. (2.2.15) are approximately consistent with the observed behaviour for many non-transition metal superconductors, many other superconductors deviate strongly from these predictions [19]. Whilst in some of these cases, this is expected to be an artefact of the assumptions imposed on the form of the electron-phonon interaction approximated by Eq. (2.2.2), in others these deviations suggest a different mechanism is responsible for the onset of superconductivity.

2.3 Ginzburg–Landau Theory

2.3.1 Introduction

The microscopic framework provided by BCS theory represented a significant step forward in the description of the superconducting state, but in cases where the pair potential varies spatially or when an external magnetic field is applied to the superconductor, a fully microscopic treatment remains excessively complex. In such regimes, the phenomenological GL theory is much more widely utilised. The theory was originally proposed by Ginzburg and Landau in 1950, prior to the development of BCS theory, on general considerations on properties of second order phase transitions [25]. However, the theory attracted little attention in western literature until 1959, when Gor'kov showed that GL theory arose as a rigorous limiting case of the microscopic BCS theory close to the critical temperature, under the assumption of local electrodynamics and slow variation in the pair potential and magnetic vector potential [26]. GL theory was subsequently generalised for 'dirty' superconductors containing high concentrations of impurities at all temperatures close to the critical magnetic field by Maki and DeGennes [27, 28, 29], and to the time-dependent case for systems dominated by paramagnetic impurities by a number of authors including Schmid, Gor'kov and Eliashberg [30, 31]. GL theory is now widely used as a starting point for modelling the macroscopic behaviour of superconductors in magnetic fields due to the relative simplicity with which it describes the spatial variation of the density of Cooper pairs and the physical insight it provides. In this chapter, we shall discuss the basis of GL theory and the key results for macroscopic superconductors, including critical fields and the properties of the Meissner and mixed states, along with a brief introduction to its extension to the time-dependent case.

2.3.2 Ginzburg—Landau Free Energy

GL theory arose from the general theory of second order phase transitions proposed by Landau. In his framework, across a second order phase transition, the symmetry group of the ground state of a system changes discontinuously as one or more of symmetries present in the more symmetric phase are spontaneously broken [32]. By definition, in a general transition into the superconducting state, at least one of the broken symmetries must be the global $U(1)$ phase rotation symmetry [33]. On group-theoretic grounds, the reduction in symmetry at a second order phase transition implies that the free energy of the system close to the transition temperature T_c may be expanded as a Taylor series in terms of a set of one or more functions $\{\psi_i\}$, which change continuously from zero in the more symmetric phase to non-zero in the less symmetric phase. The set of $\{\psi_i\}$ are referred to as order parameters for the transition and may be transformed into one another via transformations that are members of the symmetry group of the more symmetric phase [32]. As the free energy of a system must be invariant under any coordinate transformation, this symmetry condition on the order parameter(s) severely restricts which terms in the Taylor expansion of the free energy are non-zero, minimising the number of phenomenological parameters required to describe the state of the system close to the transition. Applying the Landau theory of second order phase transitions to a transition between a non-magnetic normal state and a superconductor, assuming a scalar order parameter for simplicity, Ginzburg and Landau proposed a free energy for a cubic crystal near T_c of the form

$$F = F_0 + \int \left(\alpha_\mathrm{GL} \left|\psi\right|^2 + \frac{1}{2}\beta_\mathrm{GL} \left|\psi\right|^4 + \frac{1}{2m_\mathrm{GL}} \left|\mathbf{\Pi}\psi\right|^2 + \frac{B^2}{2\mu_0} \right) \mathrm{d}^3\boldsymbol{r}, \tag{2.3.1}$$

where $\boldsymbol{\Pi} = -\imath\hbar\boldsymbol{\nabla} - 2e\boldsymbol{A}$ is the gauge invariant (kinetic) momentum operator; $\imath$ is the imaginary unit defined by $\imath^2 = -1$; $\boldsymbol{A}$ is the magnetic vector potential; $\boldsymbol{\nabla} \times \boldsymbol{A} = \boldsymbol{B}$ is the magnetic flux density and $-e$ is the charge of an electron [25, 34, 35, 36]. The quantity F_0 represents the free energy of the normal state in the absence of an applied magnetic field. The integral is over all space, and represents the combined free energy of the superconductor and any source of an externally applied magnetic field [37, 38]. For the order parameter corresponding to the minimum free energy to be zero at temperatures above T_{c} but non-zero below T_{c}, $\alpha_{\mathrm{GL}}(T)$ must be positive for $T > T_{\mathrm{c}}$ and negative for $T < T_{\mathrm{c}}$, and so close to T_{c} where the form of the GL free energy is valid, $\alpha_{\mathrm{GL}} \propto T - T_{\mathrm{c}}$. Similarly, for the order parameter corresponding to the minimum free energy to be finite in magnitude, β_{GL} must be positive either side of the transition temperature, and it is thus taken as independent of temperature close to T_{c}. The equations of motion for the equilibrium order parameter and magnetic vector potential can then be obtained up to a gauge transformation from Eq. (2.3.1) via variational minimisation of the free energy with respect to ψ and $\boldsymbol{A}$. Below T_{c}, the free energy F has a local minimum for a nonzero $|\psi|$ in the system, and the superconducting phase is thermodynamically stable; above T_{c}, no such minimum exists for $|\psi| \neq 0$, and superconductivity is unstable relative to the normal state. A depiction of the free energy variation as a function of $|\psi|$ for a bulk superconductor in the absence of magnetic fields is shown in Fig. 2.1.

It should be noted that the phenomenological parameters α_{GL}, β_{GL} and m_{GL} are only (collectively) specified up to a constant of proportionality, that sets the normalisation of $|\psi|^2$ [23, 22] and thus the microscopic interpretation of the order parameter. In Gor'kov's derivation of the GL free energy as a limit of BCS theory close to T_{c} using thermodynamic Green's functions, the GL order parameter ψ is found to be proportional to the pair potential Δ of BCS theory [39].

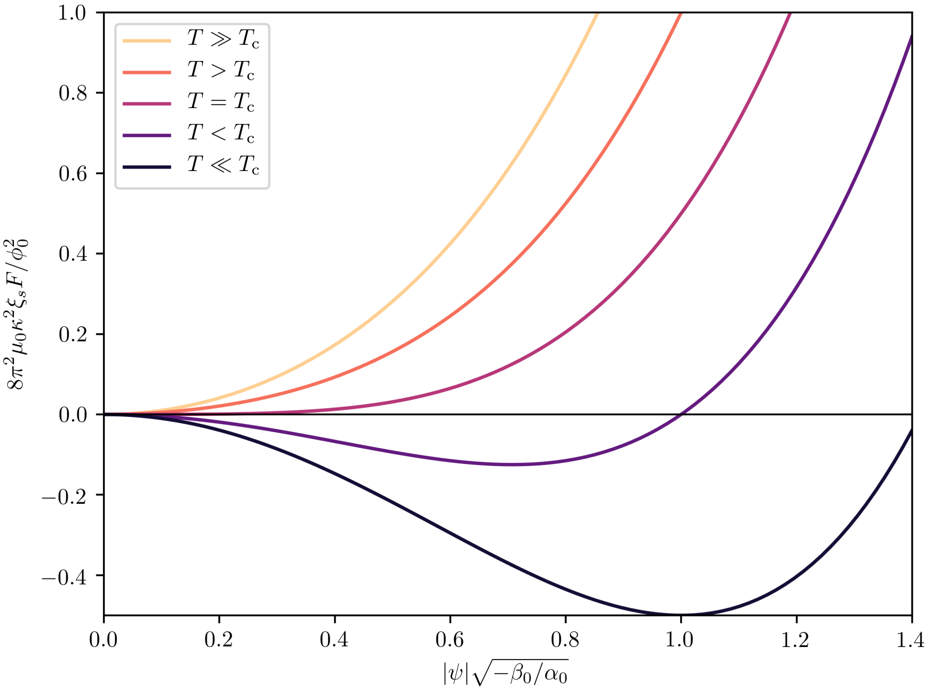

Figure 2.1: GL free energy of a uniform superconducting state in zero field, as a function of the order parameter magnitude $|\psi|$. Free energy F is determined from Eq. (2.3.1) with $F_0 = 0$. μ_0 is the permeability of free space; ϕ_0 is the magnetic flux quantum; κ is the Ginzburg–Landau constant; ξ_s is the superconducting coherence length for the $T \ll T_c$ curve; and α_0, β_0 are the GL parameters for the $T \ll T_c$ curve.

2.3.3 Ginzburg—Landau Equations

The ground state of the macroscopic system from the GL free energy presented in Eq. (2.3.1), can now be determined up to a gauge transformation. To do so, the GL free energy is variationally minimised with respect to fluctuations in the order parameter and the magnetic vector potential, to obtain a set of coupled differential equations that are satisfied for ψ and $\boldsymbol{A}$ in the ground state. By setting the functional derivative of the free energy with respect to the complex conjugate of the order parameter equal to zero,

$$\frac{\delta F}{\delta \psi^*} = 0, \tag{2.3.2}$$

and assuming that the fluctuation $\delta\psi^*$ may take arbitrary values at the surface of the superconductor, one obtains the first GL equation

$$\frac{1}{2m_{\mathrm{GL}}}\boldsymbol{\Pi}^2\psi + \alpha_{\mathrm{GL}}\psi + \beta_{\mathrm{GL}}\left|\psi\right|^2\psi = 0, \tag{2.3.3}$$

along with the boundary condition

$$\boldsymbol{n}\cdot\boldsymbol{\Pi}\psi = 0 \tag{2.3.4}$$

at the surface of the superconductor with outward normal unit vector $\boldsymbol{n}$ [15, 36, 37]. Similarly, the complex conjugate of Eqs. (2.3.3) and (2.3.4) may be obtained by setting $\delta F/\delta\psi = 0$. It should be noted that the boundary condition of Eq. (2.3.4) is only valid for an interface with a material that does not influence electrons in the superconductor, such as an insulator, as otherwise $\delta\psi^*$ may not necessarily take arbitrary values at the interface; a generalisation of this boundary condition at an interface through which no net current passes was derived from microscopic theory by De Gennes [23, 37]. The first GL equation, Eq. (2.3.3), has a similar form to the Schrödinger equation for a particle with charge $-2e$ and mass m_{GL} in a magnetic field, but with the addition of the nonlinear $\beta_{\mathrm{GL}}\left|\psi\right|^2\psi$ term [15]. This motivates the physical interpretation of ψ as proportional to the wavefunction of the centre-of-mass motion of the Cooper pairs in the superconductor [15]. The existence of this nonlinear term in Eq. (2.3.3) adds considerable complexity relative to the linearised equation where $\beta_{\mathrm{GL}}\left|\psi\right|^2\psi$ is neglected, but crucially determines the normalisation of ψ. Considering fluctuations of the magnetic vector potential on general thermodynamic grounds, for the chosen form of the GL free energy in Eq. (2.3.1), one has the general relation

$$\frac{\delta F}{\delta\boldsymbol{A}} = \mu_0\boldsymbol{J}_{\mathrm{app}}, \tag{2.3.5}$$

where $\boldsymbol{J}_{\mathrm{app}}$ is any externally applied current passing through the system, which is zero inside the superconductor in the absence of transport currents [37, 38]. Substituting Eq. (2.3.1) into Eq. (2.3.5), the second GL equation is obtained,

$$\boldsymbol{\nabla}\times\boldsymbol{B} = \mu_0\left(\boldsymbol{J}_{\mathrm{s}} + \boldsymbol{J}_{\mathrm{app}}\right), \tag{2.3.6}$$

where

$$\boldsymbol{J}_{\mathrm{s}} = \frac{2e}{m_{\mathrm{GL}}} \Im \left\{ \psi^* \left(\hbar \boldsymbol{\nabla} - 2\imath e \boldsymbol{A} \right) \psi \right\} = \frac{2e}{m_{\mathrm{GL}}} \Re \left\{ \psi^* \boldsymbol{\Pi} \psi \right\} \tag{2.3.7}$$

is the supercurrent in the system [15, 25, 36], where $\Re$ and $\Im$ represent the real and imaginary component operators respectively. Eq. (2.3.6) can be seen to be identical in form to one of Maxwell's equations in the absence of a time-varying electric field in the system, which directly implies continuity of current in the system, with $\boldsymbol{\nabla} \cdot (\boldsymbol{J}_{\mathrm{s}} + \boldsymbol{J}_{\mathrm{app}}) = 0$ [34]. Finally, in order to determine the state of the system, the two GL equations, Eqs. (2.3.3) and (2.3.6), must be self-consistently solved to obtain the order parameter ψ and the magnetic vector potential $\boldsymbol{A}$ up to a choice of gauge, and thus describe the macroscopic state of the system.

2.3.4 Superconducting Length Scales, The Meissner State and Type I Superconductors

We will now review some of the properties of the superconducting state that can be described by considering solutions to the GL equations. Firstly, we shall identify the characteristic length scales over which the order parameter magnitude $|\psi|$ and magnetic field $\boldsymbol{B}$ vary, and then present how Eqs. (2.3.3) and (2.3.6) suggest the existence of the Meissner state and a thermodynamic critical magnetic field in superconductors.

The approximate length scale over which the magnitude of the order parameter varies, the superconducting coherence length ξ, can be identified by considering the case of the superconductor in the absence of magnetic and electric fields, where $\boldsymbol{A} = \boldsymbol{0}$. In this case, the first GL equation of Eq. (2.3.3) reduces to

$$-\frac{\hbar^2}{2m_{\mathrm{GL}}} \nabla^2 \psi + \alpha_{\mathrm{GL}} \psi + \beta_{\mathrm{GL}} \left| \psi \right|^2 \psi = 0. \tag{2.3.8}$$

When the superconductor is in contact with a conductive metal occupying the region $x < 0$, the order parameter at the interface is suppressed and $\psi \approx 0$ [23]. Deep inside the superconductor, ψ is expected to be constant, so

$\lim_{x\to\infty}\{\boldsymbol{\nabla}\psi\} = \mathbf{0}$. Assuming that the order parameter is a one-dimensional function of the distance from the interface, $\psi = \psi(x)$, Eq. (2.3.8) can be solved to give

$$\psi = \psi_\infty \tanh\left(\frac{x}{\sqrt{2}\xi}\right), \tag{2.3.9}$$

where the order parameter deep inside the superconductor ψ_∞ is given by

$$|\psi_\infty|^2 = -\frac{\alpha_{\mathrm{GL}}}{\beta_{\mathrm{GL}}} = \frac{|\alpha_{\mathrm{GL}}|}{\beta_{\mathrm{GL}}}, \tag{2.3.10}$$

and the coherence length ξ is found to be [22]

$$\xi = \sqrt{\frac{\hbar^2}{2m_{\mathrm{GL}}\,|\alpha_{\mathrm{GL}}|}}. \tag{2.3.11}$$

This coherence length ξ is temperature dependent, and notably diverges as T approaches T_{c} when $|\alpha_{\mathrm{GL}}| \to 0$.

The approximate length scale over which the local magnetic field (and therefore current densities) vary in a superconductor, known as the penetration depth λ, can also be identified by considering solutions to the GL equations close to an interface with a conductive metal. Assuming that the order parameter ψ is analytic throughout the entire superconducting domain, $\boldsymbol{\nabla}\times\boldsymbol{\nabla}\psi = \mathbf{0}$ throughout the superconductor. Then, the curl of the second GL equation, Eq. (2.3.6), becomes

$$\boldsymbol{\nabla}\times\boldsymbol{\nabla}\times\boldsymbol{B} = -\frac{4e^2\mu_0}{m_{\mathrm{GL}}}\left[|\psi|^2(\boldsymbol{\nabla}\times\boldsymbol{A}) - \boldsymbol{A}\times\boldsymbol{\nabla}\left(|\psi|^2\right)\right]. \tag{2.3.12}$$

In weak fields, the final term here is small, and the curvature of the local magnetic field can be written as

$$\nabla^2\boldsymbol{B} = -\frac{|\psi|^2}{\lambda^2\,|\psi_\infty|^2}\boldsymbol{B}, \tag{2.3.13}$$

where the penetration depth λ, can be identified as

$$\lambda^2 = \frac{m_{\mathrm{GL}}\beta_{\mathrm{GL}}}{4e^2\mu_0\,|\alpha_{\mathrm{GL}}|}. \tag{2.3.14}$$

At the edge of the superconductor at the interface with a conductive metal, the boundary conditions $\psi = 0$ and $\boldsymbol{B} = B_{\mathrm{app}}\hat{\boldsymbol{k}}$ are imposed, and deep in the superconductor, B must remain finite. Assuming $B = B(x)$, Eq. (2.3.13) admits the solution for $x \gg \xi$

$$B = B_{\mathrm{app}} \exp\left(-\frac{x}{\lambda}\right), \tag{2.3.15}$$

which implies the local magnetic field decays exponentially deep inside the superconductor. The state described by Eq. (2.3.15), where an externally applied magnetic field is perfectly excluded from the bulk of the superconductor and the order parameter is homogeneous throughout the bulk, is the Meissner state. The Meissner state of perfect diamagnetism represents one of the two fundamental properties of an ideal superconductor discussed in the introduction; here, it has arisen as a property of the superconducting state in sufficiently weak fields as a consequence of describing the free energy of the superconductor in the form of Eq. (2.3.1) [15].

However, the Meissner state is not stable at all applied magnetic fields. The largest magnetic field B for which the Meissner state is thermodynamically stable relative to the normal state, referred to as the thermodynamic critical field B_{c}, can be obtained by considering Eq. (2.3.1). For the Meissner state, from Eqs. (2.3.9) and (2.3.15), $|\psi|^2 = |\alpha_{\mathrm{GL}}| / \beta_{\mathrm{GL}}$ with $B = 0$, whereas in the normal state subject to a magnetic field $\boldsymbol{B}_{\mathrm{app}}$, $\psi = 0$ and $\boldsymbol{B} = \boldsymbol{B}_{\mathrm{app}}$. From general thermodynamic considerations based on the form of the Ginzburg—Landau free energy used in Eq. (2.3.1),

$$\delta F = \frac{1}{\mu_0} \int \boldsymbol{B}_{\mathrm{app}} \cdot \delta \boldsymbol{B} \mathrm{d}^3 \boldsymbol{r}, \tag{2.3.16}$$

where $\boldsymbol{\nabla} \times \boldsymbol{B}_{\mathrm{app}} = \mu_0 \boldsymbol{J}_{\mathrm{app}}$ [38]. Therefore, taking the thermodynamic path integral of Eq. (2.3.16) at constant temperature from just above B_{c} to just below B_{c}, the free energy difference upon the transition is given by

$$F_{\mathrm{S}} - F_{\mathrm{N}} = -\frac{1}{\mu_0} \int B_{\mathrm{c}}^2 \mathrm{d}^3 \boldsymbol{r}, \tag{2.3.17}$$

where F_{S} is the free energy of the Meissner state in the bulk of a superconductor; and F_{N} is the free energy of the normal state including contributions from the local magnetic field, defined to be

$$F_{\mathrm{S}} = F_0 - \int \frac{\alpha_{\mathrm{GL}}^2}{2\beta_{\mathrm{GL}}} \mathrm{d}^3\boldsymbol{r}, \tag{2.3.18}$$

$$F_{\mathrm{N}} = F_0 + \int \frac{B_{\mathrm{c}}^2}{2\mu_0} \mathrm{d}^3\boldsymbol{r}. \tag{2.3.19}$$

Substituting Eqs. (2.3.18) and (2.3.19) into Eq. (2.3.17) gives the result for B_{c} as [22]

$$B_{\mathrm{c}}^2 = \frac{\mu_0 \alpha_{\mathrm{GL}}^2}{\beta_{\mathrm{GL}}}. \tag{2.3.20}$$

From the treatment of the superconducting state thus far, it may appear that B_{c} represents the largest magnetic field for which the superconducting state is stable. However, it should be noted that the derivation presented here only shows that the *Meissner state* is thermodynamically unstable with respect to the normal state above B_{c}, and does not preclude the possibility of a state existing with an order parameter that is inhomogeneous in the bulk being stable at higher applied magnetic fields. Whilst in some superconductors, referred to as Type I, the Meissner state is indeed the most stable superconducting state at all magnetic fields below B_{c}, in so-called Type II superconductors, there exists a range of magnetic fields at which a spatially inhomogeneous 'mixed state' is more thermodynamically stable. Type II superconductors, and the properties of the mixed state, are the topic of the next section.

2.3.5 Type II Superconductors, Vortices, and the Abrikosov Vortex Lattice

In the last section, we reviewed the solution (Eq. (2.3.9)) for the order parameter close to an interface with a conductive metal in zero field. In their original paper in which they proposed the free energy of Eq. (2.3.1), Ginzburg and Landau also provided an approximate solution for the order parameter at an insulating boundary in an externally applied magnetic field [25]. Crucially, in their derivation, they showed that the surface free energy of the system at the interface is positive when the Ginzburg—Landau parameter $\kappa = {}^{\lambda}/_{\xi} < {}^{1}/_{\sqrt{2}}$ and negative when $\kappa > {}^{1}/_{\sqrt{2}}$. The significant physical consequences of the change in sign of the surface free energy were not fully appreciated until 1957, when Abrikosov showed that a thermodynamically stable 'mixed state' existed for superconductors with $\kappa > {}^{1}/_{\sqrt{2}}$ at high fields that was multiply connected, with a lattice of local zeros of the order parameter present in the bulk, as a result of the energetic favourability of such superconductors to form interfaces [40]. The criterion $\kappa > {}^{1}/_{\sqrt{2}}$ defines Type II superconductors; similarly, Type I superconductors necessarily satisfy $\kappa \leq {}^{1}/_{\sqrt{2}}$. As an introduction to the properties of the mixed state, we first review the phenomenon of fluxoid quantisation in superconductors. By taking the integral of the second GL equation Eq. (2.3.6) about a closed contour in the superconductor, requiring the order parameter to be single valued throughout the superconducting domain,

$$\oint \left(\frac{\mu_0 m_{\mathrm{GL}}}{4e^2} \frac{\boldsymbol{J}_{\mathrm{s}}}{|\psi|^2} + \boldsymbol{A} \right) \cdot \mathrm{d}\boldsymbol{l} = n\phi_0, \tag{2.3.21}$$

where n is an integer and the magnetic flux quantum $\phi_0 = {}^{h}/_{2e}$ [15]. The integer n can be interpreted as the number of zeros of $|\psi|^2$ enclosed within the contour, or 'vortices'. Importantly, if $\boldsymbol{J}_{\mathrm{s}}$ and $\boldsymbol{A}$ are finite and $|\psi|^2 \neq 0$ at all points within the contour, then the contour may be continuously deformed to a point, and the system must be in the Meissner state with $n = 0$. If instead, for example, $|\psi|^2 = 0$ at points inside the contour, which may occur in the mixed state when the superconductor is multiply connected, then the contour cannot be continuously deformed and n can take nonzero values, implying that magnetic flux can partially penetrate the superconductor in the mixed state. Based on the observation from Eq. (2.3.21) that the number of vortices may be non-zero in the bulk in the mixed state, one may now calculate a lower bound for the magnetic field at which the mixed state of a Type II superconductor is stable. This may be carried out in a similar manner to the analysis for field at the end of the last section, by defining the lower critical field $B_{\mathrm{c}1}$ as the lowest magnetic field for which the thermodynamic stability of the Meissner state is equal to that of a superconducting state with a single vortices present in the bulk. The lower critical field B_{c1} has the simple form when $\kappa \gg 1$ [41]:

$$B_{\mathrm{c1}} = \frac{\mu_0 \phi_0}{4\pi\lambda^2} \left(\ln\kappa + 0.497\right) = \frac{B_{\mathrm{c}}}{\sqrt{2}\kappa} \left(\ln\kappa + 0.497\right). \tag{2.3.22}$$

For most Type II superconductors, κ is large, and thus B_{c1} is very small. As a result, the mixed state will be more stable than the Meissner state over most of the range of possible field values, and therefore dominates the physical properties of Type II superconductors.

Solutions for the mixed state of bulk Type II superconductors in high magnetic fields from the GL equations were first found by Abrikosov [40]. In this case, Abrikosov argued that the average value of the order parameter in the superconductor is small, and so the nonlinear term in Eq. (2.3.3) is unlikely to contribute significantly to leading order [40]. Therefore, a first approximation to the order parameter that satisfies the general nonlinear GL equation, Eq. (2.3.3), was obtained from the linearised GL equation

$$\frac{1}{2m_{\mathrm{GL}}} \boldsymbol{\Pi}^2 \psi_{\mathrm{L}} = \left|\alpha_{\mathrm{GL}}\right| \psi_{\mathrm{L}}. \tag{2.3.23}$$

Furthermore, since $\left|\psi_{\mathrm{L}}\right|^2$ is small in large fields, the induced current and magnetisation of the superconductor must also be small, and thus $\boldsymbol{B} \approx \boldsymbol{B}_{\mathrm{app}}$. For definiteness, the Coulomb gauge $\boldsymbol{\nabla} \cdot \boldsymbol{A} = \boldsymbol{0}$ can be imposed by setting

$$\boldsymbol{A} = \left(0, xB_{\mathrm{app}}, 0\right). \tag{2.3.24}$$

In this case, the linearised GL equation is equivalent to that of the Schrödinger equation of a charged particle in an external magnetic field, and may be solved by expressing the order parameter as its Fourier transform over the y and z directions;

$$\psi_{\mathrm{L}}\left(\boldsymbol{r}\right) = \iint f\left(x, x_n, k_z\right) e^{\imath k_y y} e^{\imath k_z z} \mathrm{d}k_y \mathrm{d}k_z, \tag{2.3.25}$$

where, defining $x_n = \phi_0 k_y / 2\pi B_{\mathrm{app}}$, Eq. (2.3.23) becomes

$$-\frac{\hbar^2}{2m_{\mathrm{GL}}} \left[\frac{\mathrm{d}^2}{\mathrm{d}x^2} - \left(\frac{2\pi B_{\mathrm{app}}}{\phi_0}\right)^2 \left(x - x_n\right)^2\right] f\left(x, x_n, k_z\right) = \left(\left|\alpha_{\mathrm{GL}}\right| - \frac{\hbar^2 k_z^2}{2m_{\mathrm{GL}}}\right) f\left(x, x_n, k_z\right), \tag{2.3.26}$$

and one may identify the equation as that of the quantum harmonic oscillator [22]. Bounded solutions for $f\left(x, x_n, k_z\right)$ as $x \rightarrow \infty$ only exist for a discrete set of fields B_{app}, determined by

$$B_{\text{app}} = \frac{\phi_0}{2\pi\left(2n+1\right)}\left(\frac{1}{\xi^2} - k_z^2\right), \tag{2.3.27}$$

where n is a positive integer. Clearly, the maximum applied field for which there exists a bounded solutions for $f\left(x, x_n, k_z\right)$ is obtained when $n = 0$ and $k_{\text{z}} = 0$. By definition, this field is the upper critical field B_{c2} and is given by

$$B_{\text{c2}} = \frac{\phi_0}{2\pi\xi^2} = \sqrt{2}\kappa B_{\text{c}}, \tag{2.3.28}$$

implying that for Type II superconductors, with $\kappa > {}^1\!/\!\sqrt{2}$, $B_{\text{c2}} > B_{\text{c}}$. The upper critical field B_{c2} represents the maximum magnetic field for which the mixed state is stable in the bulk.

The eigenfunctions corresponding to $B_{\text{app}} = B_{\text{c2}}$ in Eq. (2.3.26) are Gaussian in form, satisfying

$$f\left(x, x_n, k_z\right) \propto \exp\left[-\frac{\left(x - x_n\right)^2}{2\xi^2}\right], \tag{2.3.29}$$

allowing a general solution to Eq. (2.3.26) at B_{c2} to be expressed using Eq. (2.3.25). Next, Abrikosov applied periodic boundary conditions in the x and y directions. Imposing periodicity in the y direction implies only a discrete set of $k_y = nk$ are permissible, reducing the integral of Eq. (2.3.25) to a discrete sum of the form

$$\psi_{\text{L}}\left(\boldsymbol{r}\right) = \sum_n C_n e^{\imath nky} \exp\left[-\frac{\left(x - x_n\right)^2}{2\xi^2}\right]. \tag{2.3.30}$$

Additionally, periodicity in the x direction, demands

$$C_n = C_{n+N} \tag{2.3.31}$$

for some finite integer N. Then, from the GL equation for the current, Eq. (2.3.7), and the general form of the solution to the linearised equation, the magnitude of the $\boldsymbol{B}$-field induced by circulating supercurrents in the superconductor can be calculated to be

$$\left|\boldsymbol{B}_{\text{app}} - \boldsymbol{B}\right| \approx B_{\text{L}} = \frac{2\mu_0 e\hbar}{m_{\text{GL}}}\left|\psi_{\text{L}}\right|^2, \tag{2.3.32}$$

such that lines of constant $|\psi_\mathrm{L}|^2$ coincide with lines of constant B_L and streamlines of the induced current. Contours for the square magnitude of the order parameter $|\psi|^2$ based on Eq. (2.3.30) and streamlines of the current density from Eq. (2.3.32) for a triangular vortex lattice are displayed in Fig. 2.2.

However, without knowledge of the exact lattice structure, one cannot make any further statements from the linearised equation alone; in order to determine the normalisation of ψ_L, the non-linear terms in the GL equation must be considered. To do this, the Abrikosov parameter β_A is introduced,

$$\beta_\mathrm{A} = \frac{\int |\psi_\mathrm{L}|^4 \,\mathrm{d}^3\boldsymbol{r}}{\left(\int |\psi_\mathrm{L}|^2 \,\mathrm{d}^3\boldsymbol{r}\right)^2}, \tag{2.3.33}$$

which is independent of the normalisation of ψ_L and depends on the detailed properties of the lattice [40]. Then, the normalisation of ψ_L is determined in terms of β_A by expanding the exact solution of the first GL equation, Eq. (2.3.3), in terms of the solution obtained at B_c2 and small corrections ψ_1 and $\boldsymbol{A}_1$ to the order parameter and magnetic vector potential [22]. The order parameter is expanded as

$$\psi = \psi_\mathrm{L} + \psi_1, \tag{2.3.34}$$

with the additional condition that

$$\int \psi_\mathrm{L}^* \psi_1 \mathrm{d}^3\boldsymbol{r} = 0 \tag{2.3.35}$$

required to ensure and share the same normalisation. Similarly, the magnetic vector potential is expanded as

$$\boldsymbol{A} = \boldsymbol{A}_\mathrm{c2} + \boldsymbol{A}_1, \tag{2.3.36}$$

where the first order correction to the field is given by

$$\boldsymbol{\nabla} \times \boldsymbol{A}_1 = \boldsymbol{B} - \boldsymbol{B}_\mathrm{c2} \approx \boldsymbol{B}_\mathrm{app} - \boldsymbol{B}_\mathrm{L} - \boldsymbol{B}_\mathrm{c2} \tag{2.3.37}$$

and $\boldsymbol{\nabla} \times \boldsymbol{A}_\mathrm{c2} = \boldsymbol{B}_\mathrm{c2}$. Then, substituting in to the GL equation and neglecting second order terms in ψ_1, $\boldsymbol{A}_1$ and $\beta_\mathrm{GL} |\psi_\mathrm{L}|^2 \psi_\mathrm{L}$, the condition for the normalisation

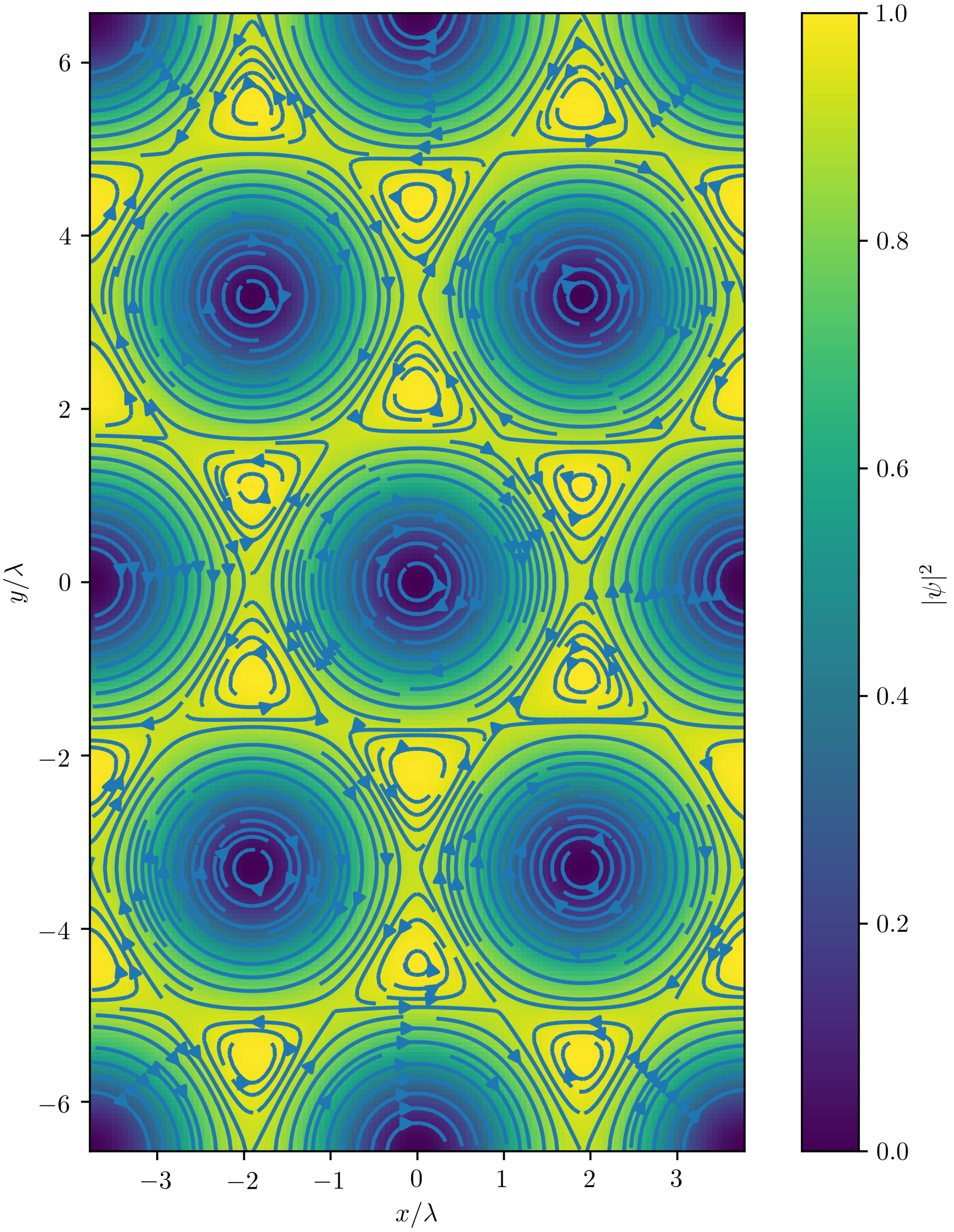

Figure 2.2: Square of the order parameter magnitude $|\psi|^2$ (color) and current density streamlines (arrows) in the Abrikosov vortex lattice, normalised such that $\max\{|\psi|^2\} = 1$, for a superconductor with Ginzburg–Landau parameter $\kappa = 1/\sqrt{2}$. λ is the superconducting penetration depth [42].

of the order parameter in terms of β_A is found as

$$\langle|\psi_\mathrm{L}|^2\rangle = \frac{m_\mathrm{GL}}{2\mu_0 e\hbar}\frac{B_\mathrm{c2} - B_\mathrm{app}}{(2\kappa^2 - 1)\,\beta_\mathrm{A}}, \tag{2.3.38}$$

implying that close to $\boldsymbol{B}_\mathrm{c2}$ the normalisation of the order parameter increases linearly as the applied field increases. Furthermore, from Eqs. (2.3.32) and (2.3.38), the average induction $\langle B\rangle$ in the superconductor can also be determined to be

$$\langle B\rangle = B_\mathrm{app} - \frac{B_\mathrm{c2} - B_\mathrm{app}}{(2\kappa^2 - 1)\,\beta_\mathrm{A}}, \tag{2.3.39}$$

which is, in general, nonzero, explicitly showing that a Type II superconductor in the mixed state described by Abrikosov does not act as a perfect diamagnet. The reversible magnetisation of the vortex lattice across the entire field range for Type II superconductors with varying values of κ is presented in Fig. 2.3, based on the method in [42]. close to B_c2, the magnetisation varies approximately linearly with field, as implied by Eq. (2.3.39).

It also can be shown that the free energy of the lattice decreases as the lattice parameter β_A decreases, and thus, the most stable lattice corresponds to the one for which the lattice parameter β_A is minimised. Abrikosov initially predicted the square lattice to be the most stable, but his result was later corrected by Kleiner et al. who showed that the triangular lattice minimised the free energy with $\beta_\mathrm{A} = 1.16$ [40, 43]. The triangular vortex lattice has since been observed experimentally in a wide range of superconducting materials.

As the applied magnetic fields is decreased below B_c2, the vortex-vortex spacing of the ideal vortex lattice increases. By applying Eq. (2.3.21) to a contour around a unit cell in the ideal lattice containing one vortex, the vortex-vortex spacing a_0 can be seen to increase with decreasing field as $a_0 \approx \sqrt{\phi_0/B}$. At lower fields, vortices are spread farther apart, and the order parameter recovers over the length scale of a coherence length ξ towards the Meissner state value in the regions between them. The local magnetic field at lower fields is strongly attenuated away from vortex cores, and decreases on the length scale of the penetration depth λ from its

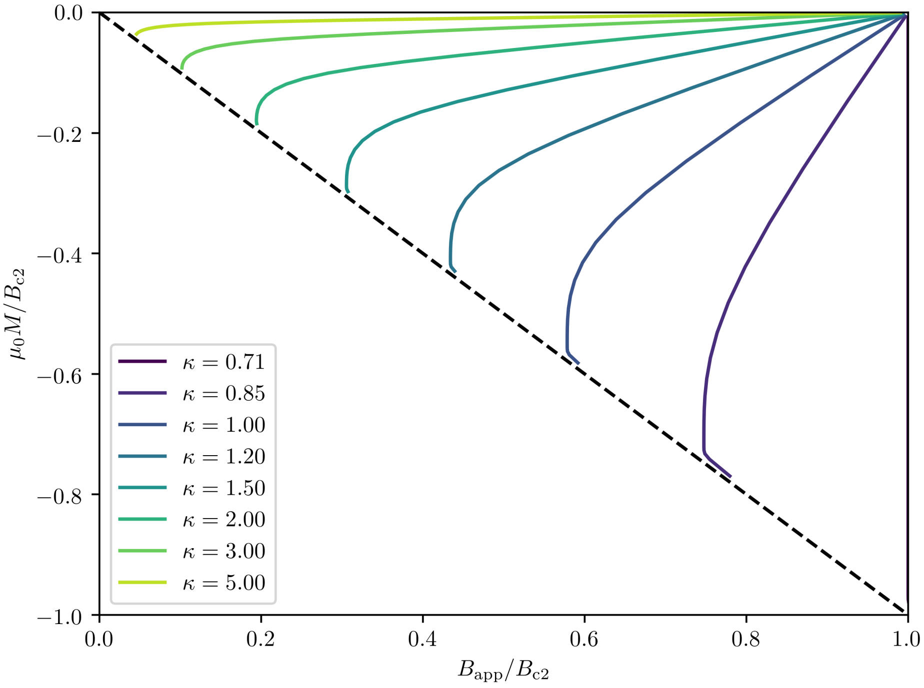

Figure 2.3: Reversible magnetisation M of the ideal vortex lattice as a function of applied field B_{app} in Type II superconductors. B_{c2} is the upper critical magnetic field of the superconductor.

peaks at the centre of vortices. Distributions of the square magnitude of the order parameter and the local magnetic field are provided in Fig. 2.4 for a superconductor with $\kappa = 1.5$, based on [42].

2.3.6 Surfaces, Coatings and Thin Film Superconductors

The upper critical field B_{c2} as given in Eq. (2.3.28) sets the limit for the magnetic field in the bulk of the superconductor for which the superconducting state is stable. However, superconductivity can still persist above this field close to insulating surfaces whose geometry restricts the symmetry of the order parameter, up to a higher, effective upper critical magnetic field B^*_{c2}.

The simplest case, when a plane insulating boundary parallel to the applied field is introduced to the system, was solved by Saint James and De Gennes [44].

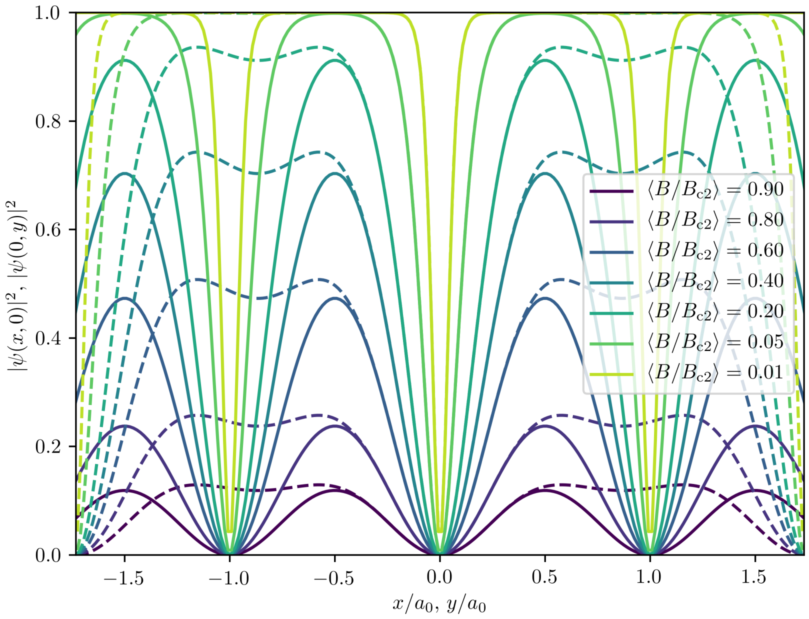

(a) $|\psi(\boldsymbol{r})|^2$

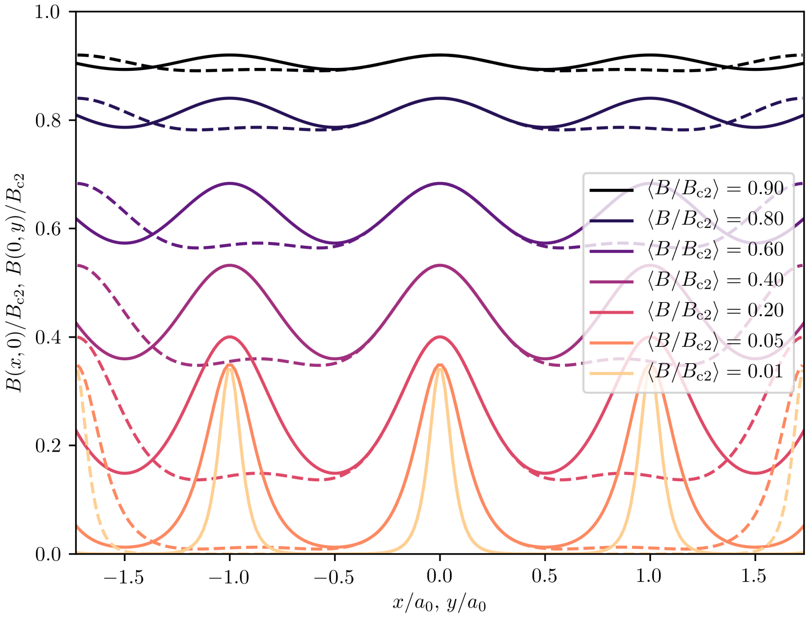

(b) $B(\boldsymbol{r})$

Figure 2.4: Spatial variation of (a) the square magnitude of the order parameter $|\psi(\boldsymbol{r})|^2$ and (b) the local magnetic field $B(\boldsymbol{r})$ for a superconductor with $\kappa = 1.5$ along the x and y axes, where the x axis is along the shortest distance between a vortex and one of its nearest neighbours, as in Fig. 2.2. B_{c2} is the upper critical magnetic field and a_0 is the vortex lattice spacing.

Introducing an insulating material in the region $x < 0$, and using Eq. (2.3.24) to define the gauge of the magnetic vector potential as before, the boundary condition Eq. (2.3.4) at the interface between the superconductor and insulator becomes simply $\partial_x \psi|_{x=0} = 0$. The linearised GL equation, Eq. (2.3.23) can then be solved for using the method of images, by considering the related problem defined by

$$-\frac{\hbar^2}{2m_{\mathrm{GL}}}\left[\frac{\mathrm{d}^2}{\mathrm{d}x^2} - \left(\frac{2\pi B_{\mathrm{app}}}{\phi_0}\right)^2 (|x| - x_n)^2\right] f(x, x_n, k_z) \\ = \left(|\alpha_{\mathrm{GL}}| - \frac{\hbar^2 k_z^2}{2m_{\mathrm{GL}}}\right) f(x, x_n, k_z) \tag{2.3.40}$$

and requiring continuity of the order parameter at $x = 0$. By construction, for $x \geq 0$, Eq. (2.3.40) is equal to Eq. (2.3.26) from the bulk case, and as Eq. (2.3.40) is symmetric about $x = 0$, its solutions will automatically satisfy the insulating boundary condition $\partial_x \psi|_{x=0} = 0$. In this case, the minimum eigenvalue, with $k_z = 0$, is given by

$$|\alpha_{\mathrm{GL}}| = 0.59 \frac{2\pi B^*_{\mathrm{c2}}}{\phi_0} \frac{\hbar^2}{2m_{\mathrm{GL}}}, \tag{2.3.41}$$

which can be rearranged to give the effective upper critical field B^*_{c2} for the superconducting state close to a plane insulating boundary, which is commonly referred to as the surface critical field B_{c3}

$$B_{\mathrm{c3}} = 1.695 \frac{\phi_0}{2\pi\xi^2} = 1.695 B_{\mathrm{c2}}. \tag{2.3.42}$$

Between B_{c2} and B_{c3} therefore, superconductivity is destroyed in the bulk of the superconductor, but can persist in a sheath region close to insulating surfaces of the superconductor. This sheath region is not present if the surface is highly conductive [22].

Superconductivity can also persist at applied magnetic fields above B_{c2} in thin film systems, when the magnetic field is applied parallel to the large, flat surfaces of the film, provided the surfaces are also insulating. When the film is sufficiently thin – of the order of the superconducting coherence length – the magnitude of the order parameter can be taken to be constant over the film thickness w, and the GL equation Eq. (2.3.3) can be averaged over the short axis of the film [45]. In this case, the upper critical field of the film $B_{\mathrm{c}\|}$ diverges as the film thickness decreases, and is given by

$$B_{\mathrm{c}\|} \approx \frac{\sqrt{12}\xi}{w} B_{\mathrm{c2}}. \tag{2.3.43}$$

Provided $w < 1.8\xi$, the approximation given in Eq. (2.3.43) is within 3% of the parallel critical field $B_{\mathrm{c}\|}$ calculated including higher order corrections; for thicker films, with $w > 1.8\xi$, vortices can enter the film and the assumption that the magnitude of the order parameter is constant over the film width no longer holds [45].

2.3.7 Anisotropic and Inhomogeneous Superconductors

Many superconductors, such as the high-temperature superconducting REBCO materials, are highly anisotropic. Such anisotropy can arise from the symmetry of the order parameter when anisotropic variations of material properties on length scales smaller than the coherence length are present. To describe such anisotropic systems, GL theory is often extended by replacing the effective Cooper pair mass m_{GL} with the components of the (anisotropic) effective mass tensor of Cooper pairs in the system $m_{\mathrm{GL};i,j}$ where $i, j \in \{x, y, z\}$ are indices labelling the coordinate axes. The free energy for an anisotropic 3D superconductor close to T_{c} is given by [46]

$$F_0 + \int_V \left(\alpha_{\mathrm{GL}}(T) \left|\psi\right|^2 + \frac{1}{2}\beta_{\mathrm{GL}} \left|\psi\right|^4 + \frac{1}{2}\sum_{i,j} \left[\Pi_i^* \psi^* m_{\mathrm{GL};i,j}^{-1} \Pi_j \psi \right] + \frac{B^2}{2\mu_0} \right) \mathrm{d}^3\boldsymbol{r}, \tag{2.3.44}$$

which has also been derived from Gor'kov as a limiting case of BCS theory when the pair potential is anisotropic [47]. If the coordinate axes $\{x, y, z\}$ are aligned along the crystal axes $\{a, b, c\}$ of the superconductor, the effective mass tensor is diagonal. For many layered superconductors like YBCO, effective masses along the a and b axes are similar, allowing the effective mass tensor in such materials to be described by only the two free parameters: the effective mass along the a and b

axes m_{ab}; and the effective mass along the c axis m_c. The anisotropy parameter $\gamma = m_c/m_{ab}$ is typically around 5-8 for YBCO.

When variations of material properties occur on length scales comparable to or larger than the superconducting coherence length ξ, the validity of assuming α_{GL}, β_{GL} and the components of the effective mass tensor $m_{\mathrm{GL};i,j}$ can be taken to be uniform in the superconductor breaks down. Boundary conditions for the GL equations at interfaces between superconducting materials close to their critical temperatures have been derived by Zaitsev [48] from BCS theory. The first of these conditions enforce continuity of the component of the supercurrent normal to the interface. The second depends on the nature of the interface. When the transmission coefficient of the interface is much larger than l_{mfp}/ξ, the pair potential Δ is continuous when electron reflections at the interface are specular [48, 49]; and the product $p_{\mathrm{F}}\Delta$ is continuous instead when reflections are diffuse, where p_{F} is the momentum of an electron at the Fermi surface [48, 50]. For interfaces between dirty superconductors and conductive metals, de Gennes showed that $\Delta/N(0)V$ is continuous when the thickness of the metal is much larger than the electronic mean free path l_{mfp} [27].

For the GL equations to be valid over all space for systems containing inhomogeneous materials, care must be employed when obtaining the equations of motion from Eq. (2.3.44) that only functional derivatives of the free energy with respect to continuous variables are taken. Fortunately, provided a continuous gauge for $\boldsymbol{A}$ and continuous order parameter ψ are chosen, a consistent set of GL equations for the inhomogeneous system can be obtained from Eq. (2.3.44) with spatially dependent $\alpha_{\mathrm{GL}}(\boldsymbol{r})$, $\beta_{\mathrm{GL}}(\boldsymbol{r})$ and $m^{-1}_{\mathrm{GL};i,j}(\boldsymbol{r})$ using Eqs. (2.3.2) and (2.3.5). Continuity of the supercurrent $\boldsymbol{J}_{\mathrm{s}}$ throughout the inhomogeneous system is then automatically satisfied via the first GL equation Eq. (2.3.3) when the order of derivatives around $m^{-1}_{\mathrm{GL};i,j}(\boldsymbol{r})$ is as written in Eq. (2.3.44) [34].

2.3.8 Time-Dependent Ginzburg—Landau Theory

The success of conventional Ginzburg—Landau theory to describe the macroscopic equilibrium state in superconductors has motivated many authors to attempt to construct a time-dependent Ginzburg—Landau (TDGL) theory to model dynamical behaviour [51]. Understanding how macroscopic superconductors behave in such regimes is necessary to determine their response to time-varying electric and magnetic fields and ultimately the critical current density they may carry without dissipation.

The simplest complete set of TDGL equations were derived by Gor'kov and Eliashberg from BCS theory in the gapless regime for superconductor dominated by paramagnetic impurities [15, 31]. An additional phenomenological parameter Γ is introduced, which parametrises how rapidly the order parameter relaxes into the equilibrium state from small perturbations from it. The TDGL equations are then given by [30, 52]

$$\Gamma\left(\partial_t + \frac{2\imath e}{\hbar}\mu_e\right)\psi = \left[-\alpha_{\mathrm{GL}} - \beta_{\mathrm{GL}}\left|\psi\right|^2 - \frac{1}{2}\sum_{i,j}\Pi_i m^{-1}_{\mathrm{GL};i,j}\Pi_j\right]\psi, \tag{2.3.45}$$

$$\boldsymbol{J} = \boldsymbol{J}_{\mathrm{app}} + \boldsymbol{J}_{\mathrm{s}} + \boldsymbol{J}_{\mathrm{n}}, \tag{2.3.46}$$

$$\rho = \varepsilon_0\frac{\mu_e - \varphi}{\lambda^2_{\mathrm{TF}}}, \tag{2.3.47}$$

with the current density terms given by

$$\boldsymbol{J}_{\mathrm{app}} = \mu_0^{-1}\boldsymbol{\nabla}\times\boldsymbol{B}_{\mathrm{app}}, \tag{2.3.48}$$

$$\boldsymbol{J}_{\mathrm{s}} = \sum_{i,j} 2em^{-1}_{\mathrm{GL};i,j}\Re\left\{\psi^*\Pi_j\psi\right\}\hat{\boldsymbol{e}}_i, \tag{2.3.49}$$

$$\boldsymbol{J}_{\mathrm{n}} = \sum_{i,j}\sigma_{\mathrm{N};i,j}\left(-\partial_j\mu_e - \partial_t A_j\right)\hat{\boldsymbol{e}}_i, \tag{2.3.50}$$

where $\boldsymbol{J}_{\mathrm{app}}$ is the externally applied current density; $\boldsymbol{J}_{\mathrm{s}}$ is the supercurrent density; $\boldsymbol{J}_{\mathrm{n}}$ is the normal current density; $\hat{\boldsymbol{e}}_i$ is the unit vector in the i direction; μ_e is the electrochemical potential divided by the magnitude of the electron charge e; φ is the electrostatic potential; ρ is the charge density per unit volume; $\sigma_{\mathrm{N};i,j}$

are the elements of the normal state conductivity tensor; ε_0 is the permittivity of free space; and λ_{TF}, is the Thomas-Fermi static-charge screening length [31]. Equations (2.3.45) to (2.3.47) are solved alongside the Maxwell equations for the electric field $\boldsymbol{E} = -\boldsymbol{\nabla}\varphi - \partial_t \boldsymbol{A}$ and magnetic field $\boldsymbol{B} = \boldsymbol{\nabla} \times \boldsymbol{A}$;

$$\boldsymbol{\nabla} \cdot \boldsymbol{E} = \frac{\rho}{\varepsilon_0}, \tag{2.3.51}$$

$$\boldsymbol{\nabla} \cdot \boldsymbol{B} = 0, \tag{2.3.52}$$

$$\boldsymbol{\nabla} \times \boldsymbol{E} = -\partial_t \boldsymbol{B}, \tag{2.3.53}$$

$$\boldsymbol{\nabla} \times \boldsymbol{B} = \mu_0 \boldsymbol{J} + \mu_0 \varepsilon_0 \partial_t \boldsymbol{E}. \tag{2.3.54}$$

Equations (2.3.45) to (2.3.47) and (2.3.51) to (2.3.54) uniquely define the state of the system in terms of ψ, $\boldsymbol{A}$, μ_e, and φ up to a gauge transformation.

For conventional superconductors, the Thomas-Fermi screening length is very small compared to all other length scales in the system. In the bulk of the system therefore, the superconductor may be considered ‘quasineutral’, and the local electrostatic potential is very close to the local electrochemical potential, allowing deviations of the electron density ρ from its average value to be neglected [53]. Furthermore, for systems in which the electric field is varying slowly with respect to time, the second term in Eq. (2.3.54) can be neglected, allowing the total current density to be written as $\boldsymbol{J} = \mu_0^{-1} \boldsymbol{\nabla} \times \boldsymbol{\nabla} \times \boldsymbol{A}$. Therefore, under magnetostatic and quasineutral conditions, Eqs. (2.3.45) and (2.3.46) can be decoupled from Eq. (2.3.47) and, along with a suitable gauge constraint, can be used to describe the dynamics of the superconducting state without the added complexity of considering local variations in the charge distribution ρ.

As noted above, the TDGL equations are only strictly valid in the gapless limit, when the lifetime of a Cooper pair τ_{int} is sufficiently small such that $\tau_{\mathrm{int}} |\Delta| \ll \hbar$ [39]. Nevertheless, despite the relatively narrow regime in which the TDGL equations may be rigorously derived, a wide range of authors have used the TDGL equations to investigate vortex dynamics in the flux-flow regime of the mixed state, in which current flow in the superconductor is resistive and the superconductor is unsuitable for many technological applications [51].

2.3.9 Normalised Ginzburg–Landau Equations

We have now reviewed the key length and time scales that occur in superconducting systems within Ginzburg–Landau theory, the magnetic flux quantum, and the maximum applied magnetic field for which superconductivity is stable in the bulk. For the remainder of this thesis, we shall find it convenient to express the Ginzburg–Landau free energy and equations of motion in a dimensionless form based on these length, time, and electromagnetic field scales. Hence, the Ginzburg–Landau free energy for gapless s-wave superconductors in the dirty limit [39], (Eq. (2.3.1)) is written as

$$F - F_0 = \int \left[-\alpha(\boldsymbol{r}) \left|\psi\right|^2 + \frac{1}{2}\beta(\boldsymbol{r}) \left|\psi\right|^4 + \sum_i m_i^{-1}(\boldsymbol{r}) \left|\left(\partial_i - \imath A_i\right)\psi\right|^2 + \kappa^2 B^2 \right] \mathrm{d}^3\boldsymbol{r}, \tag{2.3.55}$$

where a summary of the normalisations used for all variables is provided in Table 2.1. In Eq. (2.3.55), we note that the material parameters α, β and m_i^{-1} are the GL parameters α_{GL}, β_{GL} and m_{GL}^{-1} normalised relative to the values of the GL parameters of a reference superconductor α_{s}, β_{s} and $m_{x;\mathrm{s}}^{-1}$, and may be spatially variant. For a single component superconducting system therefore, $\alpha(\boldsymbol{r}) = \beta(\boldsymbol{r}) = m_x^{-1}(\boldsymbol{r}) = 1$, and for a material that is non-superconducting in the bulk, $\alpha(\boldsymbol{r}) < 0$. We summarise the normalised material parameters in Table 2.2.

The resultant TDGL equations from Eq. (2.3.55) become in dimensionless variables:

$$\eta\left(\partial_t + \imath\varphi\right)\psi = \left[\sum_i \left(\partial_i - \imath A_i\right) m_i^{-1}\left(\boldsymbol{r}\right)\left(\partial_i - \imath A_i\right) + \alpha\left(\boldsymbol{r}\right) - \beta(\boldsymbol{r})\left|\psi\right|^2\right]\psi,, \tag{2.3.56}$$

$$\partial_t A_i + \partial_i\varphi = -\,\kappa^2 m_i(\boldsymbol{r})\left(\boldsymbol{\nabla}\times\boldsymbol{\nabla}\times\boldsymbol{A}\right)_i + \mathrm{Im}\left[\psi^*(\partial_i - \imath A_i)\psi\right], \tag{2.3.57}$$

with the associated boundary conditions

$$\left(\boldsymbol{\nabla}\times\boldsymbol{A} - \boldsymbol{B}_{\mathrm{app}}\right)\times\widehat{\boldsymbol{n}} = \boldsymbol{0}, \tag{2.3.58}$$

$$\left(\boldsymbol{\nabla} - \imath\boldsymbol{A}\right)\psi\cdot\widehat{\boldsymbol{n}} = -\gamma\psi. \tag{2.3.59}$$

Symbol	Units	Interpretation
$\boldsymbol{r}$	$\xi_\mathrm{s} = \hbar/\sqrt{-2m_\mathrm{s}\alpha_\mathrm{s}}$	Position vector
t	$\tau = \mu_0\sigma_{\mathrm{N;s}}\lambda_\mathrm{s}^2$	Time
ψ	$\lvert\psi_0\rvert = \sqrt{-\alpha_\mathrm{s}/\beta_\mathrm{s}}$	Order parameter
$\boldsymbol{A}$	$A_0 = \phi_0/2\pi\xi_\mathrm{s}$	Magnetic vector potential
φ	$\varphi_0 = \phi_0/2\pi\tau$	Electrostatic potential
$\boldsymbol{B}$	$B_{\mathrm{c}2} = \phi_0/2\pi\xi_\mathrm{s}^2$	Magnetic induction
$\boldsymbol{E}$	$E_0 = \phi_0/2\pi\tau\xi_\mathrm{s}$	Electric field
$\boldsymbol{J}$	$J_0 = \phi_0/2\pi\mu_0\kappa^2\xi_\mathrm{s}^3$	Current density
F	$\phi_0^2/8\pi^2\mu_0\kappa^2\xi_\mathrm{s}$	Free energy

Table 2.1: Definition of units used in the normalised TDGL equations.

Symbol	Definition	Interpretation
$\alpha(\boldsymbol{r})$	$\alpha_{\mathrm{GL}}(\boldsymbol{r})/\alpha_\mathrm{s}$	Relative condensation parameter
$\beta(\boldsymbol{r})$	$\beta_{\mathrm{GL}}(\boldsymbol{r})/\beta_\mathrm{s}$	Relative nonlinearity parameter
$m_i^{-1}(\boldsymbol{r})$	$m_{\mathrm{GL};i}^{-1}(\boldsymbol{r})/m_{x;\mathrm{s}}^{-1}$	Relative inverse effective mass tensor
κ	$\lambda_\mathrm{s}/\xi_\mathrm{s}$	Ginzburg–Landau parameter
η	$\Gamma/\mu_0\sigma_{\mathrm{N;s}}\lambda_\mathrm{s}^2$	Time scale ratio (friction coefficient)

Table 2.2: Definition of phenomenological parameters used in the normalised TDGL equations.

The dimensionless parameters κ and η characterize the superconductive material. κ is the well-known Ginzburg—Landau parameter that represents the ratio of the characteristic length scales for variations in the electromagnetic field and variations in the order parameter. Similarly, the friction coefficient η represents the ratio between the characteristic timescales for the evolution of the electromagnetic field and evolution of the order parameter field. The friction coefficient $\eta = \Gamma/\mu_0\sigma_{\mathrm{N;s}}\lambda_\mathrm{s}^2$ was shown by Schmid to have the limiting value of $\eta = 5.79$ in the dirty limit [30, 39]. The surface parameter γ is the reciprocal of the De Gennes extrapolation length (in normalized units) and has limiting values of $\lvert\gamma\rvert = 0$ for surfaces in contact with an insulator (or vacuum) and $\lvert\gamma\rvert = \infty$ for highly conductive surfaces [23]. We note that Eqs. (2.3.56) and (2.3.57) imply continuity of the supercurrent $\boldsymbol{J}_\mathrm{s} = \sum_i m_i^{-1}(\boldsymbol{r})\mathrm{Im}\left[\psi^*(\partial_i - \imath A_i)\psi\right]\hat{\boldsymbol{e}}_i$.

In cases where the (effective) penetration depth λ is much larger than all other length scales in the system, the TDGL equations Eq. (2.3.57) can be significantly further simplified, as the self-field induced by currents circulating around vortices in the system can be neglected compared to the applied field and transport current [54]. In this high-κ approximation, for an applied magnetic field B_{app} in the z direction, the normalised magnetic vector potential in the Coulomb gauge ($\boldsymbol{\nabla} \cdot \boldsymbol{A} = 0$) is expressed as $\boldsymbol{A} = -B_{\text{app}}\,(y - w/2)\,\hat{\boldsymbol{\imath}} - \boldsymbol{K}$, where $\boldsymbol{K} = K(t)\hat{\boldsymbol{\imath}}$ is a spatially invariant parameter required to enforce the Coulomb gauge constraint, and w is the width of the system in the y direction. The governing equations in the high-κ approximation, from Eq. (2.3.57) and the current continuity equation, are

$$\eta\,(\partial_t + \imath\varphi)\,\psi = \left[(\boldsymbol{\nabla} - \imath\boldsymbol{A})^2 + \alpha\,(\boldsymbol{r}) - |\psi|^2\right]\psi, \tag{2.3.60}$$

$$\nabla^2\varphi = \boldsymbol{\nabla} \cdot \operatorname{Im}\left[\psi^*(\boldsymbol{\nabla} - \imath\boldsymbol{A})\psi\right], \tag{2.3.61}$$

$$\partial_t K = J_{\text{app}} - \left\langle \operatorname{Im}\left[\psi^*(\partial_x - \imath A_x)\psi\right]\right\rangle, \tag{2.3.62}$$

where the averaging in Eq. (2.3.62) is across the whole domain and at a constant applied magnetic field B_{app}, and we have assumed $\alpha(\boldsymbol{r})$ is the only spatially varying material parameter. The gauge constraint $\boldsymbol{K}$ can be used to determine the average electric field $\langle \boldsymbol{E} \rangle$ across the domain, since $\partial_t\boldsymbol{K} = \langle \boldsymbol{E} \rangle$. This formulation is particularly useful for 3D simulations of superconducting systems, which we shall discuss in the next chapter, as the time dependence of the electromagnetic fields is coupled only through the spatially invariant gauge parameter $\boldsymbol{K}$, reducing the computational cost of evolving the superconducting state in time [54].

2.4 Vortex Dynamics, Critical Currents, and Microstructures

2.4.1 Critical and Depairing Current Densities

At this juncture, it would be reasonable to query why, and how, the study of vortex dynamics in superconducting materials is of practical interest for the properties of technological superconductors. The answer to this can be inferred from the

Maxwell equation Eq. (2.3.53) along with the observation that the magnetic field distribution inside the superconductor is determined by the distribution (and shape) of vortices in the system. Vortex motion is therefore accompanied by variation of the local magnetic fields in the superconductor with respect to time, which, via Eq. (2.3.53), is associated with an electric field distribution. Furthermore, the vortex distribution experiences a net Lorentz force per unit volume $\boldsymbol{F}_{\mathrm{L}} = \boldsymbol{J} \times \boldsymbol{B}$ when a transport current flows through the system, which will cause vortices to start moving when the applied transport current is sufficiently large that $\boldsymbol{F}_{\mathrm{L}}$ is no longer balanced by other forces acting on them. The transport current density at which the motion of significant numbers of vortices first occurs therefore is associated with the onset of dissipation in the superconductor, and can be interpreted as the critical current density J_{c}.

An upper bound to the critical current density J_{c} can be found in zero field from Eqs. (2.3.56) and (2.3.57). In a dissipationless state, the electric field $\boldsymbol{E}$ must be zero; and as any vortices in the system must be static in the steady state, the magnitude of the order parameter $|\psi|$ cannot evolve with time. Under these assumptions, the time independent limit of Eqs. (2.3.56) and (2.3.57) can be taken, to give

$$\left\{ \sum_{i=x,y,z} \partial_i \left[m_i^{-1}(\boldsymbol{r})\, \partial_i \right] + \alpha(\boldsymbol{r}) - \beta(\boldsymbol{r})\, |\psi|^2 - \left[\sum_{i=x,y,z} \frac{J_{\mathrm{s};i}}{m_i^{-1}(\boldsymbol{r})\, |\psi|^2} \right]^2 \right\} |\psi| = 0. \tag{2.4.1}$$

In order for a nonzero $|\psi|$ that solves Eq. (2.4.1) to exist, the magnitude of the local current density $\boldsymbol{J}_{\mathrm{s}}$ cannot be made arbitrarily large. This can be determined by considering a narrow wire, homogeneous and infinite in extent in the x direction and with insulating boundary conditions applied at the edges of the superconducting domain in the transverse directions. Provided the wire is much narrower than a coherence length in the transverse directions, the current density may be assumed to flow only along the long axis of the wire in Eq. (2.4.1), and the current density can be written in terms of the magnitude of the order parameter in the wire as

$$\boldsymbol{J}_\mathrm{s}^2 = |\psi|^4 \left(1 - |\psi|^2\right). \tag{2.4.2}$$

Maximising J_s with respect to $|\psi|^2$ gives the maximum current for which a constant, non-zero, time invariant $|\psi|^2$ can be found. At this point $|\psi|^2 = 2/3$, and the maximum supercurrent density that can be carried by a homogeneous superconducting system – the depairing current density, J_D – can be found to be [15]

$$J_\mathrm{D} = \max_{|\psi|} \{\boldsymbol{J}_\mathrm{s}\} = \frac{2}{3\sqrt{3}} J_0. \tag{2.4.3}$$

However, experimental values of the critical current density J_c of technological superconductors is commonly between 0.1 - 10% of the depairing current density J_D [55]. Practical superconductors are usually much larger than the superconducting coherence length, and $|\psi|^2$ can no longer be assumed to be constant in the superconductor carrying large transport currents and in magnetic fields, due to the presence of vortices in the superconductor. To model the critical current density in practical superconductors therefore, the role of the superconductor microstructure in pinning magnetic flux and restricting vortex movement must be considered.

2.4.2 Flux Pinning

The role of microstructure in pinning vortices and preventing dissipation can be illustrated by considering the Abrikosov vortex lattice in an infinite, homogeneous superconductor as pictured in Fig. 2.2. As the superconductor is infinite and homogeneous, every point in the superconductor is equivalent to every other, and thus by symmetry, an Abrikosov vortex lattice can be translated in any direction without changing the total free energy of the superconductor. The net force on the Abrikosov vortex lattice is therefore zero, and is independent of the origin of the coordinate system. However, as discussed in Section 2.4.1, if a non-zero net transport current flows is now applied to the system, vortices will experience a Lorentz force $\boldsymbol{F}_\mathrm{L}$ acting to accelerate them. This Lorentz force is the only net force acting on the vortex lattice, and thus vortices will begin move, and an electric field will be generated, regardless of how large the transport current is. The critical current density for an infinite, homogeneous superconductor, lacking any microstructure, is therefore zero, and therefore cannot be used to carry dissipation-free currents for practical applications.

Of course, practical superconductors are able to carry large current densities without the onset of dissipation. Such systems are not homogeneous; α, β, and m^{-1} depend on position; and the free energy of the vortex lattice depends on the location and shape of vortices inside the system. Variations of the free energy of the vortex lattice with respect to the configuration of vortices in the system give rise to a net flux pinning force per unit volume F_{p}, which acts to oppose the Lorentz force $\boldsymbol{F}_{\mathrm{L}}$ and resists vortex motion. In particular, non-superconducting (or weakly superconducting) inclusions in the superconductor act as favourable pinning sites for vortices to occupy, as the vortex core intersecting a pinning site has a lower total free energy than configurations in which the pinning site and vortex core are well separated. In Section 2.4.1, the depairing current density J_{D} is found to be non-zero due to the flux pinning force provided by the interfaces between the superconductor and the surrounding insulator/vacuum.

Consequently, the critical current density J_{c} as a function of applied magnetic field is often expressed in terms of the maximum net flux pinning force per unit volume F_{p}, which acts to balance the Lorentz forces acting on the vortex lattice. Experimentally, this flux pinning force per unit volume is often characterised using the empirical expression [56]

$$F_{\mathrm{p}} \propto \frac{B_{\mathrm{c2}}^{n}}{\kappa^{2}} b^{p} \left(1 - b\right)^{q} , \tag{2.4.4}$$

where $b = B/B_{\mathrm{c2}}$ is the reduced field, and n, p and q are empirical flux pinning parameters independent of the applied magnetic field that characterise the pinning mechanism in the superconductor [57]. For NbTi, $p \approx 1$, $q \approx 1$ and $n \approx 5/2$ [58]; whereas for $\mathrm{Nb_3Sn}$, Kramer found $p \approx 1/2$, $q \approx 2$ and $n \approx 5/2$ in high fields, based on a flux shear mechanism [59]. However, exactly how the statistical summation of elementary pinning forces f_p that arise from individual pinning sites should be performed to find the net macroscopic F_p that can be used to characterise the macroscopic critical current density J_c is a long-standing problem in applied superconductivity, known as the *summation problem* [60, 61, 62].

Some solutions for F_p based on a random pinning potential have been found in limiting cases [63]. For weak random point-like pinning structures in a dislocation-free elastic vortex lattice, Larkin and Ovchinnikov developed the theory of collective pinning [64]. The flux pinning force in this case given by [64, 63]

$$F_\mathrm{p} \approx \begin{cases} \frac{\sqrt{3}}{32\sqrt{2}\pi^2} \frac{n_\mathrm{p}^2 \langle f_\mathrm{p}^2 \rangle^2}{r_\mathrm{p}^3 c_{66}^2 c_{44}} & \text{(3D)} \\ \frac{1}{\sqrt{8\pi}} \frac{n_\mathrm{p} \langle f_\mathrm{p}^2 \rangle}{r_\mathrm{p} d c_{66}} & \text{(2D)} \end{cases}, \tag{2.4.5}$$

where n_p is the number of pins per unit volume; $r_\mathrm{p} \approx \xi$ is the range of the pinning forces; and c_{44} and c_{66} are the tilt and shear modulus of the vortex lattice respectively, given by

$$c_{44} = B\frac{\partial F}{\partial B}, \tag{2.4.6}$$

$$c_{66} \approx \frac{B\phi_0}{16\pi\mu_0\lambda^2}\left(1 - \frac{1}{2\kappa^2}\right)(1-b)^2\left(1 - 0.58b + 0.29b^2\right). \tag{2.4.7}$$

When pinning is much stronger than vortex-vortex interactions in the vortex lattice, F_p is sometimes taken to be a direct sum of the elementary flux pinning forces over the number of active pins that are holding vortices. The flux pinning force per unit volume for strong random pins in an elastic vortex lattice are therefore given by

$$F_\mathrm{p} = \begin{cases} n_\mathrm{p} f_\mathrm{p} & \text{for } n_\mathrm{p}^{1/3} \ll a_0 \\ \left(n_\mathrm{p}^{1/3} B/\phi_0\right) f_\mathrm{p} & \text{for } n_\mathrm{p}^{1/3} \gg a_0 \end{cases}, \tag{2.4.8}$$

where $a_0 = \sqrt{\phi_0/B}$ is the vortex-vortex spacing.

Many other pinning structures, such as columnar pins, surfaces, and grain boundaries, can pin vortices effectively, and a wide range of functional forms for F_p have been proposed based on which microstructural features dominate the effective pinning mechanism at J_c. Nevertheless, the grand summation problem remains an open issue in how F_p should be obtained from the elementary flux pinning forces from these structures in general. For brevity, we refer the reader to a number of useful reviews available in the literature for further information on flux pinning models derived for other pinning structures [57, 63].

2.4.3 Macroscopic Superconductors

For macroscopic superconducting systems, understanding the critical current density J_c is important in predicting the large scale performance and field distributions in and around superconducting systems. The electric field of a superconducting system on length scales much larger than the vortex-vortex spacing and variations of material properties is commonly modelled using a power law dependence of the electric field on the current density passed through the material,

$$E = E_\mathrm{c}\left(\frac{J}{J_\mathrm{c}(B,T,\varepsilon,\theta)}\right)^{n(B,T,\varepsilon)}, \tag{2.4.9}$$

where n is a nonlinearity parameter and E_c is a reference critical electric field, commonly taken to be between $10\,\mu\mathrm{V\,m^{-1}}$ and $100\,\mu\mathrm{V\,m^{-1}}$ for transport measurements of technological superconductors [56]. The nonlinearity parameter n parametrises the rate of vortex creep in the superconductor, with high rates of vortex creep associated with large electric fields even at low currents, and thus with small values of n. However, in many technological superconductors, this electric field dependence is highly nonlinear, with n varying from 5 - 50 for practical materials.

2.5 Conclusions

BCS and GL theory are now well established frameworks for providing descriptions of the phenomenology of the superconducting state. However, with the rapid expansion in computing power over the last 50 years, numerical simulations have now become viable tools for investigating the behaviour of complex superconducting systems on physically relevant system scales, and have opened up opportunities for new insight into problems previously considered analytically intractable. This thesis follows such an approach, solving the time-dependent Ginzburg–Landau equations numerically using high performance computing resources to investigate critical currents and vortex dynamics in polycrystalline superconducting systems. In the next section, we outline the main algorithms and tools used in this work to solve the TDGL equations, along with their respective benefits and drawbacks.

Chapter 3

Numerical Methods for Solving the Time-Dependent Ginzburg–Landau Equations

3.1 Introduction

The TDGL equations provide a useful mathematical framework for the phenomenological study of vortex dynamics and critical currents in superconducting materials. However, for most practical systems of interest, which may contain a wide range of pinning structures and pin morphologies, the TDGL equations cannot be solved analytically. Instead, numerical techniques and discretisation schemes must be employed to study vortex dynamics in these regimes. The choice of discretisation scheme is limited by the requirement of gauge invariance [65]. Without gauge invariance, numerical artifacts can arise that lead to the violation of conservation laws satisfied by the exact TDGL equations, and unphysical dissipation mechanisms [66].

In this thesis, we use two main simulation codes based on gauge invariant finite difference approximations of the TDGL equations on regular, structured grids in 2D and 3D. Finite difference approximations have been the most widely used and well studied basis for solvers of the TDGL equations to date due to the relative simplicity in enforcing gauge invariance in the discrete equations obtained from them [67]. Finite element and finite volume approximations have also been constructed and applied to solve the TDGL equations, and offer particular advantages when studies of the effect of sample geometry and topology are of interest, as they allow the usage of unstructured meshes for the discretisation of the simulation domain that can reduce the number of degrees of freedom solved for at each timestep. Indeed, the commercial finite element software package COMSOL Multiphysics [68] has been widely used to study vortex dynamics using the TDGL equations for small systems [69, 70]. However, commercial finite element solvers offer limited scalability on high performance computing architectures, restricting the sizes of simulation domains that can be modelled, which particularly limits the ability to study vortex dynamics in large 3D superconducting domains. Licenses for such solvers can also be expensive, particularly for simulations on parallelised computer architectures, and as commercial solvers are generally closed-source, identifying algorithmic sources of error can be difficult. Scalable open source finite element software packages may be an option for the development of future TDGL solvers [71, 72], but existing general purpose solvers in such software packages are usually not easily optimised for the solution of the TDGL equations and require further development. Finite volume approximations to the TDGL equations [73] can preserve gauge invariance in the spatial discretisation, but to date implementations of such methods for unstructured meshes have been infrequently used in the literature. It is for these reasons we have chosen to implement algorithms based on existing finite difference approximations for our studies of vortex dynamics and critical current densities in this work. Further discussion of alternative numerical approximation methods for the TDGL equations can be found in [67].

For small system sizes in 2D, in this work we solve the general TDGL equations Eqs. (2.3.56) and (2.3.57) using our TDGL-ZEP code, based on the algorithm developed by [74] generalised to include a spatially dependent effective mass as in [75]. For larger systems, and in 3D, we solve the simplified TDGL equations in the high κ limit, Eqs. (2.3.60) to (2.3.62), on a GPU using our TDGL-HIK code, an implementation of the 3D TDGL solver developed by [54].

In the following sections, we describe these codes in more detail. We begin by describing the explicit method of [65], which introduces the usage of 'link variables' to enforce gauge invariance of the spatial discretisation schemes that are used in both simulation codes. We then summarise the algorithm implemented in TDGL-ZEP, and identify limitations in the previous solvers used by [74, 76] that can lead to unreliable convergence and loss of accuracy when studying systems where the local magnetic field varies significantly across the system and/or when large persistent electric fields are present in periodic systems. We also discuss the implementation of the solver developed by [54] in the TDGL-HIK code, for use on GPU architectures and present example results for vortex distributions in fixed applied magnetic fields. Finally, we present techniques developed to extract values of the critical current density J_c as a function of applied magnetic field from vortex dynamics simulations obtained from these codes. We have previously published the initial results using TDGL-ZEP presented in Figs. 3.2 and 3.5 to 3.7 and their associated sections in [77].

3.2 Numerical Algorithms

3.2.1 The Explicit Method of Gropp et al.

In this section, we review the explicit algorithm developed to solve the TDGL equations developed by Gropp et al. [65]. This method illustrates the use of link variables for the gauge invariant spatial discretisation of derivative terms in the TDGL equations, that the two main TDGL solvers implemented in this thesis, TDGL-ZEP and TDGL-HIK, will utilise.

Importantly, in [65], the spatial discretisation of the derivative terms is carried out in a gauge invariant manner, through the introduction of the *link variable* vector $\boldsymbol{U}$,

$$\begin{aligned}\boldsymbol{U}(\boldsymbol{r}) =& \exp\left(-\imath\int_{x_0}^{x} A_x(x',y,z)\mathrm{d}x'\right)\hat{\boldsymbol{e}}_x\\ &+\exp\left(-\imath\int_{y_0}^{y} A_y(x,y',z)\mathrm{d}y'\right)\hat{\boldsymbol{e}}_y\\ &+\exp\left(-\imath\int_{z_0}^{z} A_z(x,y,z')\mathrm{d}z'\right)\hat{\boldsymbol{e}}_z, \end{aligned}\tag{3.2.1}$$

where the components $U_\mu(\boldsymbol{r}) = \boldsymbol{U}_\mu(\boldsymbol{r})\cdot\hat{\boldsymbol{e}}_\mu$ are referred to as the link variables along the coordinate axes $\mu\in\{x,y,z\}$, and x_0 y_0 and z_0 are the coordinates of a reference point in the system. In terms of the link variables Eq. (3.2.1), the first order gauge invariant derivatives of the order parameter field are expressed via

$$(\boldsymbol{\nabla}-\imath\boldsymbol{A})\,\psi(\boldsymbol{r}) = \sum_{\mu=x,y,z} U_\mu^*\frac{\partial}{\partial\mu}\left(U_\mu\psi\right)\hat{\boldsymbol{e}}_\mu,\tag{3.2.2}$$

and second order gauge invariant derivatives are expressed using

$$(\boldsymbol{\nabla}-\imath\boldsymbol{A})^2\,\psi(\boldsymbol{r}) = \sum_{\mu=x,y,z} U_\mu^*\frac{\partial^2}{\partial\mu^2}\left(U_\mu\psi\right).\tag{3.2.3}$$

For the application of a finite difference method to approximate the spatial derivatives in the TDGL equations, the simulation space is discretised into a structured regular grid of nodes at points $\boldsymbol{r}_{i\in[1,n_x],j\in[1,n_y],k\in[1,n_z]}$ that are separated by step sizes h_μ in the $\mu\in\{x,y,z\}$ directions. The order parameter ψ is calculated on each node and the 'link variables' U_μ are defined on links between nodes, such that

$$\psi_{i,j,k} = \psi\left(\boldsymbol{r}_{i,j,k}\right),\tag{3.2.4}$$

$$U_{\mu;i,j,k} = U_\mu^*(\boldsymbol{r}_{i,j,k})U_\mu(\boldsymbol{r}_{i,j,k}+h_\mu\hat{\boldsymbol{e}}_\mu).\tag{3.2.5}$$

The TDGL equations Eqs. (3.2.2) and (3.2.3) in the zero electric potential gauge ($\varphi = 0\ \forall\ t$) are then discretised by approximating the gauge invariant spatial derivatives in Eqs. (3.2.2) and (3.2.3) through a second order central difference approximation, and time is evolved through the first order forward Euler method with timestep δt. The resulting equations in the bulk of a homogeneous superconductor are then expressed by

$$\psi_{i,j,k}(t+\delta t) = \psi_{i,j,k}(t) + \eta^{-1}\left(\mathcal{F}_{\psi}\left[\psi(t), \boldsymbol{U}(t)\right]\right)_{i,j,k}\delta t, \tag{3.2.6}$$

$$U_{\mu;i,j,k}(t+\delta t) = U_{\mu;i,j,k}(t)\exp\left\{-\imath\left(\mathcal{F}_{U_{\mu}}\left[\psi(t), \boldsymbol{U}(t)\right]\right)_{i,j,k}\delta t\right\}, \tag{3.2.7}$$

where

$$\begin{aligned}\left(\mathcal{F}_{\psi}\left[\psi(t), \boldsymbol{U}(t)\right]\right)_{i,j,k} &= \left(1 - \left|\psi_{i,j,k}\right|^{2}\right)\psi_{i,j,k} \\ &\quad + \sum_{\text{cyclic}} \frac{U^{*}_{x;i-1,j,k}\psi_{i-1,j,k} - 2\psi_{i,j,k} + U_{x;i,j,k}\psi_{i+1,j,k}}{h_{x}^{2}},\end{aligned} \tag{3.2.8}$$

in which the cyclic sum is over a cyclic permutation of $\{x, y, z\}$ and $\{i, j, k\}$, and

$$\begin{aligned}\left(\mathcal{F}_{U_{x}}\left[\psi(t), \boldsymbol{U}(t)\right]\right)_{i,j,k} = \kappa^{2}\Im\Bigg(&\frac{W_{z;i,j,k} - W_{z;i,j-1,k}}{h_{y}^{2}} - \frac{W_{y;i,j,k} - W_{y;i,j,k-1}}{h_{z}^{2}} \\ &+ U_{x;i,j,k}\psi^{*}_{i,j,k}\psi_{i+1,j,k}\Bigg),\end{aligned} \tag{3.2.9}$$

in which

$$W_{x;i,j,k} = \exp\left(-\imath\oint \boldsymbol{A}\cdot \mathrm{d}\boldsymbol{r}\right) = U^{*}_{y;i,j,k+1}U^{*}_{z;i,j,k}U_{y;i,j,k}U_{z;i,j,k}, \tag{3.2.10}$$

and the remaining terms $\mathcal{F}_{U_y}$, $\mathcal{F}_{U_z}$, $W_{y;i,j,k}$ and $W_{z;i,j,k}$ are defined similarly from cyclic permutation of Eqs. (3.2.9) and (3.2.10). The local discretised magnetic field

$$B_{\mu;i,j,k} = B_{\mu}\left(\boldsymbol{r}_{i,j,k} + 0.5\sum_{\mu'\neq\mu} h_{\mu'}\hat{\boldsymbol{e}}_{\mu'}\right) \tag{3.2.11}$$

can be subsequently calculated as

$$B_{\mu;i,j,k} = h_{\mu}\frac{1 - W_{\mu;i,j,k}}{\imath\prod_{\mu'} h_{\mu'}}. \tag{3.2.12}$$

Boundary conditions Eqs. (2.3.58) and (2.3.59) at the edges of the domain can similarly be implemented using a ghost point method [78] on the discretised forms of Eqs. (3.2.2) and (3.2.3).

This discretisation scheme introduced by Gropp et al. remains gauge invariant throughout. The state variables are also both bounded in magnitude, as Eq. (3.2.7) ensures the magnitude of link variables remains the same at all timesteps. Furthermore, as an explicit time-stepping scheme, the time evolution of the order parameter (or link variables) at mesh nodes (or links) is readily amenable to parallel solution strategies at each time step, as state variables at the next timestep only depend on the state at the current timestep, and crucially do not depend on the state of the system at any adjacent nodes at the next timestep.

However, as an explicit time-stepping scheme, the maximum timestep δt is restricted by the requirement that the algorithm must be stable with respect to time evolution. This restriction is often parametrised in terms of the Courant-Friedrichs-Lewy (CFL) condition, which depends on the discretisation scheme employed [78]. Assessing the stability of a nonlinear scheme such as Eqs. (3.2.6) and (3.2.7) is, in general, difficult, but estimates can be made by comparison to the stability of various terms within it. For example, stability of the diffusive terms in the time evolution of the link variable phase in Eq. (3.2.7) can be estimated via the CFL condition for the 3D diffusion equation,

$$\partial_t u = k\nabla^2 u, \tag{3.2.13}$$

which, for central differenced spatial derivatives and a forward Euler timestepping method, is only stable provided

$$C_{\mathrm{CFL}} = 2\delta t \sum_{\mu} \frac{k}{h_\mu^2} < 1. \tag{3.2.14}$$

Comparison with Eqs. (2.3.57) and (3.2.7) implies $k = \kappa^2$, and $\delta t < 1/2\kappa^2 \sum_\mu h_\mu^{-2}$ [74]. The timestep δt is therefore significantly limited when simulations of high-κ superconductors are of interest, particularly as $h_\mu < 1$ is required in order to resolve physics on the scale of the coherence length. Common technological superconductors such as $\mathrm{Nb_3Sn}$ (with typical values for $\kappa \approx 30 - 50$) and YBCO (with an anisotropic κ ranging upwards from $100 - 1000$ depending on direction) unfortunately fit this category [55].

Due to this limitation in the timestep size of the explicit method, different formulations are therefore needed to study vortex dynamics in such materials over long timescales. We shall next discuss two strategies for doing so. Firstly, we shall discuss a 2D solver, TDGL-ZEP, based on the work of [74], which utilises a semi-implicit Crank–Nicolson timestepping method to evolve the phase of $\boldsymbol{U}$. Such a method is unconditionally stable for linear problems with respect to the timestep size δt, and thus allows significantly larger timesteps to be used. The second method, TDGL-HIK, reformulates the problem and solves the TDGL equations in the high-κ limit following [54], which permits an efficient, stable and parallelisable solver of Eqs. (2.3.60) to (2.3.62) for large 3D superconducting systems that can be implemented on GPUs.

3.2.2 TDGL-ZEP – The Semi-Implicit Crank–Nicolson Method in the Zero Electric Potential Gauge

In this subsection, we describe the algorithm used in our TDGL-ZEP code, used to solve the TDGL equations Eqs. (2.3.56) and (2.3.57) in the zero electric potential gauge in this thesis for 2D thin film and junction systems, based on the work of [74] and [76]. TDGL-ZEP is written in Fortran 2003, making use of the Intel MKL PARDISO sparse matrix solver [79], and simulations using TDGL-ZEP in this work were performed on the Hamilton high performance computing service at Durham University.

We discuss a limitation arising from the method adopted by [74, 76] when considering systems in which the local magnetic field varies significantly across the domain, that can lead to unreliable convergence and loss of accuracy. To address this, in TDGL-ZEP we solve for all components of the discretised magnetic vector potential in one solution step, leading to better convergence behaviour in the general case at the expense of scalability of the algorithm with system size. We also discuss a limitation arising due to an increase in numerical noise occurring when simulating persistent resistive states in periodic systems, that informs optimal methods used to calculate the critical current density using TDGL-ZEP.

The algorithm presented here may easily be generalised to 3D systems, although we have only applied it in the 2D case in this work [74]. As the inclusion of a spatially varying effective mass is uncommon in these sorts of simulations, we shall present the discretisation scheme here explicitly; spatial variation of the effective mass has previously been included in simulations considered by [75].

3.2.2.1 Spatial Discretisation

The 2D simulation space is first discretised into a regular grid of nodes at points $\boldsymbol{r}_{i\in[1,n_x],j\in[1,n_y]}$ that are separated by a step size h_x and h_y in the x and y directions, as in the case of the explicit solver described in the previous section. The order parameter ψ is calculated on each node and a new set of 'link variables' a^x and a^y that discretise the magnetic vector potential $\boldsymbol{A}$ are defined on links between nodes,

$$\psi_{i,j} = \psi\left(\boldsymbol{r}_{i,j}\right), \qquad a^x_{i,j} = \int_{\boldsymbol{r}_{i,j}}^{\boldsymbol{r}_{i,j}+\widehat{\boldsymbol{\imath}}h_x} A_x \,\mathrm{d}x, \qquad a^y_{i,j} = \int_{\boldsymbol{r}_{i,j}}^{\boldsymbol{r}_{i,j}+\widehat{\boldsymbol{\jmath}}h_y} A_y \,\mathrm{d}y. \tag{3.2.15}$$

This spatial discretisation is shown schematically in the exploded view in Fig. 3.1, alongside a graphical depiction of the relevant dimensions used to describe a typical junction system that we shall study in the next chapter. For thin film simulations using TDGL-ZEP, the normal region N is not present. The discretisation grid is aligned such that all material boundaries lie between nodes, and thus every node can be identified with a single set of material properties α, β and η. This not the case for the effective mass, which is defined on links between nodes,

$$\begin{gathered} \alpha_{i,j} = \alpha\left(\boldsymbol{r}_{i,j}\right), \\ m^{-1}_{x;i,j} = h_x^{-1} \int_{\boldsymbol{r}_{i,j}}^{\boldsymbol{r}_{i,j}+\widehat{\boldsymbol{\imath}}h_x} m^{-1}_{xx} \,\mathrm{d}x, \qquad m^{-1}_{y;i,j} = h_y^{-1} \int_{\boldsymbol{r}_{i,j}}^{\boldsymbol{r}_{i,j}+\widehat{\boldsymbol{\jmath}}h_y} m^{-1}_{yy} \,\mathrm{d}y, \end{gathered} \tag{3.2.16}$$

on the same grid pattern as the link variables a^x and a^y. The observable electric and magnetic fields can be calculated from the link variables,

$$E^{\mu}_{i,j} = -h_\mu^{-1} \partial_t a^{\mu}_{i,j}, \tag{3.2.17}$$

$$B^z_{i,j} = h_x^{-1} h_y^{-1} \left(a^x_{i,j} - a^x_{i,j+1} - a^y_{i,j} + a^y_{i+1,j} \right), \tag{3.2.18}$$

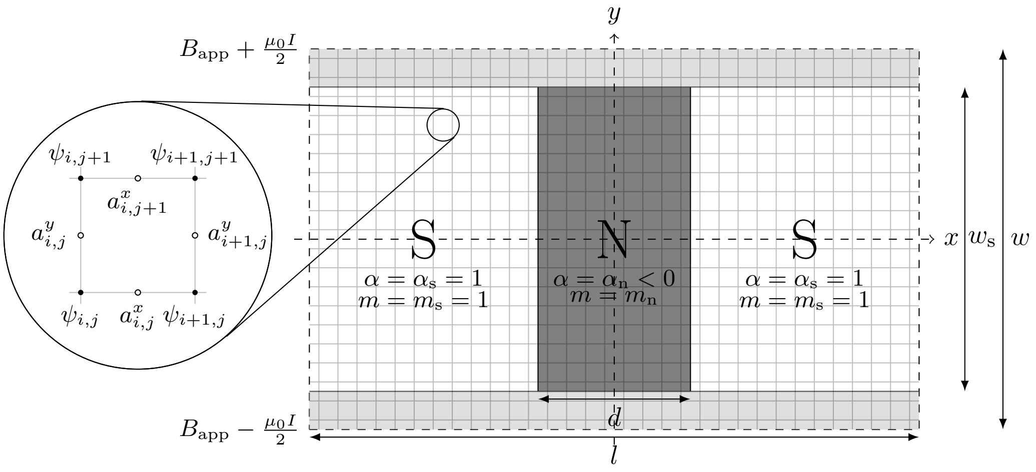

Figure 3.1: Schematic of a 2D computational domain of width w and periodic length l used to model a junction system. The domain is subdivided into three sections; the main superconducting region, S, in which the normalised Ginzburg–Landau temperature parameter $\alpha = 1$ and normalised effective mass $m = 1$, a normal region N described by the normalised Ginzburg–Landau temperature parameter and effective mass α_n and m_n respectively, and a coating region, marked in light grey, in which $\alpha = -10.0$ and $m = 10^8$ when modelling junctions with insulating coatings. The applied field B_{app} and current I are controlled through fixing the local magnetic field at the edges of the computational domain in the y direction. The junction thickness in the direction of current flow is denoted d and the junction width is denoted w_{s} Exploded view: schematic of the location at which the discretised order parameter $\psi_{i,j}$ and modified link variables $a^x_{i,j}$ and $a^y_{i,j}$ relative to the underlying computational grid. Unless otherwise stated, the grid step size is typically taken to be $h_x = h_y = 0.5\xi_{\text{s}}$ in these simulations.

as required.

With these definitions, the spatial discretisation of Eqs. (2.3.56) and (2.3.57) in the zero electric potential gauge ($\varphi = 0$) accurate to second order is

$$\begin{aligned}\eta\partial_t\psi_{i,j} = {}& h_x^{-2}\left[m^{-1}_{x;i-1,j}e^{ia^x_{i-1,j}}\psi_{i-1,j} - \left(m^{-1}_{x;i-1,j} + m^{-1}_{x;i,j}\right)\psi_{i,j} + m^{-1}_{x;i,j}e^{-ia^x_{i,j}}\psi_{i+1,j}\right]\\ &+ h_y^{-2}\left[m^{-1}_{y;i,j-1}e^{ia^y_{i,j-1}}\psi_{i,j-1} - \left(m^{-1}_{y;i,j-1} + m^{-1}_{y;i,j}\right)\psi_{i,j} + m^{-1}_{y;i,j}e^{-ia^y_{i,j}}\psi_{i,j+1}\right]\\ &+ \left(\alpha_{i,j} - |\psi_{i,j}|^2\right)\psi_{i,j}, \qquad (3.2.19)\end{aligned}$$

$$\begin{aligned}\partial_t a^x_{i,j} ={}& \kappa^2 m_{x;i,j}h_y^{-2}\left(a^x_{i,j+1} - 2a^x_{i,j} + a^x_{i,j-1} - a^y_{i+1,j} + a^y_{i,j} + a^y_{i+1,j-1} - a^y_{i,j-1}\right)\\ &+ \operatorname{Im}\left[\psi^*_{i,j}e^{-ia^x_{i,j}}\psi_{i+1,j}\right], \qquad (3.2.20)\end{aligned}$$

$$\begin{aligned}\partial_t a^y_{i,j} =& \kappa^2 m_{y;i,j} h_x^{-2}\left(a^y_{i+1,j} - 2a^y_{i,j} + a^y_{i-1,j} - a^x_{i,j+1} + a^x_{i,j} + a^x_{i-1,j+1} - a^x_{i-1,j}\right)\\ &+ \operatorname{Im}\left[\psi^*_{i,j} e^{-ia^y_{i,j}} \psi_{i,j+1}\right],\end{aligned} \tag{3.2.21}$$

where $m^x_{i,j} = 1/\left(m^{-1}\right)^x_{i,j}$ and $m^y_{i,j} = 1/\left(m^{-1}\right)^y_{i,j}$. We note that these spatially discretised equations remain gauge invariant [74].

Imposing periodic boundary conditions in the x direction requires $\psi_{0,j} \equiv \psi_{nx,j}$, $\psi_{nx+1,j} \equiv \psi_{1,j}$, $a^x_{0,j} \equiv a^x_{n_x,j}$, $a^x_{n_x+1,j} \equiv a^x_{1,j}$, $a^y_{0,j} \equiv a^y_{n_x,j}$, $a^y_{n_x+1,j} \equiv a^y_{1,j}$. In the y direction, the boundary conditions Eqs. (2.3.58) and (2.3.59) are implemented using a ghost point method [78]:

$$\begin{aligned}\eta\partial_t \psi_{i,1} =& h_x^{-2}\left[m^{-1}_{x;i-1,1} e^{ia^x_{i-1,1}} \psi_{i-1,1} - \left(m^{-1}_{x;i-1,1} + m^{-1}_{x;i,1}\right)\psi_{i,1} + m^{-1}_{x;i,1} e^{-ia^x_{i,1}} \psi_{i+1,1}\right]\\ &+ h_y^{-2}\left[\left(h_y\gamma - m^{-1}_{y;i,1}\right)\psi_{i,1} + m^{-1}_{y;i,1} e^{-ia^y_{i,1}}\psi_{i,2}\right]\\ &+ \left(\alpha_{i,1} - \left|\psi_{i,1}\right|^2\right)\psi_{i,1},\end{aligned} \tag{3.2.22}$$

$$\begin{aligned}\eta\partial_t \psi_{i,n_y} =& h_x^{-2}\left[m^{-1}_{x;i-1,n_y} e^{ia^x_{i-1,n_y}} \psi_{i-1,n_y} - \left(m^{-1}_{x;i-1,n_y} + m^{-1}_{x;i,n_y}\right)\psi_{i,n_y}\right.\\ &\left.+ m^{-1}_{x;i,n_y} e^{-ia^x_{i,n_y}} \psi_{i+1,n_y}\right]\\ &+ h_y^{-2}\left[m^{-1}_{y;i,n_y-1} e^{ia^y_{i,n_y-1}} \psi_{i,n_y-1} + \left(h_y\gamma - m^{-1}_{y;i,n_y-1}\right)\psi_{i,n_y}\right]\\ &+ \left(\alpha_{i,n_y} - \left|\psi_{i,n_y}\right|^2\right)\psi_{i,n_y},\end{aligned} \tag{3.2.23}$$

$$\begin{aligned}\partial_t a^x_{i,n_y} =& \kappa^2 m_{x;i,n_y} h_y^{-2}\left(-a^x_{i,n_y} + a^x_{i,n_y-1} + a^y_{i,n_y-1} - a^y_{i+1,n_y-1}\right)\\ &- \kappa^2 m_{x;i,n_y} h_x h_y^{-1}(B_{\text{app}} + \frac{w}{2}\mu_0 J_{\text{app}}) + \operatorname{Im}\left[\psi^*_{i,n_y} e^{-ia^x_{i,n_y}} \psi_{i+1,n_y}\right],\end{aligned} \tag{3.2.24}$$

$$\begin{aligned}\partial_t a^x_{i,1} =& \kappa^2 m_{x;i,1} h_y^{-2}\left(-a^x_{i,1} + a^x_{i,2} + a^y_{i,1} - a^y_{i+1,1}\right)\\ &+ \kappa^2 m_{x;i,1} h_x h_y^{-1}\left(B_{\text{app}} - \frac{w}{2}\mu_0 J_{\text{app}}\right) + \operatorname{Im}\left[\psi^*_{i,1} e^{-ia^x_{i,1}} \psi_{i+1,1}\right].\end{aligned} \tag{3.2.25}$$

For convenience, we will define the multi-indices μ and ν that specify the link variable $a^\mu = a^u_{i,j}$ and $\psi^\nu = \psi_{i,j}$ respectively as

$$\mu(i,j,u) = \begin{cases} j + (i-1)n_y & \text{for } u = x, \\ n_x n_y + i + (j-1)n_x & \text{for } u = y, \end{cases} \qquad \nu(i,j) = i + (j-1)n_x. \tag{3.2.26}$$

The above equations can be simplified into (where we have adopted the Einstein summation convention for notational simplicity):

$$\partial_t a^\mu = J^\mu_{\mu'} a^{\mu'} + S(\{a,\psi\})^\mu, \tag{3.2.27}$$

$$\partial_t \psi^\nu = L^\nu_{\nu'}(\{a\})\psi^{\nu'} + N(\{\psi\})^\nu, \tag{3.2.28}$$

where the nonlinear terms

$$N(\{\psi\})^\nu = \left(\eta^{-1}\right)^\nu \left(\alpha^\nu - |\psi^\nu|^2\right)\psi^\nu, \tag{3.2.29}$$

and

$$S(\{a,\psi\})^\mu = \begin{cases} \operatorname{Im}\left[\psi^*_{i,j} e^{-ia^\mu}\psi_{i+1,j}\right] & \text{for } u(\mu) = x, \\ \operatorname{Im}\left[\psi^*_{i,j} e^{-ia^\mu}\psi_{i,j+1}\right] & \text{for } u(\mu) = y. \end{cases} \tag{3.2.30}$$

3.2.2.2 Temporal Discretisation

For developing $\{a,\psi\}$ in time, we employ an adapted version of the Crank–Nicolson algorithm [74]. Such a method is known to be unconditionally stable for purely linear sets of equations [78], although stability is not guaranteed in the nonlinear case. Unlike the explicit scheme of Gropp et al. [65], that uses the computational variables $\{U\} = \{\exp(-\imath a)\}$ instead of $\{a\}$ directly, numerical errors of schemes based on [74] will increase for long simulations of periodic systems in resistive states, as the magnitude of $\{a\}$ can grow large over time as a result of Eq. (3.2.17), and the resultant increase in rounding error can slow or even prevent convergence. However, as we are predominantly interested in the critical current density J_c and the onset of persistent resistive states in the system, this does not significantly limit critical current simulations that are the primary focus of this work, provided the system is initialised in the superconducting state. This limitation compared to [65] is outweighed by the reduction in simulation time possible using the longer timesteps that the Crank–Nicolson approach permits when κ is not small, as a result of its greater stability properties.

Applying a Crank–Nicolson approach on all terms in Eqs. (3.2.19) and (3.2.20), we can relate the computational variables at timestep $n+1$ and n by:

$$\frac{a^{\mu}_{n+1}-a^{\mu}_{n}}{\delta t}=\frac{1}{2}\left[J^{\mu}_{\mu',n}a^{\mu'}_{n}+J^{\mu}_{\mu',n+1}a^{\mu'}_{n+1}+S(\{a_n,\psi_n\})^{\mu}+S(\{a_{n+1},\psi_{n+1}\})^{\mu}\right], \tag{3.2.31}$$

$$\frac{\psi^{\nu}_{n+1}-\psi^{\nu}_{n}}{\delta t}=\frac{1}{2}\left[L^{\nu}_{\nu'}(\{a_n\})\psi^{\nu'}_{n}+L^{\nu}_{\nu'}(\{a_{n+1}\})\psi^{\nu'}_{n+1}+N(\{\psi_n\})^{\nu}+N(\{\psi_{n+1}\})^{\nu}\right]. \tag{3.2.32}$$

Rearranging, we arrive at a pair of coupled, nonlinear equations to be solved for our unknown variables $\{a_{n+1},\psi_{n+1}\}$ at each timestep,

$$\mathcal{J}^{\mu,-}_{\mu',n+1}a^{\mu}_{n+1}=\mathcal{J}^{\mu,+}_{\mu',n}a^{\mu'}_{n}+\frac{\delta t}{2}\left[S(\{a_n,\psi_n\})^{\mu}+S(\{a_{n+1},\psi_{n+1}\})^{\mu}\right], \tag{3.2.33}$$

$$\mathcal{L}^{\nu,-}_{\nu'}(\{a_{n+1}\})\psi^{\nu}_{n+1}=\mathcal{L}^{\nu,+}_{\nu'}(\{a_n\})\psi^{\nu'}_{n}+\frac{\delta t}{2}\left[N(\{\psi_n\})^{\nu}+N(\{\psi_{n+1}\})^{\nu}\right], \tag{3.2.34}$$

where we have defined

$$\mathcal{J}^{\mu,\pm}_{\mu',n}=\delta^{\mu}_{\mu'}\pm\frac{\delta t}{2}J^{\mu}_{\mu',n},\qquad \mathcal{L}^{\nu,\pm}_{\nu'}(\{a_n\})=\delta^{\nu}_{\nu'}\pm\frac{\delta t}{2}L^{\nu}_{\nu'}(\{a_n\}). \tag{3.2.35}$$

However, as these equations are nonlinear, an iterative method must be employed at each timestep. Fortunately, since the timescale for the evolution of $\{a\}$ is much shorter than $\{\psi\}$ since usually $\kappa^2 \gg \eta^{-1}$, we have applied a block Gauss-Seidel approach to the fully coupled system [78]. Denoting the m^{th} iteration of our set of unknowns by $\{a^{(m)}_{n+1},\psi^{(m)}_{n+1}\}$ we have

$$\mathcal{L}^{\nu,-}_{\nu'}(\{a^{(m)}_{n+1}\})\psi^{\nu}_{n+1}=\mathcal{L}^{\nu,+}_{\nu'}(\{a_n\})\psi^{\nu'}_{n}+\frac{\delta t}{2}\left[N(\{\psi_n\})^{\nu}+N(\{\psi^{(m)}_{n+1}\})^{\nu}\right], \tag{3.2.36}$$

$$\mathcal{J}^{\mu,-}_{\mu',n+1}a^{\mu,(m+1)}_{n+1}=\mathcal{J}^{\mu,+}_{\mu',n}a^{\mu'}_{n}+\frac{\delta t}{2}\left[S(\{a_n,\psi_n\})^{\mu}+S(\{a^{(m)}_{n+1},\psi^{(m+1)}_{n+1}\})^{\mu}\right], \tag{3.2.37}$$

where we set $\{a^{(0)}_{n+1},\psi^{(0)}_{n+1}\}=\{a_n,\psi_n\}$. However, unlike [74], we do not separate Eq. (3.2.37) into two iteration steps, as the timescale for the evolution of $\{a^x\}$ and $\{a^y\}$ are similar magnitudes, which can lead to oscillatory behaviour of the iteration scheme with a block Gauss-Seidel approach and unreliability of convergence [78]. Equation (3.2.36) is solved directly and more quickly in two steps using the method of fractional steps to decompose the linear operator $\mathcal{L}^{\nu,-}_{\nu'}(\{a^{(m)}_{n+1}\})$ into the product

$\mathcal{L}_{X,\nu'}^{\nu,-}(\{a_{n+1}^{(m)}\})\mathcal{L}_{Y,\nu'}^{\nu,-}(\{a_{n+1}^{(m)}\})$ of two simpler operators containing difference terms in one dimension only [74]. In this geometry, $\mathcal{L}_{X,\nu'}^{\nu,-}$ is a cyclic tridiagonal matrix and $\mathcal{L}_{Y,\nu'}^{\nu,-}$ is a banded tridiagonal matrix, for which fast solution methods are available. Cyclic tridiagonal systems are solved using a Sherman-Morrisson algorithm [80] with the tridiagonal solver provided by the LAPACK package. Equation (3.2.37) is solved in one solution step using the Intel MKL PARDISO direct parallel sparse solver. Factorisation and analysis of the operator $\mathcal{J}_{\mu',n+1}^{\mu,-}$ need only be performed once as the values are time-independent, with the exception of boundary terms that can be grouped with nonlinear terms in Eq. (3.2.37).

Convergence was achieved by solving Eqs. (3.2.36) and (3.2.37) alternately until the maximum residual ε, defined by

$$\varepsilon = \max\left\{\left|a_{n+1}^{(m+1)} - a_{n+1}^{(m)}\right|, \left|\mathrm{Re}\left[\psi_{n+1}^{(m+1)} - \psi_{n+1}^{(m)}\right]\right|, \left|\mathrm{Im}\left[\psi_{n+1}^{(m+1)} - \psi_{n+1}^{(m)}\right]\right|\right\}, \tag{3.2.38}$$

satisfied $\varepsilon < 10^{-7}$ at each time step.

The most common use case of the TDGL-ZEP code in this work is to generate the characteristic behaviour of the critical current J_c as a function of the applied magnetic field B_app. As we will explore in later sections, the critical current density J_c at a given B_app can strongly depend on the magnetic history of the system, and so each J_c value in the $J_\mathrm{c}(B)$ characteristic was determined from a different vortex dynamics simulation and history. Therefore, to reduce the time taken to generate an entire $J_\mathrm{c}(B)$ characteristic, simulations at different applied magnetic fields were applied in parallel on separate compute cores. Within a core, when available, OpenMP was used to allow the Intel MKL PARDISO solver to run in parallel on multiple threads to accelerate the direct solve of the link variables at each solution step.

3.2.2.3 Scaling

As mentioned above, in the original semi-implicit algorithm proposed in [74], Eq. (3.2.37) is separated into two iteration steps for $\{a^x\}$ and $\{a^y\}$ which are solved using the method of fractional steps, allowing the use of fast tridiagonal matrix solving schemes that take $O(n)$ steps to solve for the unknown link variables, where n is the number of link variables being solved for. However, as discussed, since $\{a^x\}$ and $\{a^y\}$ evolve on similar timescales and are, in general, tightly coupled, such a method can (and has been observed to) lead to unreliable convergence of the iteration scheme under the block Gauss-Seidel approach applied [78]. This limitation is unlikely to affect results significantly when the vortex-vortex spacing in the system is much smaller than the penetration depth λ_s, or when the system is in the high κ limit, since in these cases the link variables $\{a^x\}$ and $\{a^y\}$ are determined to leading order by the applied magnetic field, which does not vary significantly across the system in these limits, and any oscillatory convergence can become negligible relative to the tolerance of the simulation. Furthermore, as the original algorithm presented in [74] solves for $\{a_n^x, a_n^y, \psi_n\}$ in three iterations at every timestep rather than iterating until convergence, any oscillatory convergence behaviour manifests as a loss of simulation accuracy.

To address this unreliable convergence arising from decoupling $\{a^x\}$ and $\{a^y\}$ at a given timestep, in TGDL-ZEP we instead solve the coupled system for $\{a^x\}$ and $\{a^y\}$ in one step. However, the direct sparse solver used to do so scales worse with the number of nodes (and therefore link variables) than the efficient tridiagonal approaches. In the worst case, direct matrix solvers take $O(n^2)$ steps to solve [78]. This poor scaling with system size for a given solution step for the link variables limits the maximum size of system that can be simulated using TDGL-ZEP. In particular, this makes any generalisation to 3D systems too computationally intensive to usefully study large 3D superconducting domains of interest for technological superconductors. This is significant, as the scalability of

[74] – despite the concerns regarding convergence raised above – has previously enabled idealised 3D granular systems to be studied [81]. For this reason, we have also implemented a large-scale TDGL solver for systems in the high κ limit, TDGL-HIK, based on the work of [54] that has previously been found to solve the superconducting state at each timestep in $O(n)$ operations and is appropriate for 3D simulations. This solver will be the topic of the next section.

3.2.3 TDGL-HIK – The High-κ Large Scale Solver of Sadovskyy et al.

For large grid sizes, solution of Eq. (3.2.37) with the link variables $\{a_{x,y}\}$ being updated in a single step becomes prohibitively expensive, and thus the algorithm described in Section 3.2.2 scales poorly for 3D systems. In the high-κ limit, Sadovskyy et al. have developed a scalable GPU accelerated algorithm to solve Eqs. (2.3.60) to (2.3.62) to investigate the effect of pinning structures in 3D superconducting systems [54]. For 3D simulations, we have written and implemented a TDGL solver (TDGL-HIK) using the algorithm described in [54] to investigate J_c in large scale polycrystalline systems.

The order parameter ψ, the electrostatic potential φ, and the gauge parameter K are updated successively at each timestep, with ψ and φ solved for iteratively as described in [54] until $|\psi_{n+1} - \psi_n|^2 < 10^{-5}$ and $|\nabla^2\varphi - \boldsymbol{\nabla}\cdot \mathrm{Im}\,[\psi^*(\boldsymbol{\nabla} - \imath\boldsymbol{A})\psi]|^2 < 10^{-5}$ at every mesh point. K is integrated forward in time using a second order Runge-Kutta algorithm [80]. Local order parameter fluctuations may also be included for investigations of vortex creep by adding a temperature dependent noise term $\zeta = \zeta_1 + \imath\zeta_2$ to the right hand side of Eq. (2.3.60) [54]. ζ_1 and ζ_2 are independent random variables at each timestep, taken from the uniform distribution in the interval between $\zeta_\mathrm{max} = \left(3\eta T_\mathrm{f}\delta t h_x h_y h_z/\xi_\mathrm{s}^3\tau\right)^{1/2}$ In this work however, we set $T_\mathrm{f} = 10^{-6}$, which is sufficiently small so as to minimise creep effects that may complicate the determination of J_c and corresponds to nearly zero thermal noise for vortex flow [82], but sufficiently large to speed up relaxation of the order parameter when the system is out of equilibrium, such as immediately after initialisation.

Insulating or (quasi)periodic boundary conditions can be applied at the edges of the simulation domain in any (or all) spatial dimensions [54]. For a periodic domain of size L_x, L_y, L_z in the x, y and z dimensions respectively with a magnetic field applied along the z axis, periodic boundary conditions can be applied to ψ at the edges of the domain in the x and z dimensions, and quasiperiodic boundary conditions (QBC) on ψ in the y dimension, as described in [54]. We found quasiperiodic boundary conditions to be particularly useful to eliminate surface effects in 3D simulations that can otherwise dominate over bulk critical current contributions in computationally accessible system sizes.

TDGL-HIK was written using CUDA and C++ for simulation on NVIDIA GPUs. GPU devices can contain hundreds of processing units, and can drastically improve the performance of highly parallelisable algorithms and solution steps [83]. However, copying data to the global memory of a GPU device from a host CPU (and vice versa) is a slow process, limited by the PCIe bus that connects the two, and so GPU simulation is most beneficial when only small amounts of data are needed to be transferred to and from the GPU during simulation. Due to the formulation of the TDGL solver in the high-κ limit described in [54], the only data needed to be transferred to the CPU from the GPU during a given simulation is information needed to calculate the average value of the electric field $\langle E_{\mathrm{x}} \rangle$ to update the global gauge constraint parameter K, along with some boolean flags to indicate convergence. Otherwise, other large arrays, such as those that store the order parameter and electrostatic potential at every node, are stored in global memory of the GPU, and are updated via kernels that operate using one GPU thread per node. The maximum size of the computational system that can be studied is limited by the available GPU memory; a typical simulation on a cubic domain containing $300^3 = 2.7 \times 10^7$ nodes (for a $(150\xi_{\mathrm{s}})^3$ simulation volume) took 2850 MB of GPU memory, implying a maximum $480^3 \approx 1.1 \times 10^8$ nodes that can be simulated on a NVIDIA GPU with 12 GB of memory, corresponding to a $(240\xi_\mathrm{s})^3$ simulation volume. Simulations using TDGL-HIK were carried out using the resources of the NVIDIA CUDA centre at Durham University.

3.3 Steady States

The simplest simulations that can be performed using TDGL-ZEP and TGDL-HIK are those of vortex distributions at fixed applied magnetic fields, without the application of transport currents through the system. In the bulk of homogeneous superconductors, regular triangular vortex lattices are expected (see Fig. 2.4), with each vortex aligned along the applied magnetic field axis and surrounded by six nearest neighbours in the lowest energy configuration. However, for systems containing flux pinning sites and surface barriers, the number and distribution of vortices present in the steady state is hysteretic, and depends on the magnetic history of the sample, as several different vortex states in the superconductor can be stable at the same applied field.

The particular distribution of vortices in the equilibrated vortex state at a given applied field found in these TDGL simulations is sensitive to numerical noise and the rate of increase of the applied magnetic field. This is because variations in initial vortex penetration locations can introduce defects into the vortex lattice. Any defects in the vortex lattice from the initial magnetic field ramp can then become ‘frozen in’, as low levels of numerical noise in the simulation can inhibit further vortex nucleation and entry into the superconductor and decreases the probability of a transition from one metastable vortex arrangement to another, more stable one. This effect is particularly important when strong surface barriers are present, such as those that exist at interfaces with insulating regions. Furthermore, the number of such lattice defects increases in high magnetic fields since the density of vortices is higher, and equilibration times for high field states are longer as a result. Such a crossover to a defect-dominated vortex lattice at high magnetic fields has previously been observed in both experiment and simulation in [84].

Therefore, for reproducibility of simulations carried out using TDGL-ZEP, the system is first initialised in the Meissner state throughout the computational domain ($\psi = 1$, $B = 0$). The external magnetic field is then increased rapidly at a rate of $5 \times 10^{-2} B_{\mathrm{c2}} \tau^{-1}$ up to the desired value B_{app}, during which time vortices penetrate the superconductor. Finally, the system is left to equilibrate for a duration t_{hold} to allow the vortex distribution to relax into a stable configuration. This rate, along with the tolerance used in the convergence criterion Eq. (3.2.38) was chosen to be slow enough (and small enough) to minimise the number of defects in the vortex state, whilst remaining large enough to allow simulations to equilibrate and relax in reasonable timescales. An example of such a configuration for a TDGL-ZEP simulation on a superconducting thin film system subject to a parallel magnetic field is provided in Fig. 3.2. An approximately triangular vortex lattice is observed in the centre of the film. However, close to the insulating surfaces, rows of vortices are observed due to the strong surface barriers at the interfaces with the surrounding insulator. This results are consistent with arrangements of vortices found in previous simulations carried out by [85].

For simulations carried out using TDGL-HIK, the order parameter is similarly initialised to the Meissner state value of $\psi = 1.0$ within the entire domain, and the magnetic field throughout the system is set to its applied value B_{app} directly through the link variables as described in [54]. As noted in [54], the rate at which vortices nucleate and relax is controlled by the fluctuation parameter ζ_{max} and the associated effective temperature T_{f}. As discussed in Section 3.2.3, in this work we follow [82] and set $T_{\mathrm{f}} = 10^{-6}$, to minimise effects of vortex creep in critical current density simulations, but still allow sufficient equilibration for initial vortex states. A snapshot of a simulation using TDGL-HIK after initial vortex nucleation but prior to full relaxation of the vortex state is presented in Fig. 3.3. Whilst most vortices are indeed locally surrounded by six other nearest neighbours and are aligned along the axis of the applied field, defects in the vortex lattice are clearly

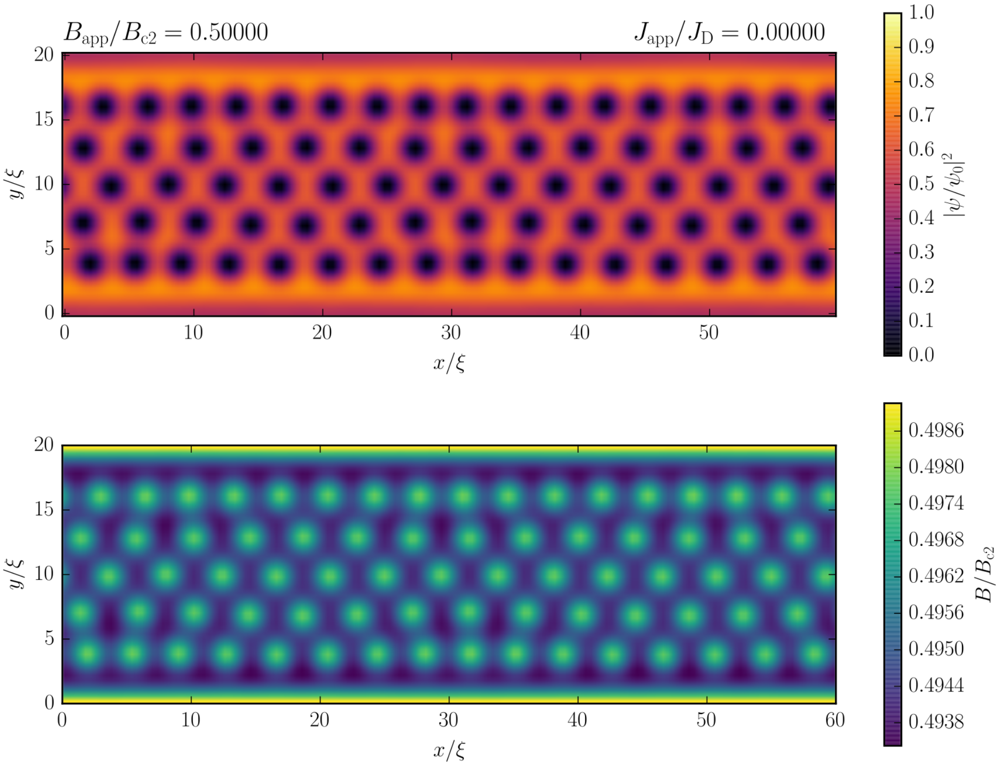

Figure 3.2: Normalised Cooper pair density $|\psi|^2$ (top) and local magnetic field B (bottom) in a superconducting film with $w = 20\xi$, $l = 60\xi$, $\eta = 1$ and $\kappa = 10$ in an applied external magnetic field $B_{\mathrm{app}} = 0.5B_{\mathrm{c2}}$, equilibrated for $10^4\tau$. The system is periodic in the x-direction and insulating boundary conditions were applied in the y-direction.

visible, as well as curvature of individual vortex lines.

Understanding the reasons for differences in the initial vortex state will be important for understanding sources of noise in the determination of the critical current density from these simulations when a transport current is applied. Different distributions and numbers of vortices and vortex lattice defects in the initial state can lead to different values of the critical current density. We shall discuss these effects, and methods of extracting critical current densities from these simulations reproducibly despite this limitation, in the next section.

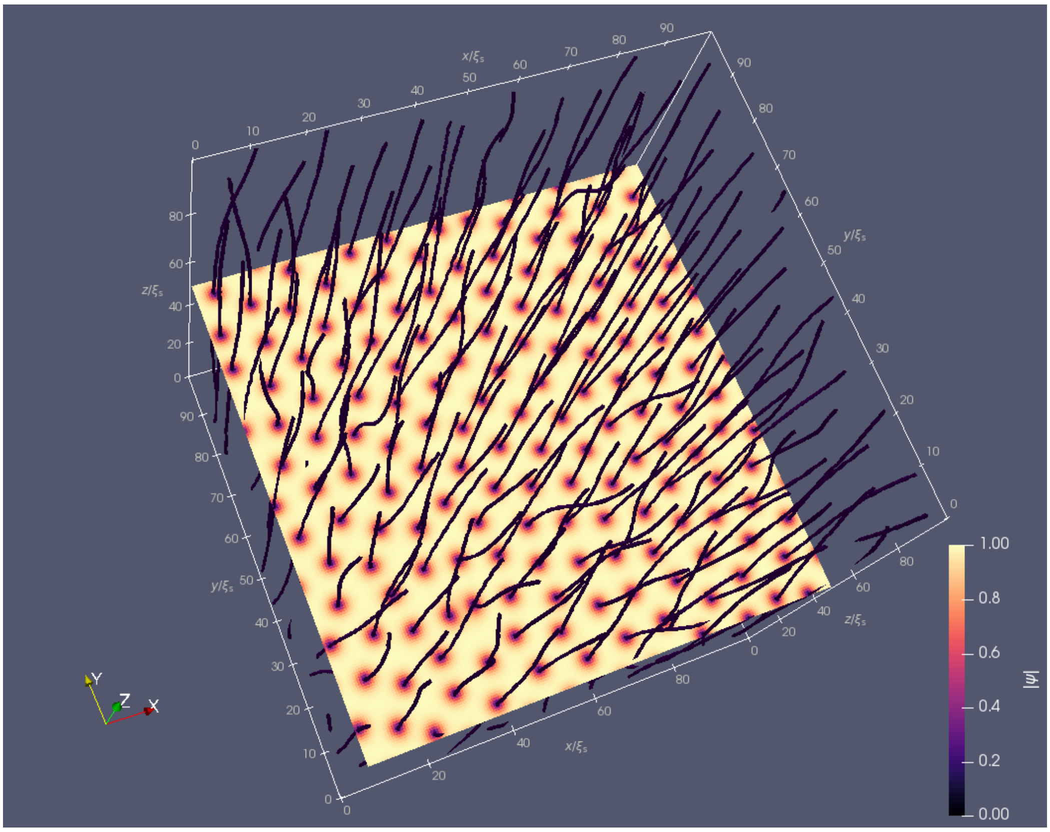

Figure 3.3: Normalised Cooper pair density $|\psi|^2$ in a 2D slice of a 3D cubic superconducting domain of side length $100\xi_s$ with $\eta = 5.79$ in an applied external magnetic field $B_{\mathrm{app}} = 0.1B_{\mathrm{c2}}$ in the z direction, with timestep 0.1τ equilibrated for $10^3\tau$. The system is periodic in all three dimensions. Vortices above and below the midplane are represented by contours of the order parameter at which $|\psi| = 0.25$.

3.4 Critical Current Determination

In order for us to study how the critical current density of a superconducting system is affected by changes in the pinning landscape and applied field, a procedure is needed to extract representative values of the critical current density of the system from vortex dynamics simulations performed using TDGL-ZEP and TDGL-HIK. In this section, we describe the methods used to extract values for J_c, and discuss possible artifacts that may arise from each method.

3.4.1 Continuous Current Ramp

For initial simulations of critical currents in thin film and junction systems using TDGL-ZEP, we adopted a method similar to that used previously used in [86] and in experiment, of continuously increasing the applied transport current through the system and monitoring the average electric field along the x-direction $\langle E_x \rangle$ in the system. We have previously described this method and presented results on small systems using this method in [77]; we include the key results obtained here. The average applied transport current density J_{app}, applied through the boundary conditions of the magnetic field (Fig. 3.1), was increased at a constant rate of $3 \times 10^{-4} J_{\mathrm{D}} \tau^{-1}$ whilst the average electric field along the x-direction $\langle E_x \rangle$ in the system was computed at each time step using Eq. (3.2.17). In this way, a simulated $E(J)$ characteristic for the superconducting system can be generated. To extract a critical current density J_{c} from this characteristic, Ekin's offset criterion method [56] was applied. When the average electric field in the system $\langle E_x \rangle$ first exceeded a critical average electric field $E_{\mathrm{c}} = 0.01\phi_0/2\pi\xi\tau$ in the system, the local tangent to the $E(J)$ characteristic was found and extrapolated to zero electric field; J_{c} was taken to be the corresponding current density at this point. This process was repeated at different applied magnetic fields B_{app} to investigate the $J_{\mathrm{c}}(B)$ dependence of a given system, in analogy to similar experimental methods.

$E(J)$ characteristics of the thin film system shown in Fig. 3.2 subject to insulating boundary conditions at the upper and lower surfaces are shown in Fig. 3.4. For low currents, almost dissipationless behavior is observed. For intermediate currents at low applied magnetic fields, temporal oscillations in the average electric field in the film are observed due to the entry/exit of entire rows of vortices across the upper/lower surface barriers of the film. The vortex rows travel across the film with a current-dependent velocity, and thus these electric field oscillations have a corresponding current-dependent period. At higher fields, the defect density in the vortex lattice increases and these electric field oscillations become less clearly

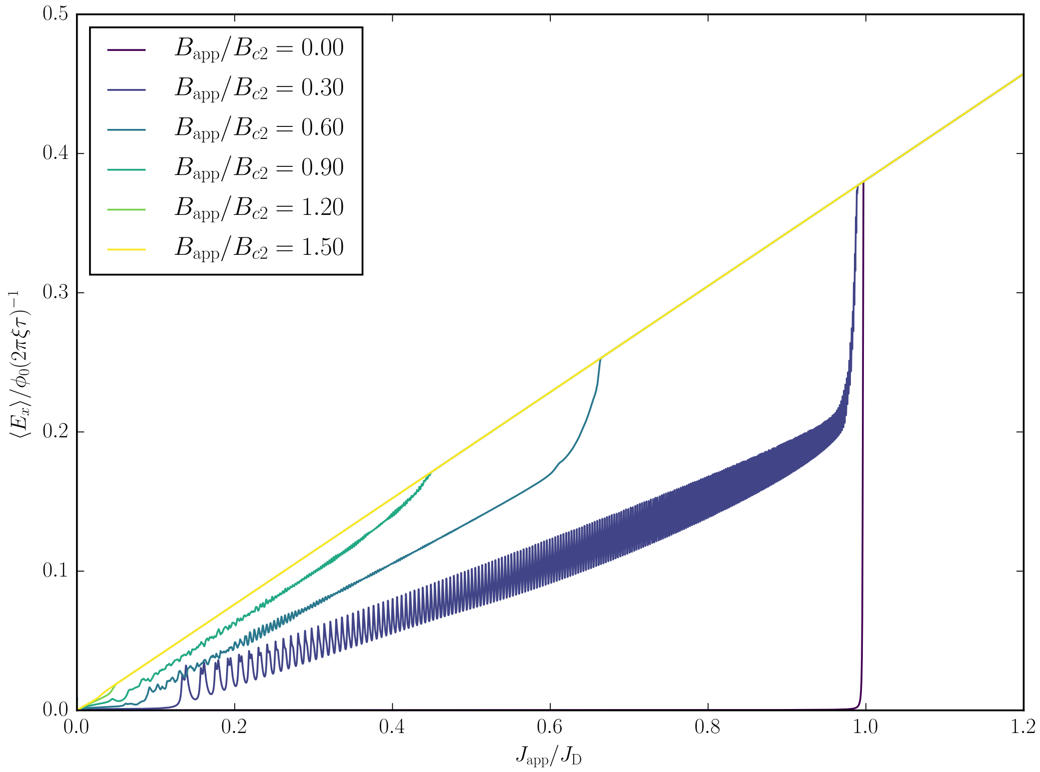

Figure 3.4: Average electric field $\langle E_x \rangle$ against external applied current J_{app} for a superconducting film with $w = 20\xi$, $l = 60\xi$, $\eta = 1$ and $\kappa = 10$ subject to various external magnetic fields. Periodic boundary conditions were applied in the x-direction and insulating boundary conditions were applied in the y-direction. Systems were first initialised in the bulk Meissner state and the external magnetic field B_{app} was raised to the desired value. The external current density J_{app} was then slowly swept up to above the depairing current J_{D}.

defined, as defect motion and the entry/exit of individual vortices dominates over the coherent motion of vortex rows. Eventually, as the applied average current density in the film is increased further, the superconducting film transitions into the (resistive) normal state. This transition becomes less abrupt as the applied magnetic field is increased.

Figure 3.5 displays the critical current density as a function of applied magnetic field for superconducting films of varying widths of the superconductor, subject to both highly metallic ($|\gamma| \to \infty$) and insulating surface conditions ($|\gamma| \to 0$). At applied magnetic fields much lower than the initial vortex penetration field of the film, the critical current density of films with insulating surface conditions is

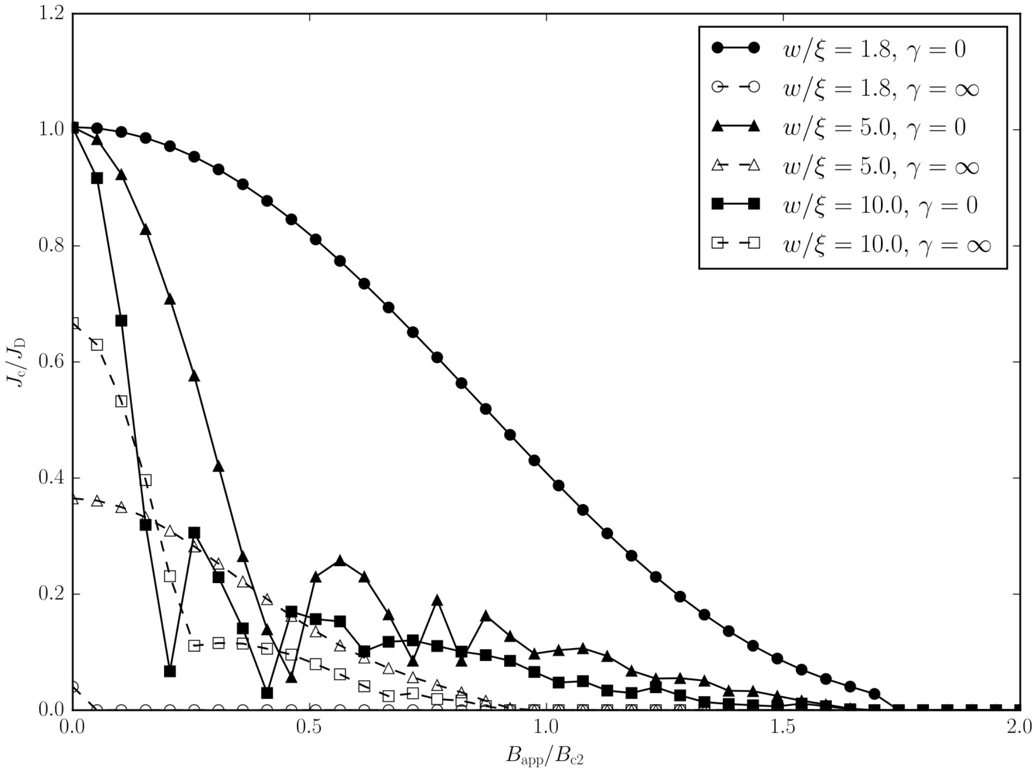

Figure 3.5: Critical current density J_c against mean external magnetic field B_{app} for a superconducting system with $\kappa = 10$, $\eta = 1$ and $l = 60\xi$ for varying width w and surface parameter γ, where $\gamma = \infty$ represents highly conductive boundaries and $\gamma = 0$ represents insulating boundary conditions. J_c and B_{app} are expressed in units of the depairing current J_D and the upper critical field B_{c2} for each superconductor respectively. The critical current was determined using Ekin's offset method using a critical electric field $E_c = 0.01\phi_0/2\pi\xi\tau$ and extrapolating to $\langle E_x \rangle = 0$.

large, and close to the depairing current density J_D. For films with highly metallic boundary conditions, the critical current density in this regime tends to zero as the film width decreases, as a result of the suppression of Cooper pair density close to the highly metallic surfaces. The effect of the surface parameter γ on the magnetisation of superconducting films in the same geometry has been previously considered in [87].

In low magnetic fields, of the order of the initial vortex penetration field in the film, the critical current density of wide films exhibits a (distorted) Fraunhöfer-like dependence with applied magnetic field. For these films, the critical current density of the film decreases to zero as the applied field is raised above B_{c2} for films subject to highly metallic surface conditions, or above $B_{\mathrm{c3}} = 1.69 B_{\mathrm{c2}}$ for films subject to insulating surface conditions. The critical current density can remain non-zero up to extremely high applied magnetic fields in very thin films with insulating surfaces, depending on their width. High resolution simulations with a grid spacing of 0.1ξ suggest that the field at which the critical current density does vanish for thin films is close to the parallel critical field of the film $B_{\mathrm{c}||} = 2\sqrt{3} B_{\mathrm{c2}} \xi / w$, consistent with Tinkham's predictions [88].

Next, the effect of including a junction region in the thin film on the $E(J)$ characteristic obtained using this continuous current ramp method was investigated. Figure 3.6 shows that the $E(J)$ characteristics of the thin film system are modified when a junction consisting of a weaker superconductor than the bulk with $\alpha_{\mathrm{n}} = 0.8$ is added to the film. At large applied current densities, in zero magnetic fields electric field oscillations are introduced, as a result of vortex-antivortex motion along the junction. Furthermore, in all magnetic fields, the transition to the normal state at high current densities is broadened. This occurs because a non-zero Cooper pair density persists just outside the junction region that carries an associated supercurrent, although most of the superconducting film itself is in the normal state.

Finally, the effects of varying the junction properties on the zero field $E(J)$ characteristic of the film containing a junction are displayed in Fig. 3.7. When α_{n} is reduced, the critical current density decreases and in the high E-field regime, the transition to the normal state broadens and the current density required to drive the whole system into the normal state increases. This behaviour has previously been observed in simulations by Berdiyorov et al. for the specific case of $\alpha_{\mathrm{n}} = -1$ [89]; our results in Fig. 3.7 show that this broadening is strongly dependent on the junction T_{c}.

Defects in the initial vortex lattice introduce noise in the simulated $E(J)$ characteristics of the film at low applied currents, but provided they are sufficiently few in number, they do not significantly affect the determination of the critical

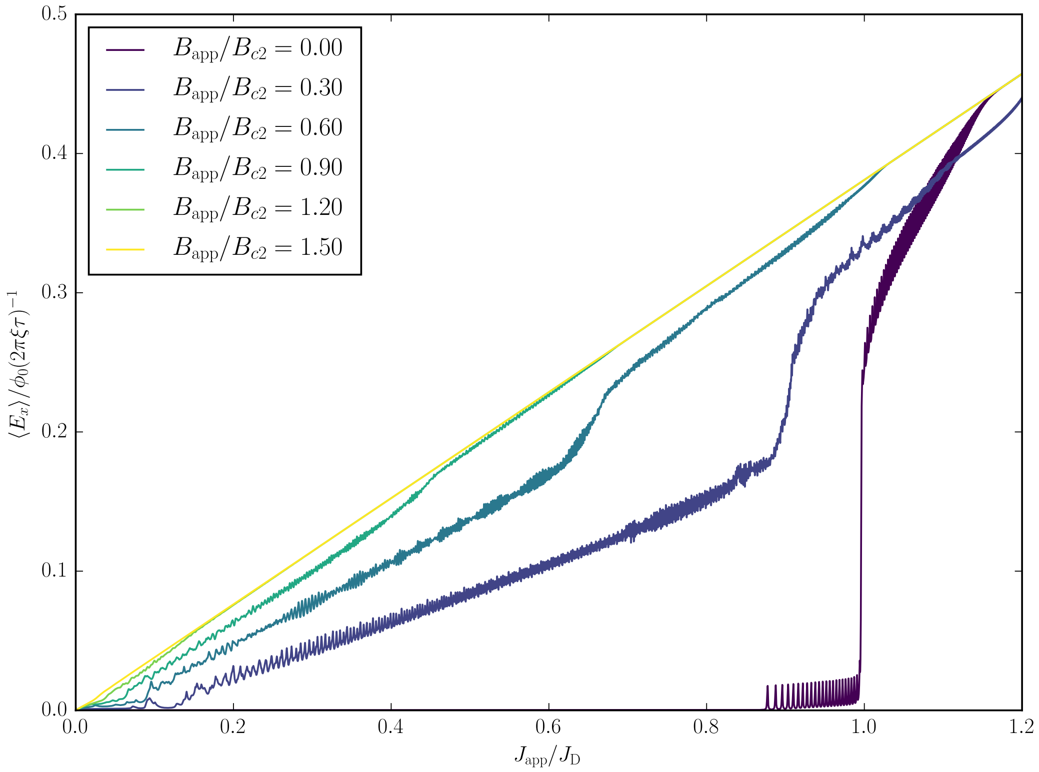

Figure 3.6: Average electric field $\langle E_x \rangle$ against external applied current J_{app} for a superconducting film containing a 2ξ wide 'junction' region in its centre, in which the local T_{c} term $\alpha_{\mathrm{n}} = 0.80$. The surrounding superconducting domain was parameterised with $\eta = 1$, $\kappa = 10$ and dimensions $w = 20\xi$ and $l = 60\xi$, with periodic boundary conditions applied in the x-direction and insulating boundary conditions applied in the y-direction. At each external magnetic field, the system was first initialised in the bulk Meissner state and the external magnetic field B_{app} was raised to the desired value. The external current density J_{app} was then slowly swept up to above the depairing current J_{D}.

current density of the system provided the offset criterion E_{c} is large enough. In high magnetic fields, when the number of defects in the vortex lattice is larger, the resultant $E(J)$ characteristics are unavoidably noisier than in the low field case. This can affect the $E(J)$ characteristics since relaxation of the vortex lattice under small applied currents can generate significant transient electric fields as the vortex lattice relaxes from an initial metastable state (c.f. Fig. 3.4).

As we have seen, a notable advantage of the continuous current ramping method is that the $E(J)$ characteristics obtained can be easily interpreted, with steps and oscillations in the $E(J)$ characteristic easily compared to the movements of vortices

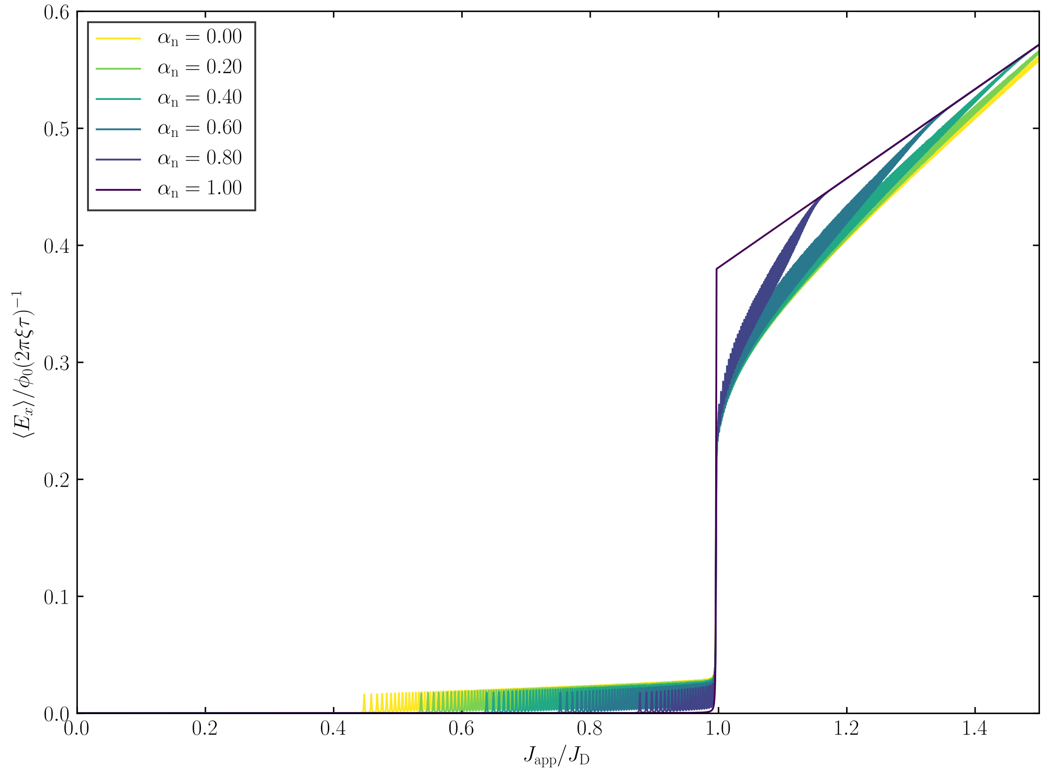

Figure 3.7: Average electric field $\langle E_x \rangle$ against external applied current J_app for a superconducting film containing a 2ξ wide ‘junction’ region in its centre, in which the local T_c term α_n is variable. The surrounding superconducting domain was parameterised with $\eta = 1$, $\kappa = 10$ and dimensions $w = 20\xi$ and $l = 60\xi$, with periodic boundary conditions applied in the x-direction and insulating boundary conditions applied in the y-direction. At each external magnetic field, the system was first initialised in the bulk Meissner state and the external magnetic field B_app was raised to the desired value. The external current density J_app was then slowly swept up to above the depairing current J_D.

observed in snapshots of the order parameter and field distributions. Furthermore, it has the additional advantage that critical current densities corresponding to lower electric field criteria with all other simulation parameters held constant can easily be obtained by postprocessing the same $E(J)$ characteristic, saving time that would otherwise need to be spent rerunning the simulation. However, oscillations and noise in the $E(J)$ characteristic close to the electric field criterion E_c can lead to significant uncertainty in critical current densities obtained using Ekin’s offset method, and cause large amounts of scatter in the inferred $J_\mathrm{c}(B)$ characteristics unless the onset of vortex flow in the system as a function of applied current is sufficiently sharp. Furthermore, the finite continuous current ramp rate provides an inductive contribution to the average electric field in the system that limits the minimum value of E_c that can be used; slower ramp rates permit smaller values of E_c, but lead to longer simulation timescales.

At this juncture, it is useful to compare the characteristic timescale τ and the characteristic electric field $E_0 = \phi_0/2\pi\xi\tau$ to a typical superconductor. For a superconductor with $\kappa = 30$, $B_{\mathrm{c2}}(T) = 10\,\mathrm{T}$ and normal state resistivity $\rho_{\mathrm{N;s}} = 1\,\mathrm{\mu\Omega\,m}$, we have $\xi \approx 6\,\mathrm{nm}$, $\tau \approx 4 \times 10^{-2}\,\mathrm{ps}$, and thus $E_0 \approx 2\,\mathrm{MV\,m^{-1}}$. Therefore, the electric field criterion used in this approach, $E_\mathrm{c} = 0.01E_0$ is around ten orders of magnitude larger than a typical $E_\mathrm{c} = 100\,\mathrm{\mu V\,m^{-1}}$ criterion used in experimental superconductor characterisation [56]! Unfortunately, using such a small electric field criterion for J_c is not feasible on achievable timescales for the reasons given above, not least because it would require an extremely slow current ramp rate for the inductive contribution to remain below $E_\mathrm{c} = 100\,\mathrm{\mu V\,m^{-1}}$. Nevertheless, we are motivated to investigate alternative procedures for critical current determination that can accommodate lower electric field criteria, to facilitate faster generation of $J_\mathrm{c}(B)$ characteristics with reduced computational cost and scatter in extracted J_c values.

3.4.2 Ramp-and-Hold

A common method used in the literature to address the problem of oscillations in the $E(J)$ characteristic when determining critical currents is to average the electric field at a given current over a time period larger than the period of oscillations [90]. In doing so, the $E(J)$ characteristic is smoothed, and methods to extract J_c from the $E(J)$ characteristic are stabilised. We adopt such a method for our TDGL-HIK simulations, following [90].

In this approach, the system is initialised in a resistive state by driving a large average applied current density $J_{\mathrm{app}} \gg J_\mathrm{c}$ through the domain. The applied average current density J_{app} was then decreased in a series of logarithmically spaced steps; typically, the ratio between the transport current applied at successive current steps $r_J \approx 0.975$, representing a 2.5% decrease in the applied current at each current step. After each current step, the current is held constant for a duration of t_{hold} and the spatially averaged electric field in the superconductor E_x is averaged over the second half of the hold step, after transient effects from stepping the current have decayed away. Typically $t_{\text{hold}} = 10.0\ \tau$. The critical current density J_{c} is then taken to be the highest current at which the time-averaged and spatially-averaged E_x is less than the electric field criterion $E_{\text{c}} = 10^{-5}\rho J_0$.

It should be noted that critical current densities obtained from such a method may underestimate the critical current density of the system at the specified electric field criterion, as vortices will not immediately stop moving once J_{c} is reached, and so the current ramp may overshoot and set the current to a lower value than J_{c} if r_J or t_{hold} are too small. Nevertheless, we find that such a method is highly efficient for generating representative J_{c} behaviour, and requires relatively little computational time compared to other approaches.

3.4.3 Adaptive Current Ramp

However, as we have noted in Section 3.2.2, simulations of TDGL-ZEP can become unstable for when simulations spend extended periods of time in resistive states, and so the ramp-and-hold method cannot be directly used. For TDGL-ZEP simulations therefore, it is necessary to ramp the applied current up from the superconducting state to the onset of a net electric field in the system, rather than down from the resistive state. However, using an averaging approach on the $E(J)$ characteristic at each applied current with an increasing current ramp can take long periods of simulation time in stable regions, where vortices are not moving. To minimise computational expense, it is therefore preferable to adopt an adaptive current ramping method, that spends most of this averaging time under conditions in which vortices are moving in the system, that could correspond to the onset of persistent vortex motion and J_c. To this end, in this subsection we shall describe the adaptive current ramping method we have developed that we shall use throughout the remainder of this thesis for determination of J_c from TDGL-ZEP.

We once again follow the experimental approach [91] and use an arbitrary electric field criterion E_c. To accommodate any variations in the local resistivity (or effective mass) in the system without needing rescaling of the electric field criterion, we express this electric field criterion in terms of a characteristic electric field E_D, which corresponds to the average electric field in the system when the superconductor is normal and carrying the zero-field Ginzburg–Landau depairing current density J_D, such that

$$E_\mathrm{D} = \kappa^2 \rho^x_\mathrm{av} J_\mathrm{D}, \tag{3.4.1}$$

where

$$\rho^x_\mathrm{av} = \frac{w}{w_\mathrm{s}} \frac{1}{n_x} \sum_{i=1}^{n_x} \frac{n_y}{\sum_{j=1}^{n_y} \left[(m^{-1})^x_{i,j} \right]}, \qquad J_\mathrm{D} = \frac{2}{3\sqrt{3}} J_0, \tag{3.4.2}$$

and ρ^x_av represents the average resistivity of the system in the x-direction, normalised to the resistivity of a system in the x-direction containing only the superconductor in its normal state.

The vortex state at fixed magnetic field is first found as described in Section 3.3. Following this, for our TDGL-ZEP simulations the applied average current density J_app was increased in a series of logarithmically spaced steps, starting from $10^{-6} J_\mathrm{D}$. Typically, the ratio between the transport current applied at successive timesteps $r_J \approx 1.01$, representing a 1% increase in the applied current at each step. If the average electric field in the system exceeded the electric field criterion, typically $E_\mathrm{c} = 10^{-5} E_\mathrm{D}$, the applied current was instead held constant. When the average electric field continued to persist above E_c for longer than the hold time t_hold, typically taken as $5 \times 10^4 \tau$, the system was determined to have entered a persistent resistive state and J_app at this point is taken to be the critical current density J_c.

An example of the time evolution of the applied current density and average electric field used to extract J_c from the simulation is displayed in Fig. 3.8. The rapid jumps in the average electric field in the system $\langle E_x \rangle$ below the critical current ($t < 1.1 \times 10^4$) are associated with the imposed current steps and the associated steps in the rate of change of the magnetic field in the system. To make the generation of a full $J_\mathrm{c}(B_\mathrm{app})$ characteristic more efficient, we also simulate J_c at different applied fields in parallel, since the simulations for the critical current at given applied fields are independent of one another.

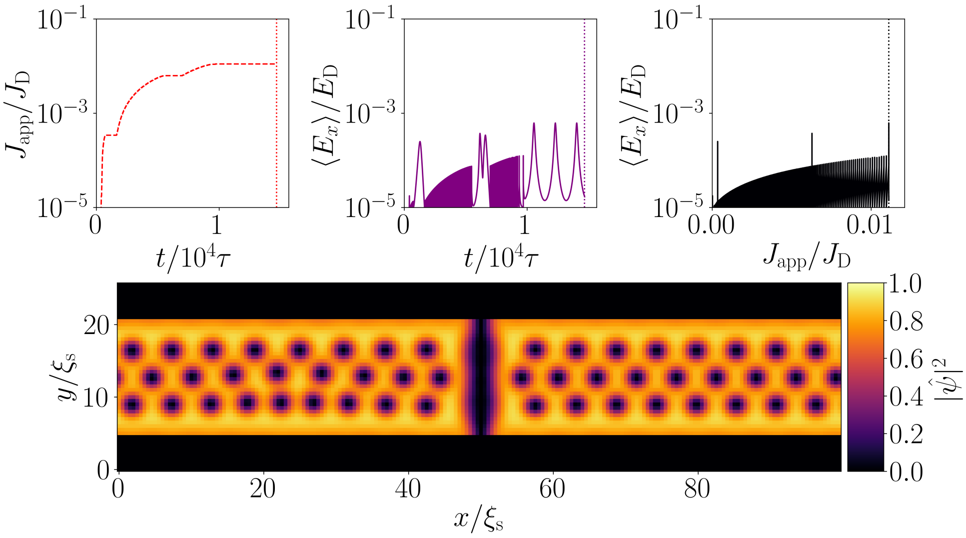

Figure 3.8: Typical simulation data used to extract J_c at the applied field $B_\mathrm{app} = 0.3B_\mathrm{c2}$. Bottom: distribution of the normalised Cooper pair density $|\tilde{\psi}|^2$ at the critical current J_c, for a simulated junction with periodic length $l = 100\xi_s$, thickness $d = 0.5\xi_s$, junction width $w_\mathrm{s} = 16.0\xi_s$ and Ginzburg–Landau temperature parameter in the normal region $\alpha_\mathrm{n} = -20$. Top left: The applied current density J_app normalised by the depairing current density J_D versus time t normalised in units of the characteristic timescale τ. Top centre: The average electric field in the x direction $\langle E_x \rangle$ normalised by the characteristic electric field E_D as a function of time t. Top right: The normalised average electric field in the x direction as a function of the applied current density. The applied current density when $E < E_\mathrm{c} = 10^{-5}E_\mathrm{D}$, and J_c is determined as the lowest current at which $E > E_\mathrm{c}$ for a duration exceeding $t_\mathrm{hold} = 5 \times 10^3\tau$.

3.5 Conclusions

In this chapter, we have outlined the numerical algorithms and methods used within this thesis to solve the TDGL equations in a 2D or 3D superconducting domain, and to evolve the vortex state of a material in time. In particular, we have identified limitations present in the convergence behaviour of the existing scalable TDGL solver of [74] when magnetic field variations are significant within the material. We found significantly improved convergence in these cases by solving for all components of the magnetic vector potential simultaneously at each iteration at the expense of scalability of the solver with system size, and have implemented this in our TDGL-ZEP code. To enable large-scale simulation for high-κ systems, we have also implemented a version of the algorithm developed by [54] for GPU simulation, in TDGL-HIK. We have also described the methods used to extract model $E(J)$ characteristics and representative values for the critical current density J_{c} from vortex dynamics simulations performed using these codes, and the benefits and limitations of the different approaches chosen.

We have also presented results obtained using TDGL-ZEP for simple thin film and junction systems, and found that the critical current density of thin films with insulating surface conditions approaches the depairing current density at applied magnetic fields below the initial vortex penetration field. In contrast, the critical current density of thin films with highly metallic surface conditions decreases to zero as the film width decreases, due to the suppression of the local Cooper pair density close to the metallic surfaces. Furthermore, we have found that the critical current density in very thin films with insulating surfaces subject to applied magnetic fields is limited by the parallel critical field $B_{\mathrm{c}||} = 2\sqrt{3}B_{\mathrm{c}2}\xi/w$, consistent with Tinkham's analytic results. Finally, when narrow junction regions of reduced T_{c} are added to the thin film perpendicular to the direction of current flow, we observe a suppression of the critical current of the system in zero applied magnetic field and a broadening of the transition to the normal state at all applied magnetic fields.

In the next chapter, we shall apply the two main TDGL algorithms implemented here – TDGL-ZEP and TDGL-HIK – to the problem of current flow across a Josephson junction, and validate the critical current densities obtained as a function of field against analytic results. We shall also use TDGL-ZEP to verify new analytic results derived to describe the decrease in critical current density as a function of applied magnetic field for narrow Josephson junctions.

Chapter 4

Simulations of the Critical Current of SNS Josephson Junctions in Arbitrary Magnetic Fields

4.1 Introduction

All large scale superconducting materials are polycrystalline, and contain a range of non-superconducting inclusions and crystal defects such as grain boundaries that may impede current flow. Nevertheless, as predicted by Josephson [92], an electric current may still flow across the system without the onset of dissipation since Cooper pairs are able to tunnel through these ‘normal’ regions. Planar defects in superconducting systems therefore limit the maximum average current density that can flow without the onset of resistance, J_{c}. This can significantly reduce the attainable critical current densities in real materials; indeed, as shown by De Gennes, the critical current density in zero magnetic field that can flow across a thin normal metal sandwiched between two superconducting electrodes decreases exponentially with the thickness of the normal metal layer [27].

In low applied magnetic fields B_{app}, the $J_{\mathrm{c}}(B_{\mathrm{app}})$ behaviour of superconductor-normal-superconductor (SNS) junctions in tunnel-like geometries is well known.

In very narrow systems, and in other geometries in which the current density is constrained to flow in one direction only, the critical current density is independent of applied field to leading order, and depends exponentially on the thickness of the normal barrier in the junction [27, 93, 50]. The local current density in this case is a sinusoidal function of the phase difference between the two superconducting electrodes [93, 50]. When the dimensions of the superconductors become comparable to the (Ginzburg–Landau) penetration depth λ_{s}, the phase difference across the junction varies along the junction, and the (average) critical current density of the junction becomes highly dependent on the system geometry, with $J_{\mathrm{c}}(B_{\mathrm{app}}) \sim B_{\mathrm{app}}^{-1/2}$ for well separated junctions in the thin film limit [94, 95]. For systems larger than λ_{s} but smaller than the Josephson penetration depth λ_{J}, in which self-field effects in the junction region can be neglected, the topological phase difference across the junction varies approximately linearly with position along the junction (except near the junction edges), leading to the well-known Fraunhöfer-like dependence of J_{c} on applied magnetic field with $J_{\mathrm{c}}(B_{\mathrm{app}}) \sim B_{\mathrm{app}}^{-1}$ [96, 97]. For very wide systems, in which the self field associated with the transport current through the junction is comparable to the applied magnetic field, the current-phase relation is multivalued depending on the number of vortices on the junction, and the critical current density depends on the magnetic history of the system [98]. Larger scale networks of SNS junctions have also been used in analytic models for the critical current of polycrystalline superconductors [99, 100], motivating our study of them within this work.

However, these canonical descriptions of SNS Josephson junctions above are all limited to low fields, far below the upper critical field of the superconducting regions, and as such are qualitatively incorrect when the superconductors are in the mixed state or when the order parameter is heavily suppressed by inductive currents. The presence of vortices in the surrounding superconductor strongly affects the critical current density that the junction can carry [101] when vortices are within the penetration depth λ_{s} of the junction. Such models fail entirely as the applied field approaches the upper critical field of the superconductors, as they cannot describe the decrease of J_c to zero when superconductivity is destroyed in the electrodes; no analytic solutions exist for the critical current of junction systems in this high field regime. In the high field regime therefore, numerical studies of the critical current density as a function of field have been employed instead [102].

In particular, time-dependent Ginzburg–Landau (TDGL) theory has been used model the critical current density as a function of applied field for superconducting systems containing normal inclusions [103, 104, 81]. TDGL simulations for the critical current as a function of field of a superconductor containing a periodic series of 'weak link' junctions in which the local temperature $T = T_c$ inside the junctions have been previously carried out [89], but have focussed on the vortex structure and dynamics through the junction rather than how the junction properties affect $J_c(B_{\mathrm{app}})$.

In this chapter we find the first known solutions (to our knowledge) for the critical current density of narrow SNS junctions in arbitrary applied magnetic fields, developing the methodology of [105, 106] to account for the suppression of superconductivity in the superconducting electrodes at applied magnetic fields close to the upper critical field of the system. We verify these solutions against our simulations based on time-dependent Ginzburg–Landau theory. We extend these results to larger systems, up to the scale of λ_s, to find critical current densities as a function of field and find both qualitative agreement with existing surface flux pinning theory for model systems and more importantly, results consistent with widely observed experimental data for superconductors such as Nb_3Sn, Nb_3Al, and $PbMo_6S_8$.

We shall first validate our computational codes against the canonical low-field expressions for the critical current density of junctions, and find good agreement between our simulation and existing theory. We then present our new solutions for the critical current density of narrow junctions in all fields when the junction and superconductors are vortex-free and compare them to simulation. Finally, we propose an extension of these narrow junction results to physically relevant system sizes, and compare them to our simulations and relevant experimental data.

4.2 Weakly Coupled SNS Junctions In Low Magnetic Fields

We shall first review analytic expressions for the critical current density across weakly coupled Josephson junction systems in low fields from the literature, in which the superconducting electrodes either side of the junction do not contain vortices. For simplicity, we shall restrict this analytic discussion to solving the GL equations in the time-independent limit for critical currents in 2D junction systems, valid for thin superconducting films, or volumes of superconducting system in which all vortices are parallel to one another and the junction plane. The system geometry is shown in Fig. 3.1; material parameters $m_i(\boldsymbol{r})$, $\alpha(\boldsymbol{r})$, and $\beta(\boldsymbol{r})$ are only functions of the x coordinate normal to the junction plane. For these systems, it is convenient to express Eqs. (2.3.56) and (2.3.57) in terms of gauge-invariant variables to facilitate physical interpretation of the results. Expressing the order parameter in terms of its magnitude $|\psi|$ and phase θ through the definition $\psi = |\psi| e^{\imath\theta}$, a gauge invariant phase γ can be introduced with gradient $\boldsymbol{\nabla}\gamma = \boldsymbol{\nabla}\theta - \boldsymbol{A}$ defined where $|\psi| \neq 0$. The GL equations expressed in terms of the gauge-invariant variables $|\psi|$, $\boldsymbol{J}_{\mathrm{s}}$, and γ for these junction systems then take the form [105]

$$\left[\sum_i \left(\partial_i \left[m_i^{-1}(x)\,\partial_i\right] - m_i^{-1}(x)\left(\partial_i\gamma\right)^2\right) + \alpha(\boldsymbol{r}) - \beta(\boldsymbol{r})\,|\psi|^2\right]|\psi| = 0, \tag{4.2.1}$$

$$\boldsymbol{J}_{\mathrm{s}} = m_i^{-1}(x)\,|\psi|^2\,\boldsymbol{\nabla}\gamma, \tag{4.2.2}$$

subject to the constraint $\boldsymbol{\nabla}\cdot\boldsymbol{J}_{\mathrm{s}} = 0$. The boundary conditions Eqs. (2.3.58) and (2.3.59) at an insulating surface become $\widehat{\boldsymbol{n}}\cdot\boldsymbol{J}_{\mathrm{s}} = \widehat{\boldsymbol{n}}\cdot\boldsymbol{\nabla}|\psi| = 0$ [93].

For clarity of presentation, we shall categorise junctions by their width w_{s} transverse to the direction of current flow relative to length scales of the superconductor, into 'very narrow' junctions, with $w_{\mathrm{s}} \ll \xi_{\mathrm{s}}, \lambda_{\mathrm{s}}$; 'narrow' junctions, with $\xi_\mathrm{s} \ll w_\mathrm{s} \ll \lambda_\mathrm{s}$, and ‘wide’ junctions, with $w_\mathrm{s} \gg \xi_\mathrm{s}, \lambda_\mathrm{s}$. In addition, it shall be useful to further subcategorize these systems as ‘thin’ or ‘thick’ junctions between weakly coupled ($-\alpha_\mathrm{n} d \gg 1$) superconductors depending on whether its thickness d in the direction of current flow that is much smaller or much larger than the superconducting coherence length ξ_s respectively. Here we consider these different types of junctions in turn.

4.2.1 Very Narrow Junctions $w_\mathrm{s} \ll \xi_\mathrm{s}$

For very narrow junctions with insulating boundary conditions, $w = w_\mathrm{s} \ll \xi_\mathrm{s}$, such that the boundary condition $\hat{\boldsymbol{n}} \cdot \boldsymbol{\nabla}|\psi| = 0$ implies $[\partial_y |\psi|]^{w_\mathrm{s}/2}_{-w_\mathrm{s}/2} = 0$. In this very narrow junction case, no vortices are stable inside the structure and the magnitude of the order parameter $|\psi|$ is approximately constant along the y direction [106, 107]. Hence the mean value theorem can be applied, as Eq. (4.2.1) can be integrated over the junction width in the y direction. $|\psi|$ can then be replaced by its average in the y direction $f = \frac{1}{w_\mathrm{s}} \int_{-w_\mathrm{s}/2}^{w_\mathrm{s}/2} |\psi| \, \mathrm{d}y$ and the components of $\boldsymbol{J}_\mathrm{s}$ by their equivalent average $\langle J_{s;i} \rangle_y = \frac{1}{w_\mathrm{s}} \int_{-w_\mathrm{s}/2}^{w_\mathrm{s}/2} (J_{s;i}) \, \mathrm{d}y$. In the limit where the applied magnetic field is much less than the self field, $J_{s;y} = 0$ from the insulating boundary conditions, and $J_{s;x}$ is independent of y. Eq. (4.2.1) is then reduced to an equation in only one variable x. Using Eq. (4.2.2) gives

$$\partial_x \left(m^{-1}(x) \, \partial_x f \right) + \left[\alpha(x) - \beta(x) f^2 - \frac{m(x) \, \langle J_{s;x} \rangle_y^2}{f^4} \right] f = 0. \tag{4.2.3}$$

This is the same geometry used in Section 2.4.1 to derive the depairing current density J_D for the maximum current density that a very narrow homogenous system can carry. As a result, we shall denote to the maximum current density that a very narrow inhomogeneous system containing a junction can carry by J_DJ. J_DJ is equivalent to the (zero-field) Ginzburg–Landau depairing current density for a junction system; the maximum lossless current density that can flow across the junction, above which superconductivity is destroyed.

4.2.1.1 Thin Junctions $d \ll \xi_\mathrm{s}$

The critical current in the thin junction limit, where $d \ll \xi_\mathrm{s}$, has been solved in weakly coupled limit by [108] and investigated numerically in the strongly coupled case by [109]. To keep things simple here, $\beta(x)$ and $m^{-1}(x)$ are taken as constant across the system. Equation (4.2.3) is written as

$$\partial_x^2 f + \left[1 - (1-\alpha(x)) - f^2 - \frac{\langle J_{s;x}\rangle_y^2}{f^4}\right] f = 0. \tag{4.2.4}$$

Since f and $\langle J_{s;x}\rangle_y$ are continuous across the S/N interface in this case, a constraint between $\partial_x f$ and f at the interface in the limit where $d \ll \xi_\mathrm{s}$ can easily be found, by integrating Eq. (4.2.4) in the x direction across the normal region. Assuming f is symmetric across the junction and $1-\alpha_\mathrm{n} \sim O(d^{-1})$ or larger, then to leading order in d/ξ_s

$$2f'_{d/2} = d\,(1-\alpha_\mathrm{n})\, f_{d/2}, \tag{4.2.5}$$

where $f_{d/2} = f\,(x = d/2)$ and $f'_{d/2} = \partial_x f\,(x = d/2)$.

As shown by [108], in the weak coupling case, when the critical current density of the junction is much less than the critical current density of the bulk superconductors, $\lim_{x\to\infty}\{f\} = 1$ and $\lim_{x\to\infty}\{f'\} = 0$, so that integrating Eq. (4.2.4) from the S/N interface to a point far from the junction yields

$$f'^2_{d/2} + f^2_{d/2} - \frac{f^4_{d/2}}{2} + \frac{\langle J_{s;x}\rangle_y^2}{f^2_{d/2}} = \frac{1}{2}. \tag{4.2.6}$$

Substituting $f'_{d/2}$ from Eq. (4.2.5) into Eq. (4.2.6) and neglecting the highest order terms in the small parameter $V_0^{-1} = 1/d\,(1-\alpha_\mathrm{n})$ gives

$$f^2_{d/2} = V_0^{-2} + V_0^{-1}\sqrt{V_0^{-2} - 4\langle J_{s;x}\rangle_y^2}. \tag{4.2.7}$$

From the discriminant, in order for f to remain positive and real at the S/N interface, $\langle J_{s;x}\rangle_y \;\le\; V_0/2$. This gives the condition for the maximum critical current that can flow through the junction J_DJ as

$$\lim_{d\ll\xi_\mathrm{s}} \{J_\mathrm{DJ}(B_\mathrm{app} = 0)\} = J_0 \frac{\xi_\mathrm{s}}{2d\,(1-\alpha_\mathrm{n})}. \tag{4.2.8}$$

4.2.1.2 Thick Junctions $d \gg \xi_{\mathrm{s}}$

For thick junctions, the critical current density for thick junctions has been solved by [50] from Eq. (4.2.3). In the superconductor regions, with $f_{\mathrm{s}} = f$, $j_x = \langle J_{s;x} \rangle_y$, Eq. (4.2.3) can be written

$$\partial_x^2 f_{\mathrm{s}} + \left[1 - f_{\mathrm{s}}^2 - \frac{j_x^2}{f_{\mathrm{s}}^4} \right] f_{\mathrm{s}} = 0, \tag{4.2.9}$$

whereas inside the normal region, Eq. (4.2.3) can be rescaled with the substitutions $u = x\sqrt{-\alpha_{\mathrm{n}} m_{\mathrm{n}}/m_{\mathrm{s}}}$, $f_{\mathrm{n}} = -f\sqrt{\beta_{\mathrm{n}}/\alpha_{\mathrm{n}}}$ and $j_u = \langle J_{s;x} \rangle_y \beta_{\mathrm{n}} \sqrt{m_{\mathrm{n}}/m_{\mathrm{s}}}(-\alpha_{\mathrm{n}})^{-3/2}$ to give

$$-\partial_u^2 f_{\mathrm{n}} + \left[1 - f_{\mathrm{n}}^2 + \frac{j_u^2}{f_{\mathrm{n}}^4} \right] f_{\mathrm{n}} = 0. \tag{4.2.10}$$

Equations (4.2.9) and (4.2.10) can be solved analytically for the magnitude of the order parameter in terms of Jacobi elliptic functions (Appendix A). From [50], Eq. (4.2.9) has the exact solution for $x > 0$

$$\begin{gathered} f_{\mathrm{s}}^2 = f_{\mathrm{s};l/2}^2 - \frac{\zeta_{\mathrm{s},+}^2 \zeta_{\mathrm{s},-}^2}{\zeta_{\mathrm{s},+}^2 + \zeta_{\mathrm{s},-}^2} \mathrm{sd}^2 \left(\left(\frac{l}{2} - x \right) \sqrt{\frac{\zeta_{\mathrm{s},+}^2 + \zeta_{\mathrm{s},-}^2}{2}}, \sqrt{\frac{\zeta_{\mathrm{s},-}^2}{\zeta_{\mathrm{s},+}^2 + \zeta_{\mathrm{s},-}^2}} \right), \\ \zeta_{\mathrm{s},\pm}^2 = \pm \left(1 - \frac{3 f_{\mathrm{s};l/2}^2}{2} \right) + \sqrt{\left(1 - \frac{f_{\mathrm{s};l/2}^2}{2} \right)^2 - \frac{2 j_x^2}{f_{\mathrm{s};l/2}^2}}, \end{gathered} \tag{4.2.11}$$

where $f_{\mathrm{s};l/2} = f_{\mathrm{s}}(x = \pm l/2)$ is the magnitude of the order parameter at the deepest point inside the electrodes where $\mathrm{d}f_{\mathrm{s}}/\mathrm{d}x = 0$, and Eq. (4.2.10) has the exact solution

$$\begin{gathered} f_{\mathrm{n}}^2 = f_{\mathrm{n};0}^2 + \frac{\zeta_{\mathrm{n},+}^2 \zeta_{\mathrm{n},-}^2}{\zeta_{\mathrm{n},+}^2 + \zeta_{\mathrm{n},-}^2} \mathrm{sd}^2 \left(u \sqrt{\frac{\zeta_{\mathrm{n},+}^2 + \zeta_{\mathrm{n},-}^2}{2}}, \sqrt{\frac{\zeta_{\mathrm{n},+}^2}{\zeta_{\mathrm{n},+}^2 + \zeta_{\mathrm{n},-}^2}}, \right) \\ \zeta_{\mathrm{n},\pm}^2 = \pm \left(1 - \frac{3 f_{\mathrm{n};0}^2}{2} \right) + \sqrt{\left(1 - \frac{f_{\mathrm{n};0}^2}{2} \right)^2 + \frac{2 j_u^2}{f_{\mathrm{n};0}^2}}, \end{gathered} \tag{4.2.12}$$

where $f_{\mathrm{n};0} = f_{\mathrm{n}}(x = 0)$ is the value of the scaled order parameter magnitude f_{n} at the centre of the junction. Equations (4.2.11) and (4.2.12) are solutions of the exact 1D time independent Ginzburg–Landau equations for the junction system; applying boundary conditions at the interface between the normal region and junction gives a relation between the current through the junction and the magnitude of the order parameter at the centre of the normal region, which can be optimised to find the critical current density J_c. For thick junctions, where the order parameter at the centre of the junction is much smaller than that at the S/N boundary, the critical current density for this system of equations can be obtained in the form [50]:

$$\begin{aligned}\lim_{d\gg\xi_\mathrm{s}}\left\{J_\mathrm{DJ}(B_\mathrm{app}=0)\right\} &= 4J_0\frac{1-\sqrt{1-sf_{d/2}^2}}{sv}\exp\left(-\frac{d}{\xi_\mathrm{n}}\right),\\ f_{d/2}^2 &= \frac{v^2+1-\sqrt{v^2(2-s)+1}}{v^2+s},\end{aligned} \tag{4.2.13}$$

where

$$v=\frac{m_\mathrm{n}\xi_\mathrm{n}}{m_\mathrm{s}\xi_\mathrm{s}},\qquad s=-\frac{\beta_\mathrm{n}}{|\alpha_\mathrm{n}|},\qquad \xi_\mathrm{n}=\sqrt{\frac{m_\mathrm{s}}{m_\mathrm{n}}\frac{1}{|\alpha_\mathrm{n}|}}\xi_\mathrm{s}. \tag{4.2.14}$$

In this work, we have included the nonlinearity parameter inside the junction $\beta=\beta_\mathrm{n}$ in the normalisation for generality and taken $\beta_\mathrm{n}=1$ which implies from Eq. (4.2.14) that $s<0$, in contrast to the numerical solutions studied by [50]. We note that in the linearised limit ($s\to 0$) this zero-field critical current reduces to the limit found by [75]. Furthermore, in the limit $v^2\to -s$, then $f_{d/2}^2\to 1/2\,(1-\alpha_\mathrm{n})$ and for the specific case $f_{d/2}^2\to 0$ we find Eq. (4.2.13) reduces to the well-known form

$$J_\mathrm{DJ}=J_0\frac{\xi_\mathrm{n}}{\xi_\mathrm{s}}\exp\left(-\frac{d}{\xi_\mathrm{n}}\right), \tag{4.2.15}$$

first found by De Gennes for SNS junctions [27] to first order and by Jacobson [93] through a similar approach.

4.2.2 Narrow Junctions, $\lambda_\mathrm{s}\gg w_\mathrm{s}\gg\xi_\mathrm{s}$

For narrow junctions, vortices penetrate the junction even in low fields. Consideration of low field solutions to the Ginzburg–Landau equations of the form $\psi=|\psi|\,e^{i\theta}$ led Josephson to propose his relation:

$$J=J_\mathrm{DJ}\sin(\Delta\gamma), \tag{4.2.16}$$

where J is the average current density along a contour between two points across the junction, J_DJ is a constant and $\Delta\gamma$ is the difference in the gauge invariant phase between the points. The general solutions for the critical current density derived from the Ginzburg Landau equations have been compared to those generated using the Josephson relation in low magnetic fields [109]. The critical current density from Eq. (4.2.8) approximates the general solution well in the weak coupling limit $V_0 > 8$, but breaks down when $V_0 \to 0$ and $J_{\mathrm{DJ}} \to J_{\mathrm{D}}$ [109].

Low field solutions for the gauge invariant phase difference $\Delta\gamma(y)$ in junctions between weakly coupled thin films have been found by Clem [94]. Whilst the original formalism was developed for thin films, it remains applicable the narrow 2D systems considered here since in both cases, ψ is independent of z and the local magnetic field can be taken to be equal to the applied field as $w_{\mathrm{s}} < \lambda_{\mathrm{s}}$. In Clem's approach, the spatial variation of the local intragranular current density within the superconducting electrodes is first found for a system with no current density flowing across the junction. From this, the variation of the the (topological) phase within the film in the Meissner state can be calculated along the junction, and used to calculate the Josephson current across the junction using Eq. (4.2.16).

The low field solutions for the gauge invariant phase difference $\Delta\gamma(y)$ and average critical current density across a narrow junction [94] are given by

$$\Delta\gamma(y) = \Delta\gamma(0) + \frac{2\pi B_{\mathrm{app}} y d_{\mathrm{eff}}}{\phi_0} + \frac{16\pi B_{\mathrm{app}}}{\phi_0 w_{\mathrm{s}}} \sum_{n=0}^{\infty} \frac{(-1)^n}{k_n^3} \tanh\left(k_n l_{\mathrm{s}}/2\right) \sin\left(k_n y\right), \tag{4.2.17}$$

$$k_n = (2n+1)\,\pi/w_{\mathrm{s}}, \tag{4.2.18}$$

$$J_{\mathrm{c}} = \max_{\Delta\gamma(0)} \left\{ \frac{1}{w_{\mathrm{s}}} \left| \int_{w_{\mathrm{s}}/2}^{w_{\mathrm{s}}/2} \mathrm{d}y \left[J_{\mathrm{DJ}}(0) \sin\left(\Delta\gamma(y)\right)\right] \right| \right\}, \tag{4.2.19}$$

where $J_{\mathrm{DJ}}(0)$ is the current density in zero field. In this case, $\gamma(0) = \pm\pi/2$ when the current through the junction is maximised for all ratios of $l_{\mathrm{s}}/w_{\mathrm{s}}$ [94]. In order to improve agreement between our computation and Eq. (4.2.17), we have included a term for the effective junction thickness d_{eff}. In the limit of thin, weakly coupled junction systems considered by [94], we find good agreement when $d_{\mathrm{eff}} \approx 2\xi_{\mathrm{s}}$. This term accounts for the finite size of the junction and the reduction in the order parameter on a length scale of order ξ_{s} close to the junction. With the inclusion of an effective junction thickness, the effective length of the S regions in the direction of current flow l_s is now smaller than the periodic system length l, with $l_\mathrm{s} = l - d_\mathrm{eff}$. It is this effective length of the S region l_s that appears in the second term of Eq. (4.2.17), as current flow within the superconducting electrodes is independent of the effective junction thickness d_eff in the weakly coupled limit considered by [94]. The geometry of the system, including the effective junction thickness d_eff, is shown in Fig. 4.1.

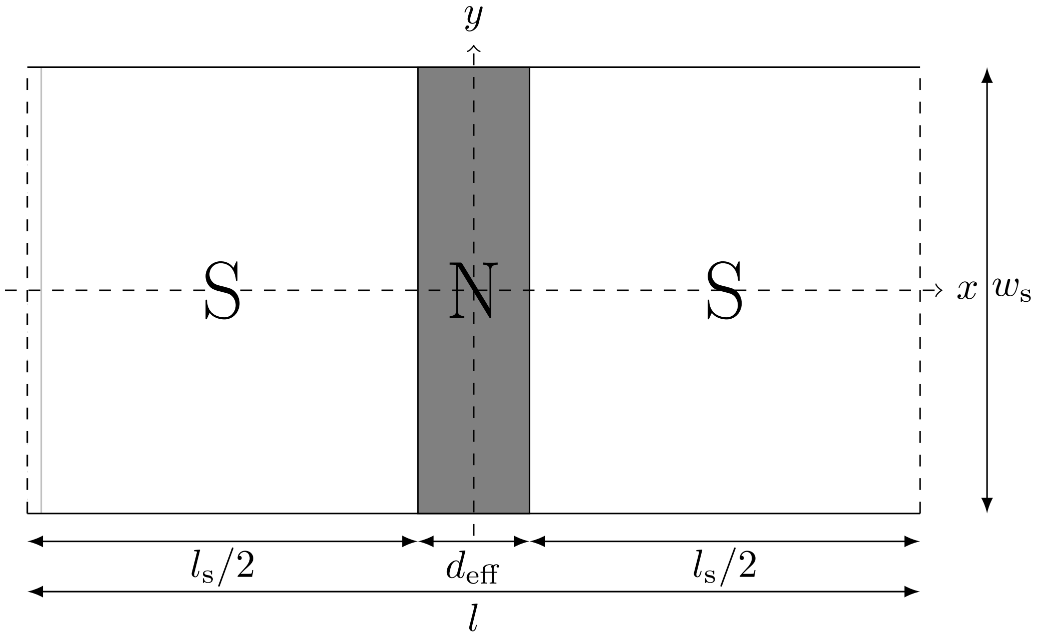

Figure 4.1: Schematic of the geometry used for junction systems considered in Eq. (4.2.17). System is periodic in the x direction with periodic length l, and insulating boundary conditions are applied at the boundaries in the y direction. With periodicity accounted for, the superconducting regions S each have length l_s and width w_s. Full field penetration in a normal region N of length d_eff is assumed in Eq. (4.2.17). We note that the effective junction thickness d_eff may differ from the thickness of the junction material d from Fig. 3.1 by an additive term of order of the coherence length, due to the proximity effect.

The 2D supercurrent density $\boldsymbol{J}_\mathrm{s}(x, y)$ within the superconducting electrodes in this limit is described succinctly by the curl of a stream function $\boldsymbol{S} = S\hat{z}$, that satisfies $\boldsymbol{J}(x, y) = \boldsymbol{\nabla} \times \boldsymbol{S}$. In the superconducting electrodes, where $(x \mod l) < l_\mathrm{s}$, a suitable stream function is given by [94]

$$S = \frac{B_{\text{app}} w_{\text{s}}^2}{2\mu_0 \lambda_{\text{s}}^2} \left\{ \frac{y^2}{w_{\text{s}}^2} + \frac{8}{w_{\text{s}}^3} \sum_{n=0}^{\infty} \frac{(-1)^n \cosh\left[k_n \left(\{x \bmod l\} - l_{\text{s}}/2\right)\right] \cos(k_n y)}{k_n^3 \cosh\left(k_n l_{\text{s}}/2\right)} \right\}. \tag{4.2.20}$$

Contours of the stream function Eq. (4.2.20), which coincide with streamlines of the current density, are illustrated in Fig. 4.2 for various aspect ratios $l_{\text{s}}/w_{\text{s}}$ of the junction.

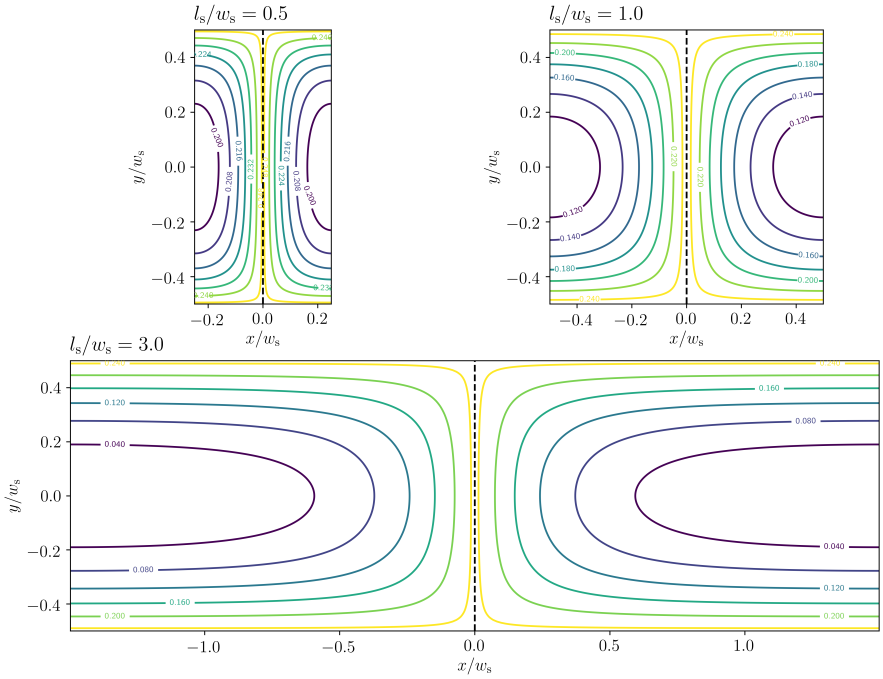

Figure 4.2: Contours of the stream function $2\mu_0\lambda^2 S/B_{\text{app}}w_{\text{s}}^2$ that coincide with current streamlines in rectangular thin film superconductors for various aspect ratios $l_{\text{s}}/w_{\text{s}}$ using Eq. (4.2.20). Location of junction region of thickness $d_{\text{eff}} \ll l_{\text{s}}, w_{\text{s}}$ represented by dashed line at $x = 0$ in all plots. For low aspect ratios $l_{\text{s}} \ll w_{\text{s}}$, current density flows parallel to the junction along most of the junction width, implying a linear variation of the topological phase along the junction width. For high aspect ratios $l_{\text{s}} \gg w_{\text{s}}$, current density streamlines are significantly curved close to the junction, implying the topological phase difference across the junction varies more slowly along the y direction at the junction edges, and vortices at the edges inside the junction are spaced further apart.

Equation (4.2.17) and Fig. 4.2 demonstrate that the screening currents close to the edges of the junction depend sensitively on the aspect ratio of the S regions, and ultimately determine the magnetic field dependence of J_c. For electrodes that are short relative to the junction width, when $l_\mathrm{s} \ll w_\mathrm{s}$, current flow close to the N region is mostly parallel to the junction across the whole length, Josephson vortices in the junction are spaced approximately equally along the junction width, and the critical current density has a Fraunhöfer-like functional form:

$$J_\mathrm{c} = J_\mathrm{DJ}(0)\frac{\phi_0}{\pi\phi_{l_\mathrm{s}\ll w_\mathrm{s}}}\left|\sin\left(\frac{\pi\phi_{l_\mathrm{s}\ll w_\mathrm{s}}}{\phi_0}\right)\right|, \qquad \phi_{l_\mathrm{s}\ll w_\mathrm{s}} = w_\mathrm{s} l_\mathrm{s} B_\mathrm{app}, \tag{4.2.21}$$

where $J_\mathrm{DJ}(0)$ is the current density in zero field. In contrast, for electrodes that are long relative to the junction width, with $l_\mathrm{s} \gg w_\mathrm{s}$, and $d_\mathrm{eff} \to 0$, screening currents flowing in the superconductors curve away from the junction across most of the junction width. As a result, Josephson vortices close to the edges are spaced further apart at the edges than at the centre, and larger current densities can be carried in the edge regions. In this case, the critical current density can be approximated as

$$J_\mathrm{c} = J_\mathrm{DJ}(0)\left|\mathcal{J}_0\left(\frac{\pi\phi_{l_\mathrm{s}\gg w_\mathrm{s}}}{\phi_0}\right)\right|, \qquad \phi_{l_\mathrm{s}\gg w_\mathrm{s}} = 14\zeta(3)B_\mathrm{app}w_\mathrm{s}^2/\pi^3, \tag{4.2.22}$$

where $\mathcal{J}_0$ is the Bessel function of the first kind of order 0, and $\zeta(3) = 1.202$. To identify the fraction of the width contributing to the *net* critical current, we note that the maxima of Eq. (4.2.19), $J_\mathrm{c}^\mathrm{peak}$, can be approximated when $w_\mathrm{s} \approx l_\mathrm{s}$ using:

$$J_\mathrm{c}^\mathrm{peak} \approx c_0\left(\frac{\phi_0}{B_\mathrm{app}w_\mathrm{s}^2}\right)^{c_1} J_\mathrm{DJ}(0). \tag{4.2.23}$$

In Fig. 4.3 we find empirically that over a large range of aspect ratios with $w_\mathrm{s} < l_\mathrm{s}$, the field dependence of $J_\mathrm{c}^\mathrm{peak}$ most closely follows the Bessel function field dependence; when $w_\mathrm{s} \approx l_\mathrm{s}$, $c_0 \approx 0.58$ and $c_1 \approx 0.58$ *. As noted by [95, 101], the reduction of the critical current with applied field when many vortices are present in the junction is slower when $w_\mathrm{s} \ll l_\mathrm{s}$ compared to when $l_\mathrm{s} \ll w_\mathrm{s}$, since the asymptotic behaviour of Eq. (4.2.22) has $J_\mathrm{c} \sim B_\mathrm{app}^{-1/2}$ compared to $J_\mathrm{c} \sim B_\mathrm{app}^{-1}$ from the Fraunhöfer-like relation of Eq. (4.2.21). A comparison between the critical

---

*We note that for $w_\mathrm{s} \approx l_\mathrm{s}$, the empirical parameters $c_0 \approx c_1$ approach values close to the Euler-Mascheroni constant $\gamma_\text{E-M} = \lim_{n\to\infty}\left[-\ln n + \sum_{k=0}^{n}\frac{1}{k}\right] \approx 0.577$; [110] although we do not offer proof of this and accept this may be mathematical coincidence.

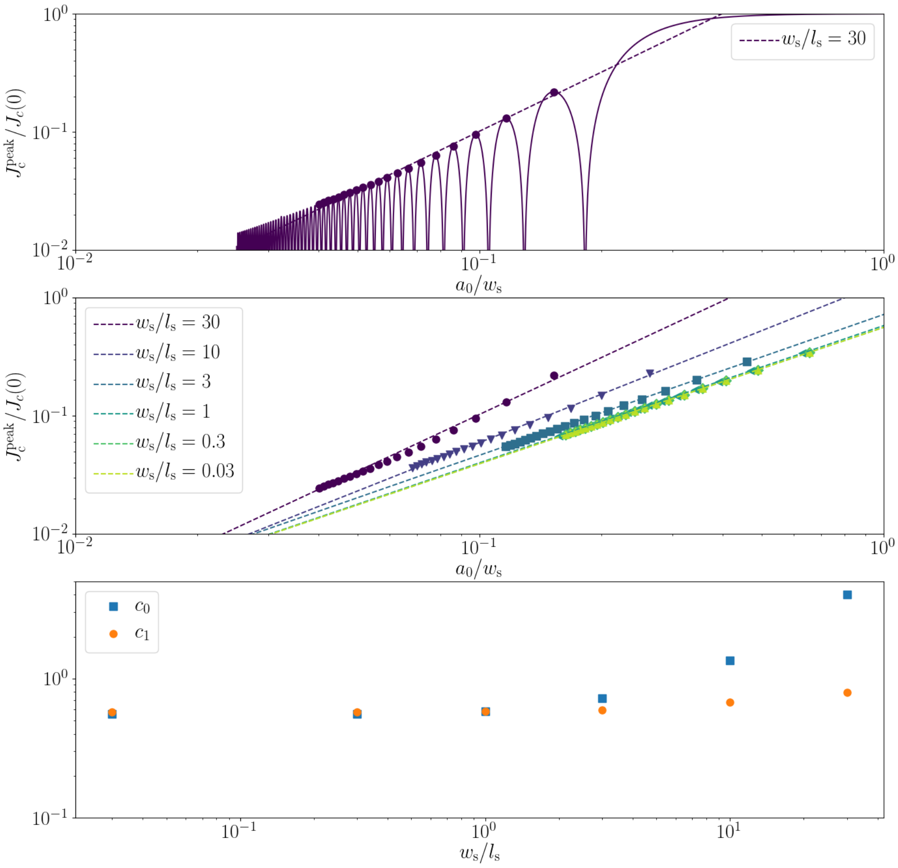

Figure 4.3: Top: Variation of the critical current density J_c as a function of the reduced vortex-vortex spacing parameter a_0/w_s using Eq. (4.2.19) with $w_\mathrm{s}/l_\mathrm{s} = 30$. Critical current density at local maxima $J_\mathrm{c}^\mathrm{peak}$ have been marked, and the dashed line represents the line of best fit over the first 20 maxima to Eq. (4.2.23), with c_0 and c_1 fit parameters. Middle: $J_\mathrm{c}^\mathrm{peak}$ values as a function of a_0/w_s for junctions of various aspect ratios $l_\mathrm{s}/w_\mathrm{s}$. Bottom: Variation of fit parameters c_0 and c_1 as a function of junction aspect ratio $l_\mathrm{s}/w_\mathrm{s}$.

current density determined from Eqs. (4.2.17) and (4.2.19) and the critical current density obtained from our 2D TDGL simulations is shown in Fig. 4.4 for a system with $w_\mathrm{s} \gg l_\mathrm{s}$ (upper panel) and $w_\mathrm{s} \ll l_\mathrm{s}$ (lower panel). In both cases, we take $d_\mathrm{eff} \approx 2\xi_\mathrm{s}$. The 2D TDGL simulations J_c from both TDGL-ZEP and TDGL-HIK show excellent agreement with each other and the analytic expressions derived from

Eqs. (4.2.17) and (4.2.19) in low fields. At these applied fields, no vortices exist in the S regions, and current flow is laminar within them. In the lower panel of Fig. 4.4, simulations of J_c obtained from TDGL-ZEP for larger system widths at $B = 0.2B_{\mathrm{c}2}$ still follow the prediction of Eqs. (4.2.17) and (4.2.19), but with larger scatter as a consequence of vortices in the S regions that distort the interference pattern of the computed system from the analytic prediction [101].

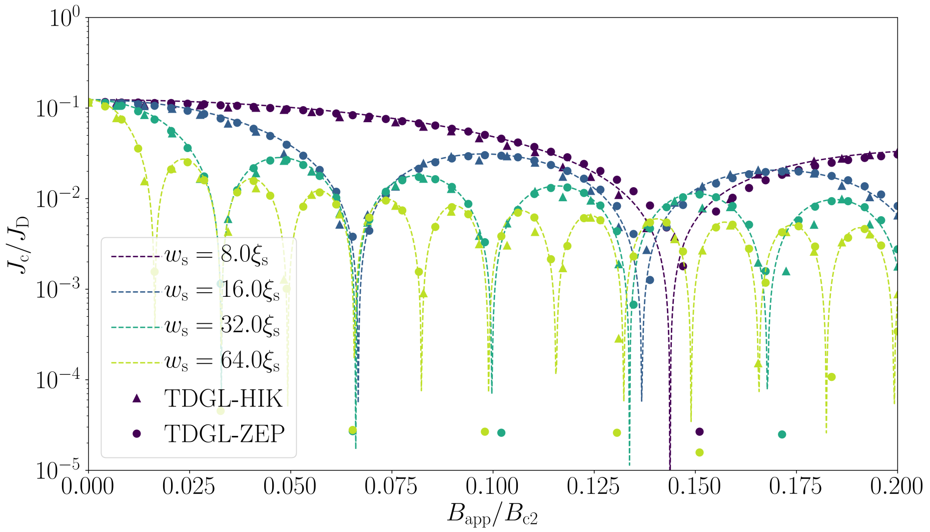

(a)

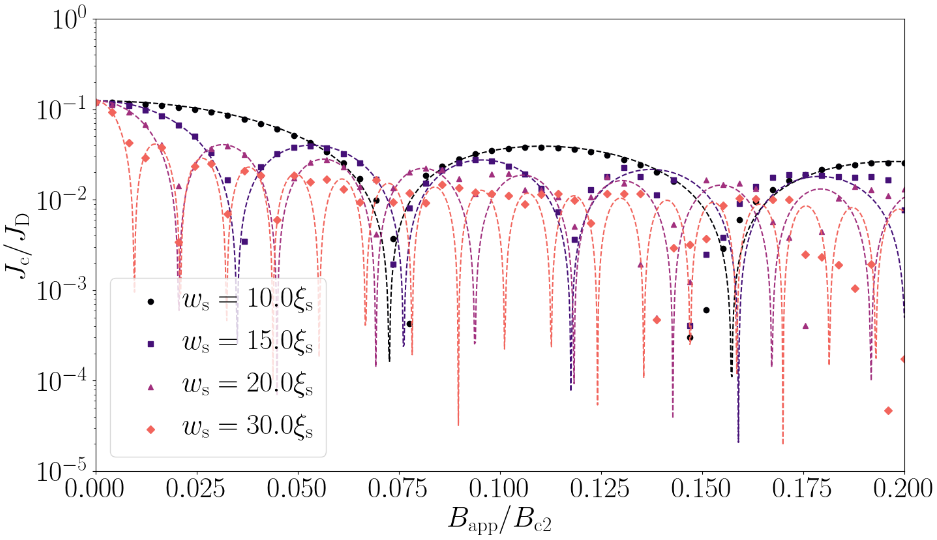

(b)

Figure 4.4: Simulations of $J_c(B)$ of narrow, very thin, weakly coupled junctions with different widths w_s. The system size in the x-direction $l = 6.0\ \xi_s$ (Upper) and $100.0\ \xi_s$ (Lower). The junction thickness d was taken to be $d_{min} = 0.5\ \xi_s$, $\alpha_n = -20.0$ and $\kappa = 40.0$. Top: $J_c(B)$ as calculated using the TDGL-ZEP code (circles) and TDGL-HIK code (triangles), with the hold time and time step for the TDGL-ZEP simulations set to $t_{hold} = 5 \times 10^3\tau$ and $\delta t = 0.5\tau$, and for the TDGL-HIK simulations set to $t_{hold} = 10\tau$ and $\delta t = 0.1\tau$ respectively. Bottom: $J_c(B)$ as calculated using the TDGL-ZEP code with hold time $t_{hold} = 10^3\tau$ and time step 0.1τ. Dashed lines in both panels are given by Eqs. (4.2.17) and (4.2.19) with $d_{eff} = 2\xi_s$.

4.2.3 Wide Junctions, $w_{\mathbf{s}} \gg \lambda_{\mathbf{s}}, \xi_{\mathbf{s}}$

For completeness, we shall briefly review wide junctions also. In wide junctions between weakly coupled superconductors in low fields, with widths that are comparable to or larger than the penetration depth λ_{s} but still smaller than the Josephson penetration depth λ_{J}, the screening currents that flow around the S regions screen most of the applied magnetic field and flow parallel to the junction across all but the edge regions within λ_{s} of the junction edges. On a junction length scale much greater than λ_{s} therefore, away from the junction edges, the gradient of the phase difference $\Delta\gamma$ along the junction is proportional to the applied field at the edges of the junction,

$$\frac{\partial \Delta\gamma}{\partial y} = \frac{2\pi d_{\mathrm{eff}}}{\phi_0} B = \frac{2}{\lambda_{\mathrm{J}}} \frac{B}{B_{\mathrm{cJ}}}, \qquad B_{\mathrm{cJ}} = \frac{\phi_0}{\pi d_{\mathrm{eff}} \lambda_{\mathrm{J}}} = \frac{2\xi_{\mathrm{s}}^2}{\lambda_{\mathrm{J}} d_{\mathrm{eff}}} B_{\mathrm{c2}}, \tag{4.2.24}$$

where B_{cJ} is a characteristic field for vortices in the junction. Equation (4.2.16) can be combined with Eq. (4.2.24) to give the well-known stationary Sine-Gordon equation given by

$$\frac{\partial^2 \varphi}{\partial y^2} = \frac{1}{\lambda_{\mathrm{J}}^2} \sin\varphi, \tag{4.2.25}$$

which fixes the Josephson penetration depth as the length scale for variations in the phase difference along the junction [111]

$$\lambda_{\mathrm{J}}^2 = \frac{\phi_0}{2\pi\mu_0 J_{\mathrm{DJ}} d_{\mathrm{eff}}}. \tag{4.2.26}$$

The effective junction thickness $d_{\mathrm{eff}} \approx d + 2\lambda_{\mathrm{s}} \tanh\left[\frac{(l-d)}{2\lambda_{\mathrm{s}}}\right]$ up to a term of order ξ_{s} when corrected to accommodate a finite electrode size of superconductor either side of the junction [111]. Equation (4.2.26) has solutions

$$k\frac{B(y)}{B_{\mathrm{cJ}}} = \mathrm{dn}\left(z_0 + \frac{y}{k\lambda_{\mathrm{J}}}, k\right), \tag{4.2.27}$$

where k, z_0 are constants of integration that must be found from the applied magnetic field at the edges of the junction and the condition that the current I flowing through the junction is maximised [98]. Specifically, these conditions take the form

$$2k\frac{B_{\mathrm{app}}}{B_{\mathrm{cJ}}} = \mathrm{dn}\left(z_0 + \frac{w_{\mathrm{eff}}}{2k\lambda_{\mathrm{J}}}, k\right) + \mathrm{dn}\left(z_0 - \frac{w_{\mathrm{eff}}}{2k\lambda_{\mathrm{J}}}, k\right), \tag{4.2.28}$$

$$k\frac{\mu_0 I}{B_{\mathrm{cJ}}} = \mathrm{dn}\left(z_0 + \frac{w_{\mathrm{eff}}}{2k\lambda_{\mathrm{J}}}, k\right) - \mathrm{dn}\left(z_0 - \frac{w_{\mathrm{eff}}}{2k\lambda_{\mathrm{J}}}, k\right), \tag{4.2.29}$$

where $w_{\mathrm{eff}} \approx w$, up to an additive constant of order $\xi_{\mathrm{s}} \ll \lambda_{\mathrm{s}}$. Equations (4.2.28) and (4.2.29) constrain k to a discrete set of values at a given applied field, ordered by the number of whole vortices in the junction; small values of k represent a rapidly oscillating magnetic field along the junction, and are associated with states containing large numbers of vortices per unit length along the junction. The critical current $I_{\mathrm{c}} = J_{\mathrm{c}} w_{\mathrm{eff}}$ of the junction is then found at each k by maximisation of $|I|$ as a function of z_0 [98]. In general, the field dependence of the critical current is multivalued and requires the solution of trancendental equations [112], with solution branches depending on the number of whole vortices in the junction. Physically, this arises because states with different numbers of vortices and different critical current density can be stable at the same applied field due to the presence of a surface barrier in the system, and, in general, these states have different critical currents.

The net critical current density of the junction is once again given by a Fraunhöfer pattern similar to Eq. (4.2.21) for wide junctions when many vortices are present in the junction [111]. In this case, the applied magnetic field is much larger than any screening currents flowing across the junction itself that reduce the local magnetic field at the centre of the junction, and $k \to 0$. Following [112], using the expansion $\mathrm{dn}\,(z,k) \approx 1 - \frac{k^2}{2}\sin^2 z + O(k^4)$ [110], Eqs. (4.2.28) and (4.2.29) simplify to

$$2k\frac{B_{\mathrm{app}}}{B_{\mathrm{cJ}}} = 2 - \frac{k^2}{2}\left[1 - \cos\left(\frac{w_{\mathrm{eff}}}{k\lambda_{\mathrm{J}}}\right)\cos\left(2z_0\right)\right], \tag{4.2.30}$$

$$k\frac{\mu_0 I}{B_{\mathrm{cJ}}} = -\frac{k^2}{2}\sin\left(\frac{w_{\mathrm{eff}}}{k\lambda_{\mathrm{J}}}\right)\sin\left(2z_0\right), \tag{4.2.31}$$

After some rearrangement, Eq. (4.2.31) takes the form

$$\frac{\mu_0^2 I^2}{B_{\mathrm{cJ}}^2} = \frac{k^2}{4}\sin^2\left(\frac{w_{\mathrm{eff}}}{k\lambda_{\mathrm{J}}}\right)\left\{1 - \left[\frac{k^2 + 4k\frac{B_{\mathrm{app}}}{B_{\mathrm{cJ}}} - 4}{k^2\cos\left(\frac{w_{\mathrm{eff}}}{k\lambda_{\mathrm{J}}}\right)}\right]^2\right\}. \tag{4.2.32}$$

Finding the junction critical current $I_\mathrm{c} = J_\mathrm{c} w_\mathrm{eff}$ is now an optimisation problem, with $I_\mathrm{c}(B_\mathrm{app}) = \sqrt{\max_k\{I^2(B_\mathrm{app}, k)\}}$. In the limit of interest, $k \to 0$ with $k\lambda_\mathrm{J}$ finite, the term in the curly braces in Eq. (4.2.32) is large and negative unless $k = B_\mathrm{cJ}/B_\mathrm{app}$. In this case, this term tends to unity and the well known Fraunhöfer dependence is recovered

$$\lim_{k\to 0} J_\mathrm{c} = J_\mathrm{DJ}\frac{2\xi^2 B_\mathrm{c2}}{w_\mathrm{eff} d_\mathrm{eff} B_\mathrm{app}}\left|\sin\left(\frac{w_\mathrm{eff} d_\mathrm{eff} B_\mathrm{app}}{2\xi^2 B_\mathrm{c2}}\right)\right| \qquad \text{where} \quad \frac{B_\mathrm{app}}{B_\mathrm{cJ}} = \frac{B_\mathrm{app}\lambda_\mathrm{J} d_\mathrm{eff}}{2B_\mathrm{c2}\xi^2} \gg 1. \tag{4.2.33}$$

Note that the condition for the Fraunhöfer relation to arise is a condition on the applied field, and is a valid limit of the Eq. (4.2.26) equation for a junction containing many vortices for all widths satisfying $w \gg \lambda$. The crossover from Eq. (4.2.21) to Eq. (4.2.33) has been investigated analytically by [97].

An example set of simulations using TDGL-ZEP in this limit is presented in Fig. 4.5 and compared to the analytic results of [112] derived from Eqs. (4.2.28) and (4.2.29) for junctions of varying widths with $\lambda_\mathrm{J} = 9.5\xi_\mathrm{s}$ and $\lambda_\mathrm{s} = 5.0\xi_\mathrm{s}$. It can be seen that the critical current density determined from simulations can be the J_c of a branch that is not the maximum J_c of all possible branches at a given field. The proportion of simulations that lie below the maximal envelope could be reduced by the hold time t_hold at a candidate J_c to allow the number of vortices in the junction to adjust to maximise J_c; here, $t_\mathrm{hold} = 5000\tau$. However, when the applied field is sufficiently large such that there are many vortices in the junction ($B_\mathrm{app} \gg B_\mathrm{cJ}$), the solutions tend towards the sinc-like pattern of Eq. (4.2.33) and the envelope of the critical current density decreases inversely proportionately to the applied field ($J_\mathrm{c} \sim B_\mathrm{app}^{-1}$) [112].

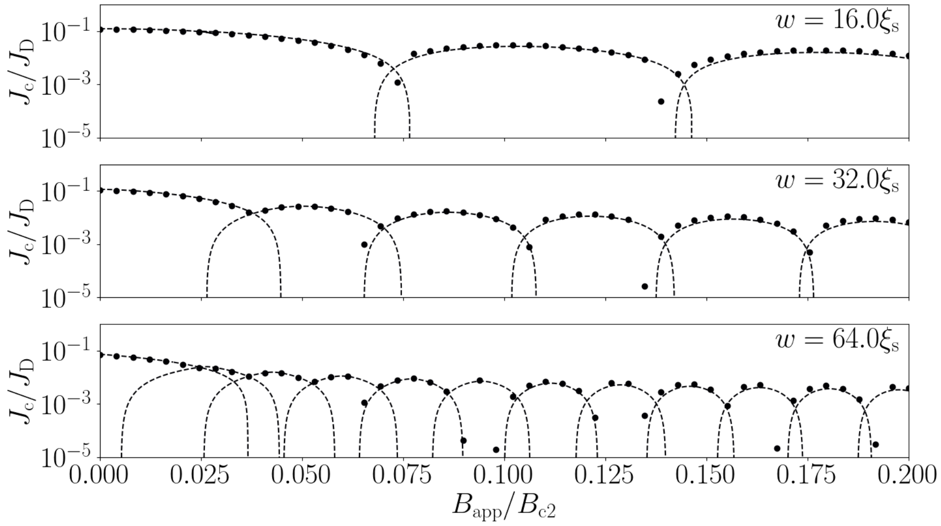

Figure 4.5: 2D simulations of the critical current of a wide, thin, weakly coupled Josephson junction (markers) as described in Section 4.2.2 using TDGL-ZEP. The periodic system size in the x-direction $l = 6.0\xi_s$, the superconductor width $w_s = 64.0\xi_s$ and the Ginzburg–Landau parameter and friction coefficient in the superconductor are $\kappa = 5.0$ and $\eta = 5.79$ respectively throughout. The junction is of thickness $d = h_x = 0.5\xi_s$ with $\alpha_n = -20$, and J_D is calculated using Eq. (4.2.8). Remaining computational parameters are as described in the text. Dashed lines are comparisons to the analytic expressions for the low field J_c using Eqs. (4.2.28) and (4.2.29) from [112], with $d_{eff} = 5.8\xi_s$ and $w_{eff} = w_s - \xi_s$.

4.3 Josephson Junctions in Arbitrary Magnetic Field

In this section, we derive new analytic expressions for the critical current density of very narrow Josephson junctions ($w_s < \xi_s$), that are valid across the entire range of applied magnetic fields, up to the upper critical field of the system. We shall then use these expressions to form approximations for the dependence of the critical current density on applied magnetic fields for very narrow ($w_s \ll \xi_s$) and narrow junction systems ($\xi_s \ll w_s \ll \lambda_s$). First we consider current flow within the junction from screening currents and from the injected currents. Integrating around a thin closed rectangular loop inside the system using Eq. (4.2.2) with the lower path along the x-axis and the upper path at y gives

$$\oint \boldsymbol{\nabla}\gamma \cdot \mathrm{d}\boldsymbol{l} = \oint \boldsymbol{\nabla}\theta \cdot \mathrm{d}\boldsymbol{l} - \oint \boldsymbol{B} \cdot \mathrm{d}\boldsymbol{S}, \tag{4.3.1}$$

after applying Stoke's theorem on the magnetic vector potential term. For any choice of gauge, the first closed integral on the RHS in θ is $2\pi n$ where n is the number of vortex cores inside the closed contour, from the requirement that the order parameter magnitude be a single valued function. We assume that the order parameter magnitude is symmetric about both the y-axis and x-axis, that the screening currents and hence $\partial_y\gamma$ are both antisymmetric about these axes, and to first order the transport current is uniform along the y-axis, such that $\langle J_{s;x}\rangle_y = m_x^{-1}(x)\, f^2 \partial_x\gamma(y=0)$ from Eq. (4.2.2). Assuming no vortices exist in the very narrow system ($n = 0$), and taking the sections of the contour in Eq. (4.3.1) that are parallel to the x axis to be sufficiently short relative to the coherence length ξ leads to the gauge invariant result

$$\partial_x\gamma(y) - \frac{\langle J_{s;x}\rangle_y}{f^2 m_x^{-1}(x)} = \frac{B_{\mathrm{app}}y}{B_{\mathrm{c2}}\xi_{\mathrm{s}}}. \tag{4.3.2}$$

We also assume that for very narrow junctions, given the boundary conditions at the insulating surfaces and the requirement for current continuity across the S-N internal interface, $J_{s;y}(x)$ can be taken to be zero. Equation (4.3.2) describes the transport current density and the screening currents that flow within the junction itself. We have not included the small self field corrections to the net field, that describe the currents associated with a vortex-antivortex pair at the edges, since we assume the self-field is much smaller than the applied field.

4.3.1 Very Narrow Junctions in High Fields

We can now extend the low field results for very narrow junction to fields up to the critical magnetic field of the junction. Substituting in our new expression for $\partial_x\gamma(y)$ into Eq. (4.2.1)and averaging over the y-direction as before gives

$$\partial_x\left(m_x^{-1}(x)\,\partial_x f\right) + \left[\alpha(x) - m_x^{-1}q^2 - \beta(x)f^2 - \frac{\langle J_{s;x}\rangle_y^2}{f^4\, m_x^{-1}(x)}\right] f = 0, \tag{4.3.3}$$

with $q^2 = \left(\frac{B_{\mathrm{app}} w_{\mathrm{s}}}{\sqrt{12} B_{\mathrm{c2}} \xi_{\mathrm{s}}}\right)^2$. Equation (4.3.3) represents a generalisation of Eq. (4.2.3) valid for very narrow junctions in all applied fields B_{app}. We can now solve for the critical current of the junction system using Eq. (4.3.3) in the two cases considered in Section 4.2.1: when the N region is thin, when $d \ll \xi_{\mathrm{s}}$; and when the N region is thick, when $d \gg \xi_{\mathrm{s}}$. For all these very narrow junctions, we assume there are no vortices in the barrier.

4.3.1.1 Thin Junctions in High Fields

Consider first the thin junction limit, where $d \ll \xi_{\mathrm{s}}$. Assuming $\beta(x)$ and $m_x^{-1}(x)$ are constant across the system for simplicity, we rescale Eq. (4.3.3) by $\tilde{x} = x\sqrt{1-q^2}$, $\tilde{f} = f/\sqrt{1-q^2}$ and $\tilde{j}_x = \langle J_{s;x} \rangle_y (1-q^2)^{-3/2}$ to give

$$\partial_{\tilde{x}}^2 \tilde{f} + \left[1 - \frac{1-\alpha(x)}{1-q^2} - \tilde{f}^2 - \frac{\tilde{j}_x^2}{\tilde{f}^4}\right] \tilde{f} = 0. \tag{4.3.4}$$

Since $\tilde{f}$ and $\tilde{j}_x$ are continuous across the S/N interface, we find a constraint between $\partial_{\tilde{x}} \tilde{f}$ and $\tilde{f}$ at the interface in the limit where $d \ll \xi_{\mathrm{s}}$, by integrating Eq. (4.3.4) across the normal region, where $|\tilde{x}| < d\sqrt{1-q^2}/2$, and assuming $\tilde{f}$ is symmetric across the junction:

$$2\tilde{f}'_{d/2} = d\frac{1-\alpha_{\mathrm{n}}}{\sqrt{1-q^2}} \tilde{f}_{d/2}, \tag{4.3.5}$$

where $\tilde{f}_{d/2} = \tilde{f}\,(x = d/2)$ and $\tilde{f}'_{d/2} = \partial_{\tilde{x}} \tilde{f}\,(x = d/2)$. The remainder of the derivation now follows the same approach as in Section 4.2.1 for low fields [108]; by substituting Eq. (4.3.5) into Eq. (4.3.4) and neglecting the highest order terms in the new small parameter $V_0^{-1} = \sqrt{1-q^2}/d\,(1-\alpha_{\mathrm{n}})$, we find the necessary condition for a solution to exist as $\tilde{j}_x < 1/2V_0$. In usual units, this corresponds to the critical current density J_{DJ},

$$\lim_{d \ll \xi_{\mathrm{s}}} \{J_{\mathrm{DJ}}(B_{\mathrm{app}})\} = J_0 \frac{\xi_{\mathrm{s}}}{2d\,(1-\alpha_{\mathrm{n}})} \left(1-q^2\right)^2, \tag{4.3.6}$$

where $q^2 = \left(B_{\mathrm{app}} w_{\mathrm{s}}/\sqrt{12} B_{\mathrm{c2}} \xi_{\mathrm{s}}\right)^2$ and $J_0 = B_{\mathrm{c2}}/\kappa^2 \mu_0 \xi_{\mathrm{s}}$ as before. The applied field at which the critical current density of the system is zero is given by $q^2 = 1$. This is equivalent to an applied field equal to the parallel critical field

$$B_{\mathrm{app}}\left(q^2 = 1\right) = \frac{\sqrt{12}\xi_{\mathrm{s}}}{w_{\mathrm{s}}} B_{\mathrm{c2}}. \tag{4.3.7}$$

This expression has previously been found by Tinkham to be the upper critical field of a thin film superconductor of thickness w_{s} when the applied magnetic field is parallel to the film surface, provided the film is thinner than approximately 1.8 ξ_{s} [88]. Equation (4.3.6) is compared to simulation data from TDGL-ZEP in Fig. 4.6, showing excellent agreement across the whole field range.

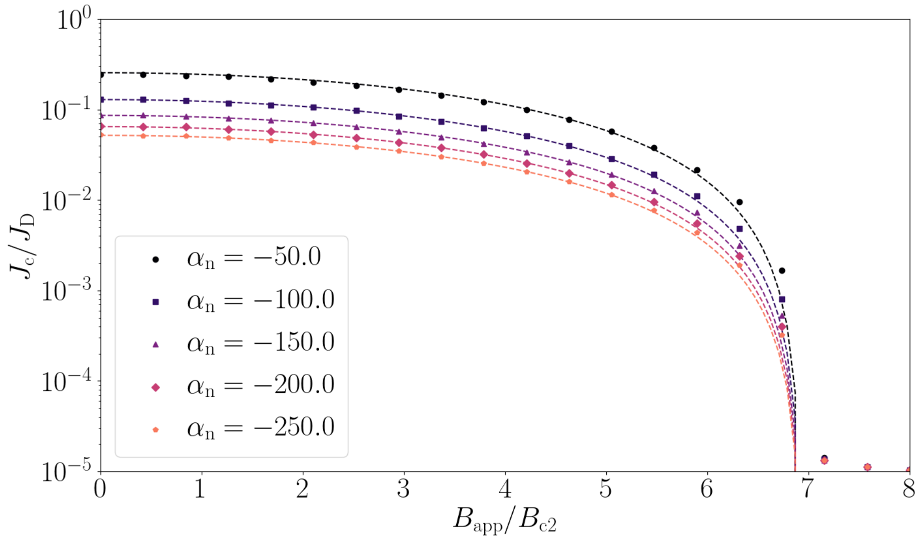

Figure 4.6: Simulations of $J_{\mathrm{c}}(B)$ of very narrow, thin, weakly coupled junctions as a function of α_{n} where $-250 \leq \alpha_{\mathrm{n}} \leq -50$. The width $w_{\mathrm{s}} = 0.5\xi_{\mathrm{s}}$ and the junction thickness $d = d_{\mathrm{min}} = 0.1\xi_{\mathrm{s}}$. The periodic system length in the x direction $l = 12.0\xi_{\mathrm{s}}$ and $\kappa = 5$. The effective mass in the normal region was taken to be $m_{\mathrm{n}} = m_{\mathrm{s}}$. The grid spacing was chosen to be $h_x = h_y = 0.1\xi_{\mathrm{s}}$, the time step $\delta t = 0.5\tau$, and the hold time $t_{\mathrm{hold}} = 5 \times 10^3\tau$. Dashed lines are given by Eq. (4.2.8).

We note that the junctionless case, where $V_0 = 0$ can trivially be considered also, as the rescaling used in Eq. (4.3.4) is equivalent to rescaling the Ginzburg–Landau equations in terms of a field dependent coherence length in the superconductor $\tilde{\xi}_{\mathrm{s}} = \xi_{\mathrm{s}}/\sqrt{1-q^2}$. In this case, the critical current of the thin film system becomes $J_{\mathrm{D}}\left(1-q^2\right)^{3/2}$ as found by previous authors [88].

4.3.1.2 Thick Junctions in High Field $d \gg \xi_\mathrm{s}$

For thick junctions, we rescale Eq. (4.3.3) into a similar form to that studied in [50] as in Section 4.2.1. In the superconducting regions, we rescale by $\tilde{x} = x\sqrt{1-q^2}$, $\tilde{f}_\mathrm{s} = f/\sqrt{1-q^2}$ and $\tilde{j}_x = \langle J_{s;x}\rangle_y (1-q^2)^{-3/2}$ to give a form equivalent to Eq. (4.2.9),

$$\partial^2_{\tilde{x}}\tilde{f}_\mathrm{s} + \left[1 - \tilde{f}_\mathrm{s}^2 - \frac{\tilde{j}_x^2}{\tilde{f}_\mathrm{s}^4}\right]\tilde{f}_\mathrm{s} = 0. \tag{4.3.8}$$

Inside the normal region, we rescale Eq. (4.3.3) by $\tilde{u} = x\sqrt{\frac{m_\mathrm{n}}{m_\mathrm{s}}\left(-\alpha_\mathrm{n} + \frac{m_\mathrm{s}}{m_\mathrm{n}}q^2\right)}$, $\tilde{f}_\mathrm{n} = -f\sqrt{\beta_\mathrm{n}/\left(\alpha_\mathrm{n} - \frac{m_\mathrm{s}}{m_\mathrm{n}}q^2\right)}$ and $\tilde{j}_u = \langle J_{s;x}\rangle_y \beta_\mathrm{n}\sqrt{m_\mathrm{n}/m_\mathrm{s}}(-\alpha_\mathrm{n} + \frac{m_\mathrm{s}}{m_\mathrm{n}}q^2)^{-3/2}$ to give a form similar to Eq. (4.2.10),

$$-\partial^2_{\tilde{u}}\tilde{f}_\mathrm{n} + \left[1 - \tilde{f}_\mathrm{n}^2 + \frac{\tilde{j}_u^2}{\tilde{f}_\mathrm{n}^4}\right]\tilde{f}_\mathrm{n} = 0. \tag{4.3.9}$$

The critical current in field can now be obtained following the procedure used by [50] for zero field, as in Section 4.2.1, but for our new, field-dependent rescaled variables. In usual units, the critical current of this narrow junction system in applied fields is given by:

$$\lim_{d \gg \xi_\mathrm{s} > w_\mathrm{s}} \{J_\mathrm{DJ}(B_\mathrm{app})\} = 4J_0(1-q^2)^{\frac{3}{2}}\frac{1-\sqrt{1-\tilde{s}\tilde{f}_{d/2}^2}}{\tilde{s}\tilde{v}}\exp\left(-\frac{d}{\tilde{\xi}_\mathrm{n}}\right), \tag{4.3.10}$$

where

$$\begin{aligned} \tilde{f}_{d/2}^2 &= \frac{\tilde{v}^2 + 1 - \sqrt{\tilde{v}^2(2-\tilde{s})+1}}{\tilde{v}^2+\tilde{s}}, \qquad \tilde{v} = \frac{m_\mathrm{n}\tilde{\xi}_\mathrm{n}}{m_\mathrm{s}\xi_\mathrm{s}}\sqrt{1-q^2}, \\ q^2 = \frac{B_\mathrm{app}^2 w_\mathrm{s}^2}{12}, \qquad \tilde{s} &= \frac{\beta_\mathrm{n}(1-q^2)}{(\alpha_\mathrm{n} - \frac{m_\mathrm{s}}{m_\mathrm{n}}q^2)}, \qquad \tilde{\xi}_\mathrm{n} = \sqrt{\frac{m_\mathrm{s}}{m_\mathrm{n}}\frac{1}{\left(-\alpha_\mathrm{n} + \frac{m_\mathrm{s}}{m_\mathrm{n}}q^2\right)}}\xi_\mathrm{s}, \end{aligned} \tag{4.3.11}$$

and $J_0 = B_\mathrm{c2}/\kappa^2\mu_0\xi_\mathrm{s}$ as in Table 2.1. Once again, we take $\beta_\mathrm{n} = 1$ and so when the effective mass of the N region is the same as that of the superconductors, $\tilde{v}^2 \to -\tilde{s}$, and $\tilde{f}_{d/2}^2 \to \left(1-q^2\right)/2\left(1-\alpha_\mathrm{n}\right)$. Equation (4.3.10) is compared to the critical current densities obtained from TDGL-ZEP in Fig. 4.7. Excellent agreement between Eq. (4.3.10) and TDGL-ZEP is observed across the entire field range, and across the parameter space for $d > \xi_\mathrm{s}$, $\alpha_\mathrm{n} < -1.0$, and $0.1\ m_\mathrm{s} < m_\mathrm{n} < 6.0\ m_\mathrm{s}$.

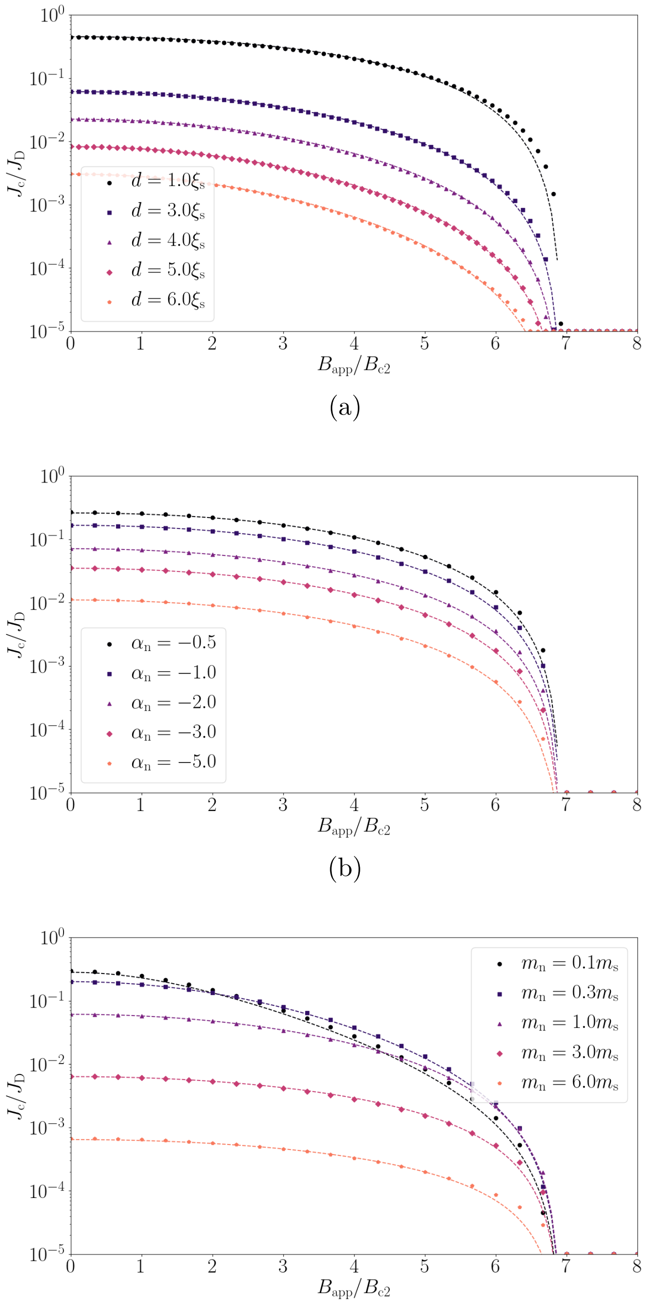

(a)

(b)

(c)

Figure 4.7: Simulations of $J_c(B)$ for very narrow, thick, weakly coupled junctions. The width $w_s = 0.5\xi_s$, the periodic system length in the x direction $l = 12.0\xi_s$ and $\kappa = 5$. The grid spacing was $h_x = h_y = 0.1\xi_s$, the time step $\delta t = 0.5\tau$, and the hold time $t_{hold} = 5 \times 10^3\tau$. (Upper) The effective mass in the normal region was taken to be $m_n = m_s$, $\alpha_n = -1.0$, and the junction thickness d was varied. (Middle) $m_n = m_s$, α_n was varied and $d = 2.0\xi_s$. (Lower) m_n was varied, $\alpha_n = -1.0$ and $d = 2.0\xi_s$. Dashed lines in all panels are given by Eq. (4.3.10).

In the limit where $\tilde{f}^2_{d/2} \to 0$, and when $m_\mathrm{n} = m_\mathrm{s}$ Eq. (4.3.10) reduces to the simpler form

$$\lim_{d \gg \xi_\mathrm{s} > w_\mathrm{s}} \left\{ J_\mathrm{DJ}(B_\mathrm{app}) \right\} = J_0 \frac{\left(1 - q^2\right)^2}{\sqrt{1 - \alpha_\mathrm{n}}} \exp\left(- \frac{d\sqrt{1 - \alpha_\mathrm{n}}}{\xi_\mathrm{s}} \right), \tag{4.3.12}$$

which provides the general field-dependent form for Eq. (4.2.15) famously found by De Gennes for SNS junctions in zero field [27]. In general, weakly coupled junctions with $\tilde{f}^2_{d/2} \to 0$ for any thickness of junction with $m_\mathrm{n} = m_\mathrm{s}$ can be described by the single expression

$$\lim_{\xi_\mathrm{s} > w_\mathrm{s}} \left\{ J_\mathrm{DJ}(B_\mathrm{app}) \right\} = J_0 \frac{\left(1 - q^2\right)^2}{2\sqrt{1 - \alpha_\mathrm{n}} \sinh\left(d\sqrt{1 - \alpha_\mathrm{n}}/\xi_\mathrm{s} \right)}, \tag{4.3.13}$$

where Eq. (4.3.6) is recovered in the limit $d\sqrt{1 - \alpha_\mathrm{n}}/\xi_\mathrm{s} \to 0$ and Eq. (4.3.12) is recovered in the limit $d\sqrt{1 - \alpha_\mathrm{n}}/\xi_\mathrm{s} \gg 1$.

4.3.1.3 Comments and Comparisons

The new solutions derived in this work for very narrow junctions, Eqs. (4.3.6) and (4.3.10), are formally restricted to systems with weakly coupled junctions with width of order of the coherence length, bounded by insulating surfaces. In this regime, an increase in magnetic field induces large screening currents in the superconductor close to the junction, which are restricted to flow parallel to the film surfaces due to the insulating boundary conditions and weaken superconductivity in the film. In effect, the applied magnetic field acts to increase the energy of the superconducting state, making it less stable, and increasing the local coherence length in the superconductor (and decreasing it in the normal metal). This reduces the magnitude of the order parameter far from the junction and increases the length scale over which the order parameter recovers from the boundary with the normal metal. At the parallel critical field, this length diverges, and superconductivity is destroyed throughout the system.

The full-field approximation for J_c given in Eq. (4.3.10) has the same leading order monotonically decreasing behaviour in low field as predicted by the authors of [107, 105, 106] using a model of an SNS Josephson junction from the linearised Usadel equations, including the applied magnetic field as an effective spin-flip scattering rate. Indeed, our result, Eq. (4.3.10) can be viewed as an extension to this result that describes fields approaching the parallel critical field of the superconductor.

Experimental measurements of SNS junctions between superconducting nanowires in this monotonically decaying regime that have been carried out in [113, 114] show good agreement with Eq. (4.3.10), as shown in Fig. 4.8 with reasonable estimates for the coherence length in the superconducting nanowires.

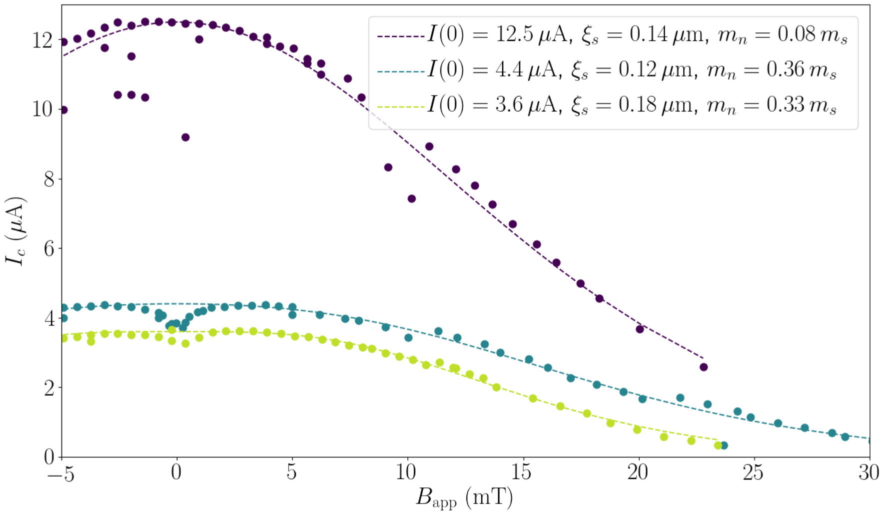

Figure 4.8: Comparison of Eq. (4.3.10) to experimental data on Al-Au-Al nanowire junctions measured by [114]. The junction thickness d varied between 900 and 1300 nm, and all junctions were $w_{\text{s}} = 125$ nm wide. The coherence length ξ_{n} in the Au region was taken to be 10 µm as suggested by weak localization experiments below 50 mK. The critical current at zero field $I(0)$ was fixed at the maximum measured current, and the coherence length of the Al superconductor ξ_{s} along with the ratio of the effective mass of a Cooper pair in Au and in Al $m_{\text{n}}/m_{\text{s}}$ were left as free parameters for the fit.

4.3.2 Narrow Junctions

We now extend our new solutions for $J_{\text{c}}(B_{\text{app}})$ in very narrow junctions to describe the qualitative behaviour of larger 2D systems with narrow junctions, with widths up to the length scale of the superconductor penetration depth λ_s, in arbitrary applied magnetic fields. In low fields, Eq. (4.2.23) accounts for the decrease in J_c from the decreasing spacing between vortices inside the junction region, but does not include the effect of vortices in the electrodes on the net critical current density or the reduction of the average Cooper pair density in the electrodes with field, and as such, cannot describe the decrease of the net critical current density of the junction to zero as the applied field approaches the effective upper critical field of the system. We therefore wish to consider the case where the vortex-vortex spacing a_0 inside the electrodes is smaller than the superconductor width w_s, but vortices do not move within the electrodes at J_c.

In low fields, Eq. (4.2.23) accounts for the fraction of the total width of the junction over which current density flows, as a result of screening currents in the superconductor set up by the distribution of vortices inside the junction. We therefore expect any approximation to J_c to reduce to this expression when the applied field is far below the critical magnetic field of the junction. However, in high fields, the order parameter inside the electrodes is no longer constant across the width of the system, but varies on the length scale of the vortex-vortex spacing a_0 in the electrodes. Similarly, the local current density also varies on a length scale of order a_0 in narrow junctions, instead of the junction width w_s, and Eq. (4.3.2) no longer holds. We are therefore motivated to replace the zero field J_DJ term in Eq. (4.2.23) with the field dependent J_DJ expressions from Eqs. (4.2.8) and (4.3.10) but with the width w_s replaced by a term comparable to the vortex spacing in the superconductor $\sim a_0$. This yields our approximation for J_c over the full field range as

$$J_\mathrm{c}(B_\mathrm{app}) = c_0 \left(\frac{\phi_0}{B_\mathrm{app} w_\mathrm{s}^2} \right)^{c_1} J_\mathrm{DJ} \left(B_\mathrm{app}, w_\mathrm{s} \to a_0 \right), \tag{4.3.14}$$

where $q^2 = B_\mathrm{app}/B_{c2}^*$ and J_DJ is taken from Eq. (4.3.6) and Eq. (4.3.10) in the thin limit and in the thick limit respectively. We have replaced B_c2 by B_c2^* to include junctions such as that considered above, where there is a insulating surface barrier along the edge of both the superconductor and the junction. Indeed, in the uniform case, representing current flow along a thin film between two insulators in which a junction is not present where $J_{\mathrm{c}} \approx J_{\mathrm{D}}\left(1-q^2\right)^{3/2}$, the substitution $q^2 = B_{\mathrm{app}}/B_{c2}^{*}$ reproduces the result $J_{\mathrm{c}} \approx J_{\mathrm{D}}\left(1-B_{\mathrm{app}}/B_{c2}^{*}\right)^{3/2}$ previously found by Abrikosov [115] close to the upper critical field of the system. Explicitly, in the weak coupling limit, Eq. (4.3.14) for thin junctions takes the form,

$$J_{\mathrm{c}}(B_{\mathrm{app}}) = J_0 \frac{c_0 \xi_{\mathrm{s}}}{2d\left(1-\alpha_{\mathrm{n}}\right)} \left(\frac{\phi_0}{B_{\mathrm{app}} w_{\mathrm{s}}^2}\right)^{c_1} \left(1-\frac{B_{\mathrm{app}}}{B_{\mathrm{c2}}^{*}}\right)^2, \tag{4.3.15}$$

whereas for thick junctions,

$$J_{\mathrm{c}}(B_{\mathrm{app}}) = J_0 \frac{c_0}{\sqrt{1-\alpha_{\mathrm{n}}}} \exp\left(-\frac{d\sqrt{1-\alpha_{\mathrm{n}}}}{\xi_{\mathrm{s}}}\right) \left(\frac{\phi_0}{B_{\mathrm{app}} w_{\mathrm{s}}^2}\right)^{c_1} \left(1-\frac{B_{\mathrm{app}}}{B_{\mathrm{c2}}^{*}}\right)^2. \tag{4.3.16}$$

2D simulations for two narrow junctions in high field are plotted in Fig. 4.9 and compared to Eq. (4.3.15) with $c_0 = c_1 = 0.58$ from Eq. (4.2.23) and B_{c2}^{*} set to $1.8B_{\mathrm{c2}}$. Excellent agreement is seen between the functional form and the simulated data, with only B_{c2}^{*} taken as a free parameter. We note that the power law dependence of Eq. (4.2.23) with $c_1 \approx 0.6$ has also been widely observed in many high temperature superconductors at high temperatures and magnetic fields that are still well below B_{c2}^{*} [116]; as shown in Fig. 4.3, the low field result with $c_0 \approx c_1 \approx 0.6$ is robust to a wide range of aspect ratios.

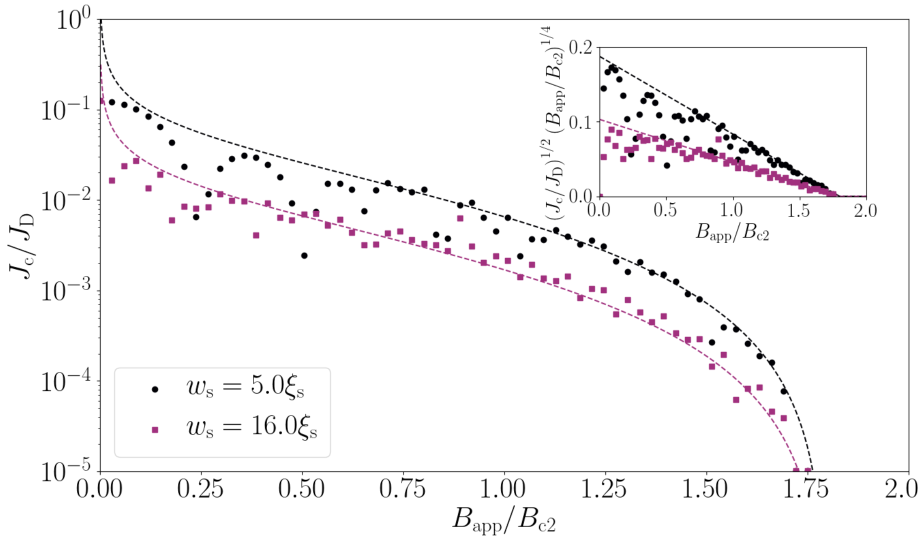

Figure 4.9: Simulations of the critical current of a narrow, thin junction in the weak coupling limit (markers) as described in Section 4.3.2 with the Ginzburg–Landau temperature parameter in the normal region $\alpha_n = -40.0$, a junction thickness $d = 0.25\xi_s$ smaller than the superconducting coherence length ξ_s, and a width w_s much smaller than the Josephson penetration depth λ_J but much larger than ξ_s. The periodic system size in the x-direction $l = 100.0\xi_s$, and the Ginzburg–Landau parameter and friction coefficient in the superconductor are $\kappa = 40.0$ and $\eta = 5.79$ respectively throughout. The grid spacing was chosen to be $h_x = h_y = 0.25\xi_s$ and the time step $\delta t = 0.5\tau$. Dashed lines represent Eq. (4.3.15) for the example parameters $B_{c2}^* = 1.8B_{c2}$, $c_0 = 0.58$ and $c_1 = 0.58$. Remaining computational parameters are as described in the text. Inset: Kramer plot of data shown in main plot.

4.4 Conclusions

In this chapter, we have obtained new expressions for the critical current density of narrow, tunnel-like SNS Josephson junctions on the scale of the superconducting coherence length across the entire magnetic field range, up to the effective upper critical field of the superconducting system. To the best of our knowledge, these expressions for J_c are the first for any Josephson junction system to be valid up to the effective upper critical magnetic field. We have confirmed these expressions against simulations based on time-dependent Ginzburg–Landau theory, and validated existing expressions from the literature for the critical current of

Josephson junctions in low applied magnetic fields. We have also found these expressions to be consistent with experimental data for nanowire junctions in which monotonically decreasing critical currents with field have been observed [113, 114]. By applying these new expressions for the critical current density of narrow junctions to the edge regions of Josephson junctions with dimensions much larger than the superconducting coherence length but smaller than the superconductor penetration depth, we obtain expressions for the critical current density as a function of field from a junction-based model that qualitatively agrees with experimental data for polycrystalline superconductors such as Nb_3Sn and existing models based on flux shear through grain boundaries [117]. In the next chapter, we compare these expressions to Ginzburg–Landau simulations of 2D and 3D polycrystalline superconducting systems.

Chapter 5

Simulations of the Critical Current of Polycrystalline Superconductors in Magnetic Fields

5.1 Introduction

In the last chapter, we studied current flow in 2D across an idealised model of a grain boundary, and found excellent agreement between critical current densities obtained from our TDGL simulations and analytic predictions derived for Josephson junction systems. However, in real technological superconductors, the morphology of the grain boundary network that spans the material is far more complex. In such polycrystalline materials, crystal grains are a range of sizes and shapes, and planes of grain boundaries lie at a range of angles with respect to the applied magnetic field. Grain boundaries can also intersect along lines and at points, introducing new pinning structures into 3D polycrystalline systems that have no equivalent in the idealised 2D Josephson junction models previously considered. Understanding the mechanism(s) limiting critical currents in these materials is therefore significantly more challenging, as understanding how the distribution of grain boundaries in a polycrystal contributes to vortex pinning and flow along the grain boundary network becomes extremely difficult to tackle using analytic tools alone. As mentioned in Chapter 2, this *summation problem* of how local flux pinning forces determine macroscopic critical currents is a long-standing problem in the literature [60, 61, 62].

Nevertheless, large-scale TDGL simulations provide a useful possible tool for the study of how changes in grain structure and the grain boundary network in polycrystalline materials affect the critical current density that the material can carry, and for visualising the manner in which vortices flow in such materials close to the critical current. The effect of varying parameters such as grain size, which can be difficult (or impossible) to systematically vary experimentally, can be investigated in much shorter time frames via simulation. As a result, we present TDGL simulations of vortex dynamics and critical currents in large-scale polycrystalline systems, and compare them to experimental results for critical currents in polycrystalline superconductors such as Nb_3Sn.

In this chapter, we first describe the computational method we used to generate representative grain morphologies for the simulation of polycrystalline materials. Then, we describe the preliminary simulations carried out on small 2D polycrystalline systems using TDGL-ZEP, and limitations that arose from the presence of surface barriers in the system. These results were previously published in [118]. Finally, we report results obtained for simulations on equiaxed polycrystalline systems in 3D, obtained using TDGL-HIK. In particular, when simulation parameters appropriate for Nb_3Sn are used, we find simulated critical current densities of similar magnitude and dependence with decreasing grain size and applied magnetic field as that observed experimentally in commercial polycrystalline Nb_3Sn samples. To our knowledge, these are the first large-scale TDGL simulations carried out for polycrystalline systems that display an increasing critical currents and flux pinning force with decreasing grain size, in agreement with the behaviour widely observed in experiment.

5.2 Grain Morphology Generation using Voronoi Tessellations

In order to simulate vortex flow in polycrystalline systems, it is necessary to first decide on a method to divide the superconducting region of our computational domain into a set of crystal grains, that we wish to be representative of the polycrystalline superconductor under study. That is, given a superconductor containing known distributions of grain sizes, sphericities, and anisotropies, we wish to be able to subdivide our computational domain into a set of grains that share the same size, sphericity, and anisotropy distributions. To address this problem, we adopt a method widely used in the mechanical modelling of mesoscale polycrystalline systems of using (weighted) Voronoi tessellations of the superconducting domain to generate a representative grain morphology [119].

The unweighted Voronoi tessellation of a $\mathcal{D}$-dimensional domain containing a set of n seed points is the set of n $\mathcal{D}$-dimensional convex polyhedra whose surfaces consist of the set of points equidistant from two (or more) seed points. Physically, these polyhedra can be viewed as the grains expected to form if all crystal grains nucleated at all seed points simultaneously and grew isotropically at equal rates [120]. The average grain size can be controlled by the number of seed points used to generate the tessellation. For a (uniform) random distribution of seed points within the domain, the Voronoi tessellation of the material generates polycrystals that possess distributions of the number of nearest neighbours between grains that are representative of those found in many isotropic polycrystalline systems to first order [120]. Unweighted Voronoi tessellations – including for periodic domains – can be generated using a number of open source computational tools. For the preliminary studies, unweighted 2D Voronoi tessellations generated from n randomly selected set of node points in the computational mesh were generated using the *pyvoro* Python wrapper [121] to the *Voro++* software library [122].

However, unweighted Voronoi tessellations generate grain morphologies that typically possess a smaller range of grain sizes and less spherical grains than those observed in equiaxed polycrystalline materials [123]. Weighted Voronoi tessellations – sometimes referred to as Laguerre tessellations – can be introduced to help address these shortcomings. A weighted Voronoi tessellation of the domain is defined similarly to the unweighted case, but with distances from seed points calculated using a non-Euclidean metric to apply weightings to the distances obtained, allowing further control over the grain size distribution. Use of an anisotropic metric will generate anisotropy in the resultant grain morphology. To control the distribution of the sphericity of grains in the material, the distribution of the initial set of seed points can be modified, either by choosing a different initial distribution of seed points, or by perturbation of the seed locations. To generate polycrystalline systems from representative grain size and sphericity distributions in this work, we use the *Neper* software package v3.5.0 [120, 123]. In this package, distributions of the grain size D – representing the effective diameter D of a spherical cell with an equivalent volume to the grain – and of the grain sphericity s – representing the ratio between the surface area of a spherical cell with equivalent volume to that of the grain and the grain surface area – are controllable. An iterative is method used to find a set of seed points and metric that generate a Laguerre tessellation with sufficiently similar grain size and sphericity distributions to those provided.

In this work, we restrict our attention to equiaxed polycrystalline systems, with particular attention to 3D systems representative of grain distributions in Nb_3Sn. Nevertheless, we emphasise that the general approach could be used to generate other grain morphologies of interest, such as to model vortex flow in systems with elongated grains such as NbTi, or even for systems containing spatial variations in grain sizes [123]. To create our model polycrystalline material for critical current and flux pinning simulations, we first generate a 3D tessellation of equiaxed grains, periodic in all three dimensions, with grain sizes corresponding to a typical lognormal grain size distribution for a grain growth system, using *Neper*. The probability density function $P(x)$ for the lognormal distribution of a random variable X with mean μ_X and variance σ_X^2 is given by

$$P(x) = \frac{1}{\sqrt{2\pi}x\sigma} \exp\left(-\frac{(\ln x - \mu)^2}{2\sigma^2}\right), \tag{5.2.1}$$

where the dimensionless parameters μ and σ^2 are

$$\sigma^2 = \ln\left(1 + \frac{\sigma_X^2}{\mu_X^2}\right), \qquad \mu = \ln(\mu_X) - \frac{\sigma^2}{2}. \tag{5.2.2}$$

For a typical grain-growth polycrystal, whose grain boundaries have migrated during formation from capillarity effects, the grain size distribution $D/\langle D\rangle$ has been observed to follow a lognormal distribution with average $\mu_X = \langle D\rangle = 1$ and standard deviation $\sigma = 0.35$, and $1 - s$ follows a lognormal distribution of average 0.145 and standard deviation 0.030 [123]. Indeed, there is evidence that polycrystalline Nb_3Sn in coatings exhibits grain size distributions that can be well-described by such a grain-growth model, with standard deviations of $D/\langle D\rangle$ of between 0.25 and 0.45 depending on growth conditions [124].

Finally, once we have generated a grain structure for the polycrystalline superconducting domain, we must decide on a mapping to the spatially dependent phenomenological parameters α, β and m of the TDGL theory. In this work, we are focussed on studying the role of vortex flow along grain boundaries in the polycrystalline system. Therefore, in analogy to the junction regions defined in the last chapter, we define grain boundary regions as those within a distance of $d/2$ of any face of crystal grains, and assign $\alpha = \alpha_{\mathrm{GB}}$. In this manner, a rasterised approximation to an equiaxed polycrystal is constructed, with grain boundaries given degraded superconducting properties with $\alpha_{\mathrm{GB}} < 1$.

5.3 Critical Current Simulations of 2D Polycrystals

We now present initial studies on small scale polycrystal systems carried out using TDGL-ZEP. We have previously published the work in this section in [118];

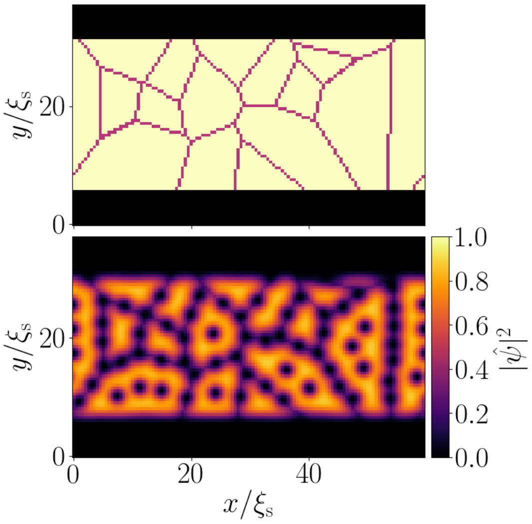

Figure 5.1: (Top) Voronoi mesh with 16 grains (top) and a grid step $h_x = h_y = 0.5\xi$ of a superconducting film with $w_\mathrm{s} = 25\xi$, $l = 60\xi$, $\eta = 5.79$ and $\kappa = 5$. The effective mass is constant throughout the system. Regions of reduced T_c where $\alpha = \alpha_\mathrm{GB}$ are denoted in red, and coating regions where $\alpha = -10.0$ are colored black. The edges of each Voronoi cell are 0.5ξ thick. (Bottom) Normalized superparticle density $|\psi|^2$ for this mesh at the critical current density J_c with $\alpha_\mathrm{GB} = -1.0$ in an applied magnetic field $B_\mathrm{app} = 0.35B_\mathrm{c2}$. The system is periodic in the x-direction and insulating boundary conditions were applied at the edges of the computational domain in the y-direction

we include the key results here to inform the discussion of 3D polycrystalline simulations that will follow. In this preliminary work, the subdivision of the domain into polycrystalline cells was carried out using the unweighted Voronoi tessellation method described in the last section, using *pyvoro* and *Voro++* [121, 122].

A representative polycrystal structure used for these initial small-scale studies, along with the corresponding order parameter distribution at J_c, is presented in Fig. 5.1. Both inter and intragrain fluxons are present, with a clear preference for fluxons to enter the structure along the grain boundaries and to occupy the grain boundary regions [125].

The evolution of the average electric field in the x-direction $\langle E_x \rangle$ and J_app with time is similar to those observed in the previous chapter for junction systems, as illustrated in Fig. 5.2. Determination of the critical current density of the

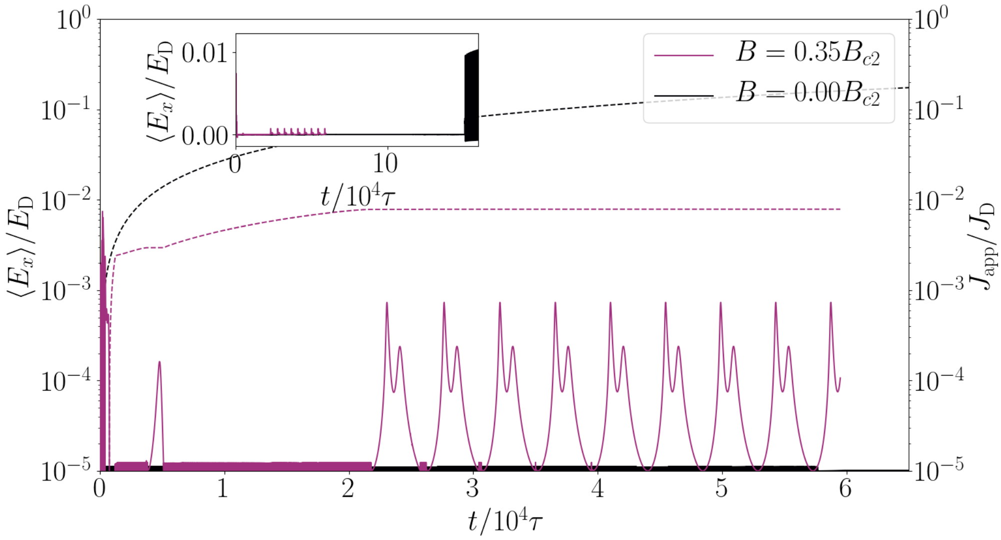

Figure 5.2: Spatially average (normalized) electric field in the x-direction $\langle E_x \rangle$ and applied current density J_app as a function of simulation time t, denoted by the solid and dashed lines respectively. J_app is increased at a rate of $5 \times 10^{-6} J_\mathrm{D} \tau^{-1}$. The system was initialised in the Meissner state throughout and evolved in timesteps of $h_t = 0.5\tau$. The order parameter and magnetic vector potential were converged to one part in 10^7 at each timestep. The critical current density J_c valued stored was taken to be the lowest current at which $\langle E_x \rangle > 10^{-5} E_\mathrm{D}$ for longer than $2 \times 10^4 \tau$; i.e. persistent vortex motion was observed. Inset: linear plot showing difference in magnitude of $\langle E_x \rangle$ at J_c at zero field and at 0.35 B_c2. Simulations at high magnetic fields take longer to equilibrate, and generate smaller electric fields.

polycrystal system was determined as described in the 'adaptive current ramp' method in Chapter 3, but with a linear increase in critical current density of $5 \times 10^{-6} J_\mathrm{D} \tau^{-1}$ at each current step and a hold time $t_\mathrm{hold} = 2 \times 10^4 \tau$.

As noted in the last section, the finite grid step size $h_x = h_y = 0.5\xi_\mathrm{s}$ used in these simulations results in rasterisation of the representation of the Voronoi tessellation and of the grain boundary regions. However Fig. 5.3 demonstrates that the critical current behaviour as a function of field is not strongly affected by this grid step size. As in TDGL-ZEP simulations in the last chapter, the standard grid step size of $0.5\xi_\mathrm{s}$ was chosen since it gave the optimal trade- off between accuracy and computation time.

The critical current density as a function of field $J_\mathrm{c}(B)$ for the 2D polycrystal

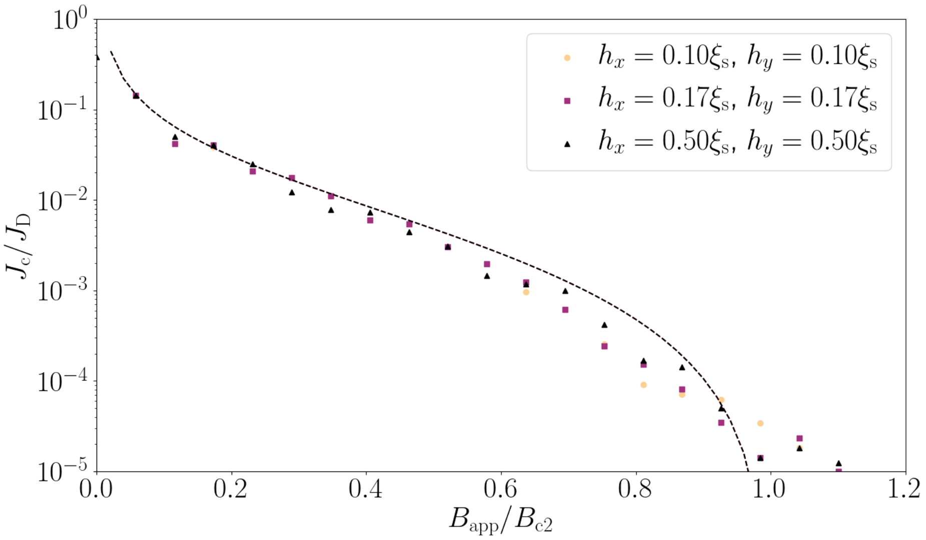

Figure 5.3: Critical current density J_c as a function of applied magnetic field B app for the Voronoi polycrystalline system shown in Fig. 5.1 for different mesh sizes. We have used $w_s = 25\xi$, $l = 60\xi$, $\eta = 5.79$ and $\kappa = 5$. The width of the boundary region in which T_c is reduced is unchanged. Mesh size does not strongly affect the form of $J_c(B)$ obtained. Dashed line represents predicted $J_c(B)$ from Eq. (5.3.2) with $\alpha_{Junc} = \alpha_{GB} = -1$

system of Fig. 5.1 is presented in Fig. 5.4, and can be compared to equivalent curves obtained for a system containing a single Josephson junction (similar to those considered in the previous chapter) in Fig. 5.5. When $\alpha_{GB} = 1.0$, there are no grain boundaries or barriers in the superconductor, and so J_c values represent those for a homogeneous thin film subject to a parallel magnetic field, and are identical in these two figures. J_c can be attributed to surface pinning from the two superconducting surfaces in contact with the coating region in this case, with a surface area per unit volume of surface pins $S = 2/w_s$, and a critical current density dependence given by [57]

$$J_c^{\alpha=1.0} = \frac{\xi_s}{2w_s} b^{-0.5}(1-b)^2 J_D \qquad (5.3.1)$$

where $b = B_{app}/B_{c2}$. In contrast, critical currents for systems with α_{GB} and $\alpha_{Junc} \leq -1.0$ in Figs. 5.4 and 5.5 are limited by current flow through grain boundary regions. We have used the semi-empirical low field critical current dependence for Josephson junction systems, with the factor $(1-b)^2$ added to extend the agreement

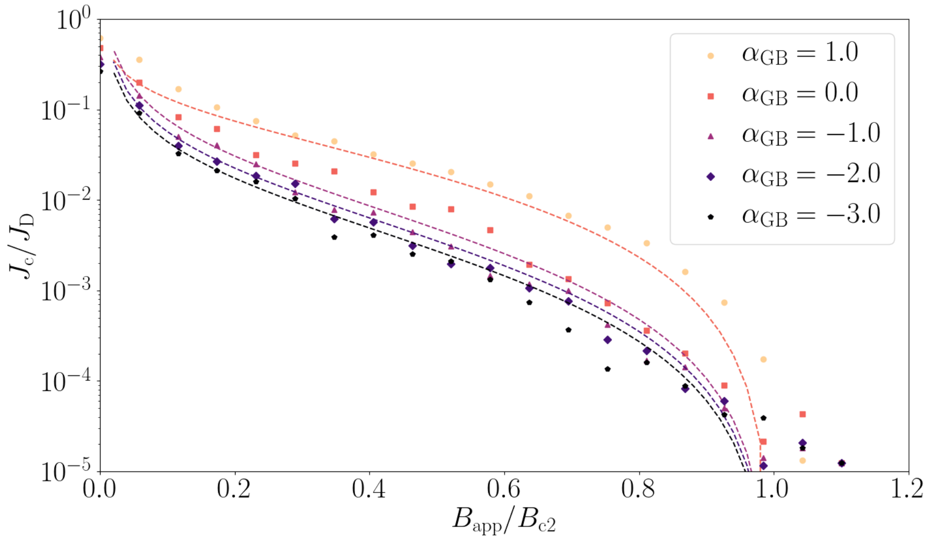

Figure 5.4: Critical current density J_c as a function of applied magnetic field B_{app} for the Voronoi polycrystalline system shown in Fig. 5.1 for different T_c (i.e. α_{GB}) values in the junction regions. We have used $h_x = h_y = 0.5\xi$, $w_s = 25\xi$, $l = 60\xi$, $\eta = 5.79$ and $\kappa = 5$. When the junction region is strongly normal, finite-size effects associated with flux quantisation become important and cusps become visible in the $J_c(B)$ characteristic. Dashed lines represented predicted $J_c(B)$ from Eq. (5.3.1) for $\alpha_{Junc} = \alpha_{GB} = 1$, and from Eq. (5.3.2) for $\alpha_{Junc} = \alpha_{GB} \le -1$

of the functional form to high-fields [75]:

$$J_c = \frac{J_{DJ}\xi_s^2}{\sqrt{2}w_s(d+2\xi_s)}b^{-1}(1-b)^2, \tag{5.3.2}$$

$$J_{DJ} = 2J_D u\left(u^2 - u\sqrt{u^2+2}+1\right)e^{-du/\xi_s} \tag{5.3.3}$$

where $u = \sqrt{\alpha_{Junc}}$. In Eqs. (5.3.2) and (5.3.3), we find $J_c \propto 1/w_s$ which indicates J_c is determined predominantly by surface pinning in these small-scale simulations.

We also note that J_c in all polycrystalline simulations is less than the corresponding single-junction case at all fields. Indeed, critical current densities are of similar orders of magnitude as those found in technological materials [55]. In Fig. 5.6, we present data that show J_c is independent of grain size at large grain sizes, suggesting that bulk pinning is negligible in these simulations, as the contribution from bulk pinning is expected to increase as grain size decreases. Only when the average grain diameter D is sufficiently small that the average Cooper pair density in the system is limited by the proximity effect of the grain boundary regions does

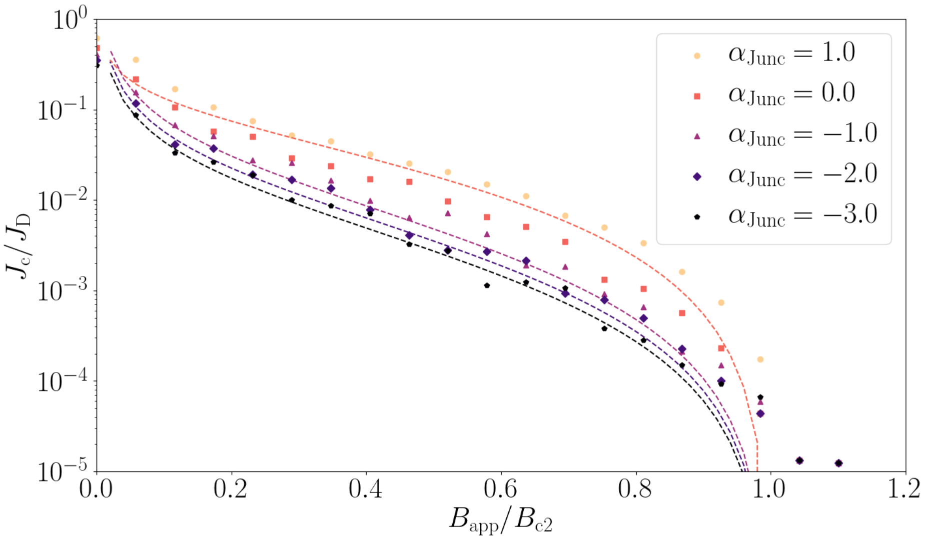

Figure 5.5: Critical current density J_c of a simple junction system as a function of applied magnetic field B_{app} for different T_c in the junction region. We have used $h_x = h_y = 0.5\xi$, $w_s = 25\xi$, $l = 60\xi$, $\eta = 5.79$ and $\kappa = 5$. $\alpha_{Junc} = 1.0$ corresponds to a homogenous superconductive sysetm, with no reduction of T_c in the grain boundary regions. Dashed lines represented predicted $J_c(B)$ from Eq. (5.3.1) for $\alpha_{Junc} = 1$, and from Eq. (5.3.2) for $\alpha_{Junc} \leq -1$

the critical current density become sensitive to changes in the system grain size. Furthermore, the independence of J_c when D is large for a range of different meshes is consistent with the conclusions from this work not being sensitive to variations in the specific locations of the initial seed points used to generate any particular large grain Voronoi mesh (e.g. Fig. 5.1).

In this section, we have seen that Voronoi tessellations can be used to generate polycrystal structures to investigate percolation of vortices through grain boundary networks in 2D superconducting systems, and that critical current densities obtained through such methods are similar in magnitude to those observed experimentally in optimised technological superconductors [55]. Results do not appear to depend strongly on mesh size nor details of the configuration of grains, provided a statistically significant number of grains is present in the computational domain. However, pinning by surfaces in the systems considered is generally much stronger than any bulk pinning contributions from the grain boundary network. As

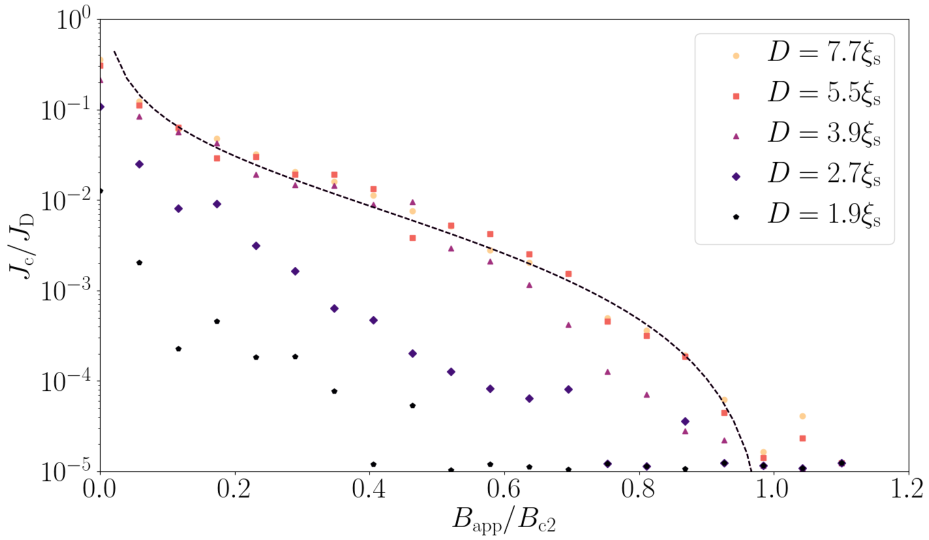

Figure 5.6: Critical current density J_c as a function of applied magnetic field B_{app} for the Voronoi polycrystalline system shown in Fig. 5.1 for different average grain diameters D. We have used $h_x = h_y = 0.5\xi$, $w_s = 25\xi$, $l = 60\xi$, $\eta = 5.79$ and $\kappa = 5$. In the large grain size regime, grain size does not have a significant effect on $J_c(B)$. For small grain sizes, J_c is reduced by the proximity effect. Dashed line represents predicted $J_c(B)$ from Eq. (5.3.2) for $\alpha_{Junc} = \alpha_{GB} = -1$

a result, the primary effect of grain boundaries in these small-scale simulations is to provide preferred channels for flux entry into and exit from the superconductor, and to reduce the surface barrier at all fields. Consequently, grain size does not appear to have a significant effect on the observed critical currents measured, except when sufficiently small ($D \sim \xi_s$) such that the superconducting volume fraction is small and the Cooper pair density in the system is significantly limited by the proximity effect. This lack of grain size dependence has been previously observed in similar simulations [75] but is in contrast to experimental data for large-grained polycrystalline superconductors with hundreds of grains across the width of the material such as Nb_3Sn, in which decreasing grain size increases critical current density [126]. In the next section, we shall investigate whether the use of large-scale solvers and periodic systems, without significant surface barriers, display this grain size dependence of critical current densities that has been widely observed in technological materials.

5.4 Critical Current Simulations of 3D Polycrystals

Following on from our preliminary 2D polycrystal simulations, we now consider vortex dynamics and critical currents in 3D polycrystalline systems, in which vortices may flow along the grain boundary network in the material. In particular, we show that the TDGL simulations describe the behaviour of the critical current density in equiaxed polycrystalline technological materials such as Nb_3Sn, subject to changes in grain size and grain boundary properties. Furthermore, we suggest how grain boundaries can be described using Josephson junction-like structures and how this description can help provide analytic expressions for critical current densities, using the mathematical results of the previous chapter.

Informed by our preliminary 2D polycrystal simulations, in order to have a sufficient number of grains in the system such that the resultant critical current behaviour is determined by the statistical properties of the grain distribution and not by any individual grain configuration, we require a large system size, and necessarily need to use the large-scale TDGL-HIK solver for these simulations. Furthermore, as indicated by our small scale 2D simulations, surface pinning effects can strongly mask the bulk flux pinning contributions from the grain boundary network, and so we restrict our attention to systems periodic in all three dimensions. We choose base parameters for our model polycrystalline system, presented in Table 5.1, to be representative of Nb_3Sn at $T = 4.2$ K, with a critical temperature of $T_{\mathrm{cs}} = 17.8$ K and a coherence length $\xi_{\mathrm{s}}(4.2\ \mathrm{K}) \approx 3.12$ nm [55]. The superconducting volume of our base system corresponds to physical dimensions of 468 nm × 468 nm × 468 nm with a mean grain size $D = 70\,\mathrm{nm}$. An example distribution of grain boundaries for this set of parameters, along with distributions of $|\psi|$ over the simulation domain and close to a representative grain are presented in Fig. 5.7. Indeed, vortices can be seen to preferentially occupy grain boundary regions, as observed in 2D, and bend to stay within them where possible.

The flux pinning force per unit volume $F_{\mathrm{p}} = J_{\mathrm{c}}B_{\mathrm{app}}$ as a function of reduced

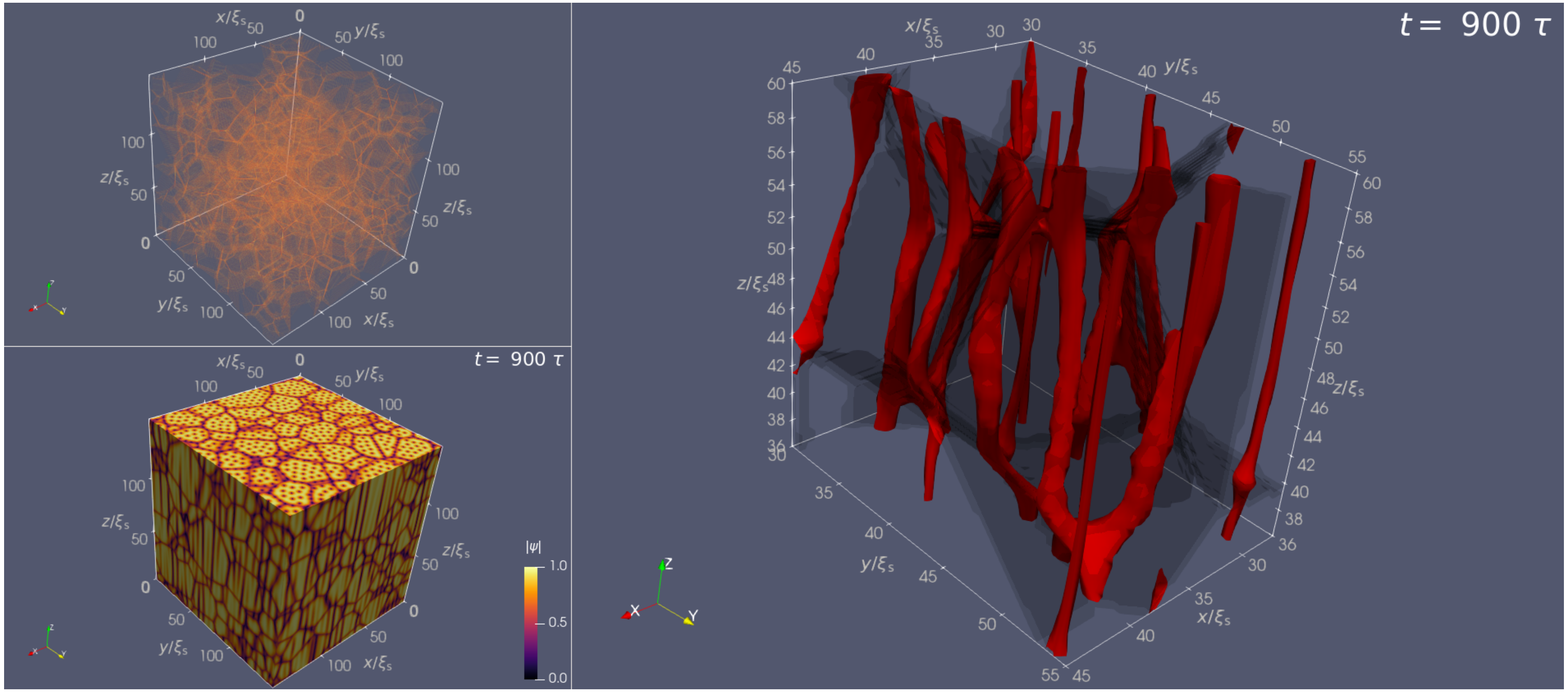

Figure 5.7: A snapshot of the time dependent simulation at $J_{\mathrm{app}} = 10^{-2} J_{\mathrm{D}}$ and $B_{\mathrm{app}} = 0.2 B_{\mathrm{c2}}$ for the base system described in Table 5.1. Top left: grain boundary network of the periodic physical system. Bottom left: distribution of the magnitude of the order parameter $|\psi|$ across the surfaces of the computational domain. Right: distribution of vortices around an example grain in the system. The surface of the region enclosing points where $|\psi| < 0.25$ is displayed in red, and the grain boundary regions are shown in black. A time-dependent visualisation at this applied field and current is available in the attached supplementary materials.

Parameter	Value
$h_{\{x,y,z\}}/\xi_{\rm s}(T)$	0.5
$L_x/\xi_{\rm s}(T)$	150.0
$L_y/\xi_{\rm s}(T)$	150.0
$L_z/\xi_{\rm s}(T)$	150.0
$D/\xi_{\rm s}(T)$	22.4
$d_{\rm GB}/\xi_{\rm s}(T)$	0.5
$\alpha_{\rm GB}$	-2.0

Table 5.1: Material parameters for the reference 3D polycrystalline system for 3D J_c investigations. $J_{\rm c}$ is decreased by 2.5% at each current step.

field, for TDGL-HIK simulations of polycrystalline materials with different grain boundary parameters $\alpha_{\rm GB}$, are shown in Fig. 5.8. The optimum flux pinning forces occur when the grain boundary thickness $d_{\rm GB}$ is close to the effective (normal metal) coherence length in the grain boundary $\xi_{\rm GB} = \sqrt{-\alpha_{\rm GB}}\,\xi_{\rm s}$ (defined when $\alpha_{\rm GB} < 0$). For more degraded boundaries, $J_{\rm c}$ decays approximately exponentially at a rate proportional to $d_{\rm GB}/\xi_{\rm GB}$ for $d_{\rm GB}/\xi_{\rm GB} > 1$, and for $\alpha_{\rm GB} < -4.0$ the maximum in the flux pinning force $F_{\rm p} \propto J_{\rm c}B_{\rm app}$ is found at higher reduced field values. For more weakly degraded grain boundaries ($\alpha_{\rm GB} > -4.0$), we find a Kramer dependence of the flux pinning force with applied magnetic field, such that the maximum flux pinning force per unit volume is close to 0.2 $B_{\rm c2}$. Both the magnitude of $J_{\rm c}$ with a grain size of 70 nm at $10^{-3}J_{\rm D}$, and the Kramer field dependence, are similar to those observed experimentally in optimised polycrystalline $\rm Nb_3Sn$ [55] suggesting these simulations capture the important physical processes in these systems. In the time dependent simulations when $J > J_{\rm c}$ (i.e. showing continuous vortex movement), we see significant differences in the curvature of moving vortices, above and below the optimum. In strongly degraded boundaries when $\alpha_{\rm GB} < -4.0$, vortices are significantly curved and follow grain boundaries, being preferentially held at points where two or more grain boundaries meet, whereas for $\alpha_{\rm GB} > -2.0$, vortices remain mostly straight, aligned along the applied field in the z axis.

Experimental and simulation flux pinning curves for different mean grain sizes are presented and compared in Fig. 5.10. The maximum flux pinning force per unit volume as a function of grain size is seen to be similar to the experimental values.

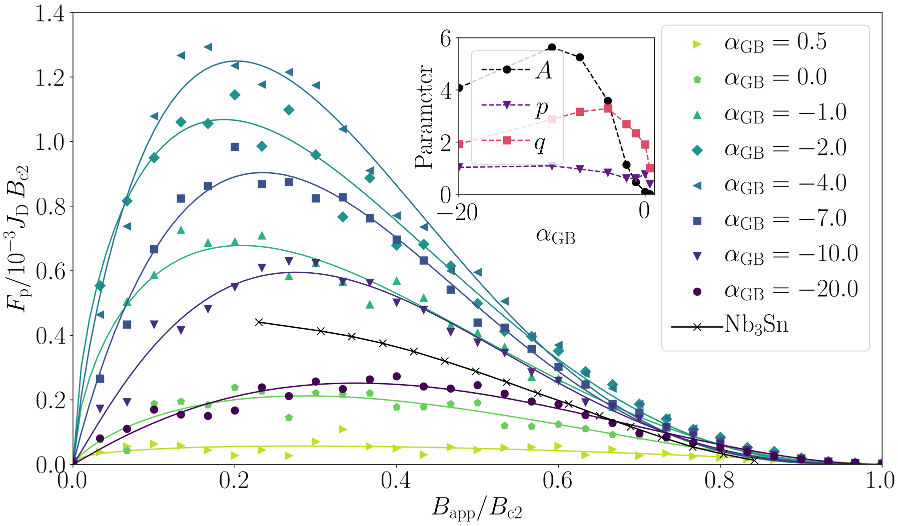

Figure 5.8: Normalised flux pinning force per unit volume $F_p/10^{-3}J_D B_{c2}$ for the polycrystalline 3D system described in Table 5.1 with varying α_{GB} at various applied magnetic fields. The maximum in the flux pinning force is found close to $B_{app} = 0.2B_{c2}$ for $\alpha_{GB} > -4.0$ but moves to higher fields as the grain boundaries become more strongly normal (as α_{GB} decreases). Solid lines are fits to Eq. (5.4.1) with $r = 1.1$. Crosses are typical experimental data for optimised bronze route Nb_3Sn, taken from [55]. Inset: Fitting parameters for Eq. (5.4.1) as a function of α_{GB}.

For very small grain sizes with $D < 100\,\text{nm}$, our simulations predict F_p^{max} values that are larger than observed in experiment, but this could be accounted for by a shorter coherence length in the superconducting grains ξ_s for these fine grained systems or degraded grain boundaries in such small grain material. We have also confirmed that in homogeneous systems with no flux pinning structures present, no significant critical current densities are found in these simulations. To our knowledge, these TDGL simulations of 3D polycrystalline systems are the first to display this increase of F_p^{max} with decreasing grain size D in qualitative agreement with experiment.

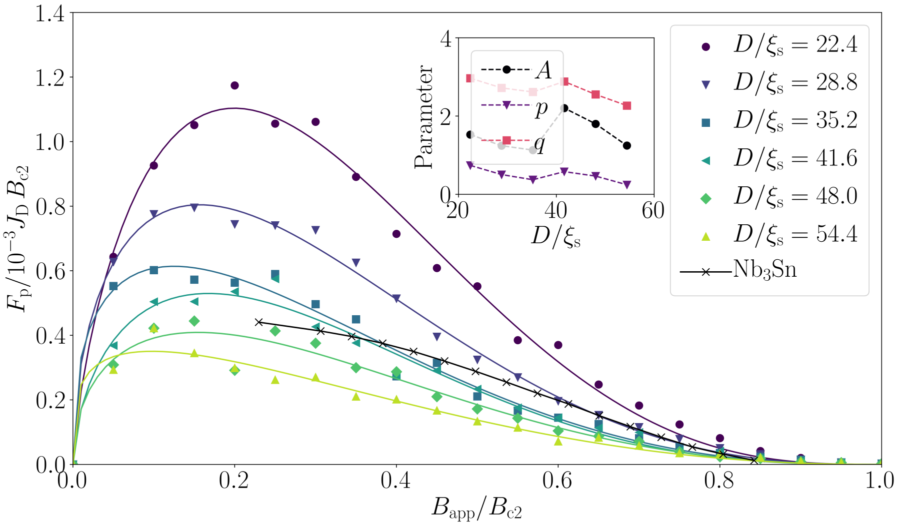

Figure 5.9: Normalised flux pinning force per unit volume $F_\mathrm{p}/10^{-3}J_\mathrm{D}B_\mathrm{c2}$ for a polycrystalline 3D system with varying mean grain size D. All other system parameters are set to the values given in Table 5.1. Solid lines are fits to Eq. (5.4.1) with $r = 1.1$. Crosses represent comparison to typical experimental data for bronze route $\mathrm{Nb_3Sn}$, taken from [55]. Inset: Critical current density J_c as a function of applied field for varying grain size; colours correspond to main plot.

5.4.1 Flux Pinning Expressions for Polycrystalline Materials

In 3D polycrystals, there are multiple types of pinning structures formed by the network of grain boundaries in the system; faces (grain boundaries) at the loci at which two grains meet, intersection lines along which two grain boundaries meet, and triple points at which three (or more) grain boundaries meet. The number of all of these structures in a given volume scales inversely proportional to the grain size D, albeit with different constants of proportionality. In principle, triple points can pin vortices more strongly than intersection lines, which will pin vortices stronger than grain boundary faces [99]. The intragrain magnetisation currents close to these structures will also be successively weaker: close to grain boundary faces, significant magnetisation currents can flow in the two orthogonal directions parallel to the face; close to line intersections, a significant magnetisation current can only flow in the direction parallel to the intersection line; and close to triple

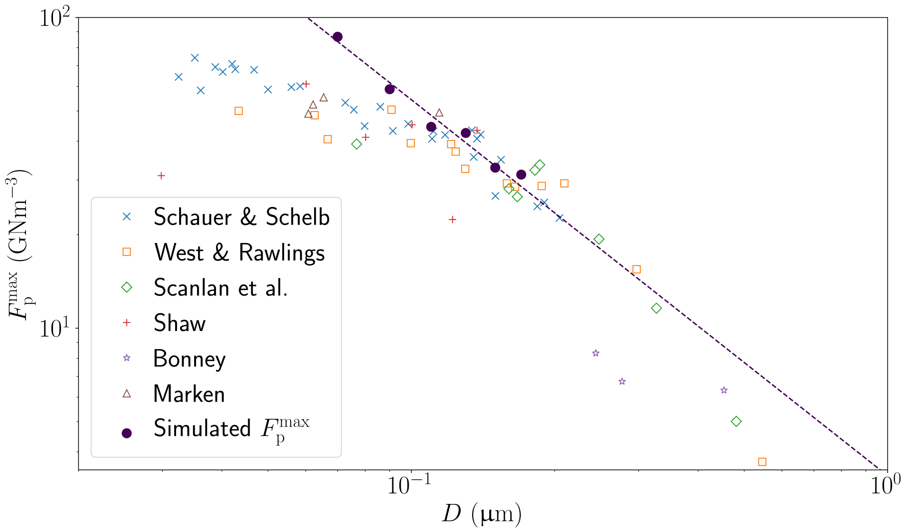

Figure 5.10: Maximum flux pinning force per unit volume $F_p^{\max}$ for the polycrystalline 3D system described in Table 5.1 with varying average grain diameter D compared to experimental data for the maximum flux pinning force measured in experimental Nb$_3$Sn samples taken from [126]. Dashed line represents fit to Eq. (5.4.1) with $p = 0.5$ and $q = 2$, with remaining free parameters found to be $A = 0.09$ and $r = 0.6$.

points, no significant magnetisation currents can flow, as currents are inhibited in three (non-collinear) directions.

How large these intragrain magnetisation currents are in the high-κ limit depends strongly on how degraded the grain boundary regions are, i.e. the value of α_{GB}. For very weakly degraded grain boundaries, with $\alpha_{\mathrm{GB}} \approx 1$, intragrain magnetisation currents along boundary surfaces are small, and vortices are only very weakly pinned to grain boundaries; this case corresponds to the current flow across grain boundary faces in the system limiting the critical (transport) current in the system, and therefore vortices depinning from grain boundary faces at the critical current. Such a case was referred to in [99] as weak intragranular pinning. As α_{GB} decreases, intragrain magnetisation currents are increased, and the contribution to the transport critical current from boundary intersection lines becomes largest; in this case, vortices remain mostly aligned to the axis of the applied magnetic field, but at the critical current, sections of them slide along grain boundaries preferentially. This case is the one considered within a flux pinning framework by [100]. In the extreme limit, when $\alpha_{\mathrm{GB}} \ll -1$, vortices curve to remain entirely within boundary regions, and the critical current is determined by the onset of vortex motion about triple points. Here Fig. 5.8 suggests $J_{\mathrm{c}} \sim (1-b)^2$, which can be obtained from Eq. (4.3.12) with $q^2 = B_{\mathrm{app}}/B_{\mathrm{c2}}$.

With such complexity, an analytic derivation of the average flux pinning force per unit volume arising from a grain boundary network is extremely difficult. As such, we adopt an empirical approach here to propose a suitable functional form to parameterise F_{p} for these polycrystalline systems. We note that some properties of the critical current expressions obtained in the previous chapter for weakly coupled Josephson junction systems in 2D (Eq. (4.3.14)), bear similarities to the observed behaviour of critical currents in polycrystalline technological superconductors. The Kramer-like field dependence implied by Eq. (4.3.15) has been widely observed in low temperature polycrystalline superconductors such as Nb$_3$Sn [127] up to B_{c2}, and the $w^{-1.2}$ factor in Eq. (4.3.14) is reminiscent of the inverse grain size dependence observed for J_{c} experimentally [117] and in our simulations (Fig. 5.10). Motivated by this, we propose an expression for the flux pinning force per unit volume for a polycrystalline system with weakly coupled grains (with highly degraded grain boundaries) based on Eq. (4.3.14) using

$$F_{\mathrm{p}}(B_{\mathrm{app}}) \approx J_0 B_{c2} A \left(\frac{\phi_0}{B_{c2}^{*} D^2} \right)^{r} (b^*)^p (1-b^*)^q f(\alpha_{\mathrm{GB}}), \tag{5.4.1}$$

where we have replaced w_{s} by the grain size D; defined the pinning parameters $p \approx 1 - c_1$ and $q \approx 2$; introduced the new empirical parameters A and r; and made the weak coupling approximations that $f(\alpha_{\mathrm{GB}}) = \xi_{\mathrm{s}}/2d\,(1-\alpha_{\mathrm{n}})$ in the thin limit and $f(\alpha_{\mathrm{GB}}) = \exp\left(-d\sqrt{1-\alpha_{\mathrm{n}}}/\xi_{\mathrm{s}}\right)/\sqrt{1-\alpha_{\mathrm{GB}}}$ in the thick junction limit. $F_{\mathrm{p}}^{\mathrm{max}}$ is found as usual at the field $b^* = p/(p+q)$. The empirical parameters A and r account for the fraction of the total vortex length that is held within grain boundaries.

Comparisons of Eq. (5.4.1) in the thick junction limit to our TDGL results are presented in Figs. 5.8 and 5.9. A, p and q were taken to be free parameters for each flux pinning curve, and $r = 1.1$ was obtained as a global fit parameter from the combined set of simulations. The maximum in the flux pinning force per unit volume, $F_{\mathrm{p}}^{\mathrm{max}}$, has been compared to a constrained form of Eq. (5.4.1) in Figs. 5.10 and 5.11, in which the pinning parameters are restricted to their Kramer-like values $p = 0.5$, $q = 2$. The decrease in critical current density as the grain boundary properties degrade (as $\sqrt{1 - \alpha_{\mathrm{GB}}}$ increases) in the weak coupling limit of grains appears to be well represented by Eq. (5.4.1) and $f(\alpha_{\mathrm{GB}})$ taken from Eq. (4.3.12). In this case, the parameters A and r are closely related to their 2D equivalents in Eq. (4.3.16), with $r \approx c_1 \approx 0.6$ and in the limit of strongly degraded grain boundaries, $A \approx c_0/3$, as shown by Fig. 5.11. The observation that the prefactor c_0 in the 2D junction simulations is approximately three times larger than the prefactor A in the 3D simulations here may partly be due to the stronger surface barrier existing in the junction system at the junction-insulator interface. The surface barrier at the grain-grain boundary interface in the 3D simulations is generally weaker as a result of the proximity effect limiting supercurrents at the interface, similar to the effect observed at metallic interfaces in Fig. 3.5.

For the polycrystal system in Table 5.1, which lies close to the peak $F_{\mathrm{p,max}}$ in Fig. 5.9, $J_{\mathrm{c}} \sim b^{-0.4}(1 - b)^{2.7}$ ($p = 0.6$, $q = 2.7$), close to the Kramer-like field dependence of the critical current density $J_{\mathrm{c}} \sim b^{-0.5}(1 - b)^2$ ($p = 0.5$, $q = 2$). Deviations of p and q from predictions can occur due to multiple pinning mechanisms contributing to J_{c} concurrently; indeed, videos of the simulated vortex state show vortex depinning from grain boundaries, line intersections, and triple points across the range of α_{GB} in Fig. 5.8.

It is important to note that all the polycrystalline simulations carried out in this work are in the high-κ limit, when the local magnetic field is equal to the applied magnetic field in the system at every point. Nevertheless, we expect the results to be qualitatively accurate for real systems of materials such as $\mathrm{Nb_3Sn}$, since the

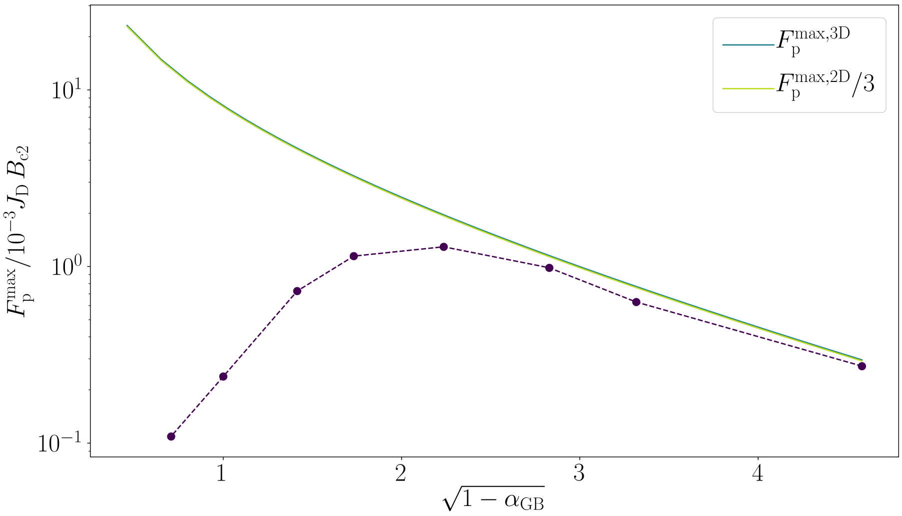

Figure 5.11: Maximum flux pinning force per unit volume $F_\mathrm{p}^{\mathrm{max}}/J_\mathrm{D}B_\mathrm{c2}$ as a function of $\sqrt{1-\alpha_\mathrm{GB}}$. Line fits are comparisons to Eq. (5.4.1) with $A = 0.25$, $r = 0.6$, $p = 0.5$ and $q = 2$, and to Eq. (4.3.14).

penetration depth in such materials $\lambda_\mathrm{s} \approx 100\,\mathrm{nm}$ is still of the order of the grain size [55], and so in high fields, magnetisation of grains will still be small relative to the applied magnetic field. The same is not necessarily true in very weak applied fields though, and thus care should be taken interpreting results in this regime as a result.

5.5 Conclusions

In this chapter, we have performed 3D simulations of equiaxed polycrystalline systems in the high κ limit, which we believe to be the first for a complex polycrystalline system to display an increase in the critical current density of the system with decreasing grain size in qualitative agreement with experiment [128].

We find that these TDGL simulations display maximum critical currents when the grain boundary thickness is similar to the effective coherence length in the grain boundary regions, at which point the field dependence of the critical current density

$J_c \approx b^{1/2}(1-b)^2$, as widely observed experimentally for commercial equiaxed polycrystalline Nb_3Sn. In this case, vortices display preferential motion along grain boundaries. These simulations also predict values for J_c in these systems within the same order of magnitude as those observed in experiment.

We have also suggested a new empirical flux pinning expression to parametrise these data based on current flow across Josephson junctions, and found this expression well describes decreases in critical current densities as grain boundaries degrade in the limit of weakly coupled grains over the range of simulations studied thus far. As a consequence of these simulations, we conclude that critical currents in these materials are primarily determined by the onset of vortex flow along grain boundaries.

Chapter 6

Future Work

In this thesis, we have presented a framework in which critical current densities in polycrystalline materials can be modelled and studied. Using TDGL simulations and analytic expressions, we have derived a foundation for future studies of current flow across grain boundary networks in technological materials.

Most directly, the critical current simulations of Chapter 5 can be repeated for different grain morphologies and materials. Of particular technological interest is whether systems of elongated grains along the direction of transport current with few continuous grain boundary channels in the direction of the Lorentz force give rise to $F_{\mathrm{p}} \sim b(1-b)$, as observed in commercial NbTi samples which share this grain morphology [117]. Such flux pinning behaviour has previously been attributed to vortices depinning from grain boundaries and crossing grains in such materials, in contrast to the flux-shear behaviour along grain boundaries in $\mathrm{Nb_3Sn}$. If these explanations are correct, one could investigate how the flux-pinning behaviour crosses over to the $F_{\mathrm{p}} \sim b^{1/2}(1-b)^2$ behaviour in the equiaxed system by tuning the grain anisotropies between the elongated and equiaxed cases.

None of the simulations presented in this thesis have included pinning structures within grains, such as inclusions, precipitates, or disordered regions that may form during growth of the polycrystal or be introduced by damage after formation. These structures will contribute to pinning of vortices in addition to the grain boundary effects that have been the focus here. Such pinning structures can easily be added to these simulations in the form of regions in which $\alpha_{\mathrm{n}} < 1$ [129]. Of special interest for fusion applications is the role of pinning structures and crystal defects introduced by radiation damage, such as collision cascades. Such pinning structures can significantly contribute to achievable critical currents in such materials, but the role of defect migration to grain boundaries on their properties in operational conditions remains poorly understood.

The approach used to generate grain morphologies in Chapter 5 using *Neper* can also track orientations of grains, and restrict the distribution of grain orientations in the system. This could be useful for studies of the role of grain boundaries limiting critical currents in HTS tapes, in which the critical current density across a boundary decreases exponentially with the misorientation angle θ_{gg} between grains [130]. Considering Eq. (4.3.12), this behaviour could be modelled within the existing framework with an ansatz that $\theta_{\mathrm{gg}} \propto \sqrt{1-\alpha_{\mathrm{GB}}}$, and could help elucidate the crossover between critical currents limited by current flow across grain boundaries in these systems, and those limited by intragranular pinning structures. Electronic structure modelling of this exponential decrease of critical currents with misorientation angle at grain boundaries in *d*-wave superconductors like YBCO, such as that presented in [131], may help further guide future simulations, particularly those regarding the role of charge inhomogeneities at grain boundary interfaces in limiting critical currents.

A necessary limitation of using TDGL theory for these studies is that the input parameters α, β and m are phenomenological parameters, whose absolute values are unknown for a given material. Advances in density functional theory and electronic structure analysis, such as those presented in [132], may help constrain these phenomenological parameters for simple superconducting systems using first-principles methods. Direct experimental comparisons such will also help constrain these parameters further, developing towards the goal of quantitatively predictive critical current simulations in common technological materials. One particularly exciting extension of this work would be to take grain morphologies and microstructures directly measured in experiment for a given superconducting sample and compare them to the critical current densities predicted by TDGL-HIK. A similar approach has been applied in [90] to provide quantitative predictions for J_c in YBCO samples doped with Dy nanoparticles.

Analytic models of the critical current density of these large-scale polycrystalline materials remain difficult to obtain for the reasons given in Chapter 5. Future work should consider if the approach from [94] for 2D Josephson junction systems can be extended to predict critical currents across 3D convex polyhedral grains, in the similar weak coupling, high κ limit in low fields. This may help develop our understanding of the grain size dependencies observed in Chapter 5 and in experiment. Furthermore, more work is needed on the crossover between the weak coupling and strong coupling limit between grains; the results in Chapter 5 suggest that the flux pinning behaviour most commonly observed in experimental samples of $\mathrm{Nb_3Sn}$ occurs close to this crossover point. Necessarily, such analytic models will need to accommodate the crossover between vortex depinning from grain boundaries and vortex shear along them, as grains become more weakly coupled.

Finally, it would be desirable to extend the large-scale polycrystalline simulations presented here to accommodate systems with finite κ, and thus with finite penetration depth λ. This would be necessary for the study of effects arising from shielding of the external magnetic field in the interior of grains; particularly important for simulations of large-grained systems in low fields. A stable, large-scale solver for the TDGL equations for finite λ is therefore desirable to this end. For low κ simulations, the explicit solver of [65] is suitable, but is limited to extremely short time steps for large κ as discussed in Chapter 3. Similarly, extending TDGL-HIK to accommodate arbitrary finite penetration depths is also not easily possible without significant detrimental effects on performance, due to the extra complexity in requiring the solution of the magnetic field distribution at every time step. Further work is needed to determine how, or if, a solver such as this can be developed with the required accuracy and performance required for critical current simulations.

APPENDIX A

Jacobi Elliptic Functions

The results in Chapter 4 make use of the Jacobi elliptic functions as solutions to the Ginzburg–Landau equations in junction systems. We shall include their basic definitions and properties here for convenience. The Jacobi elliptic functions $\mathrm{sn}(z,k)$, $\mathrm{cn}(z,k)$, and $\mathrm{dn}(z,k)$ of argument z and modulus k satisfy the relations [110]

$$\mathrm{sn}^2\left(z,k\right)+\mathrm{cn}^2\left(z,k\right)\equiv k^2\mathrm{sn}^2\left(z,k\right)+\mathrm{dn}^2\left(z,k\right)\equiv 1. \tag{A.0.1}$$

For $0\leq k\leq 1$ they can be related to the usual trigonometric functions via the Jacobi amplitude function $\mathrm{am}\left(z,k\right)$ via

$$\begin{aligned}\mathrm{sn}\left(z,k\right)&=\sin\left(\mathrm{am}\left(z,k\right)\right),\\ \mathrm{cn}\left(z,k\right)&=\cos\left(\mathrm{am}\left(z,k\right)\right),\\ \mathrm{dn}\left(z,k\right)&=\sqrt{1-k^2\sin^2\left(\mathrm{am}\left(z,k\right)\right)}.\end{aligned} \tag{A.0.2}$$

A shorthand notation is often used for ratios of Jacobi elliptic functions, where

$$\mathrm{pq}\left(z,k\right)=\frac{\mathrm{pr}\left(z,k\right)}{\mathrm{qr}\left(z,k\right)}, \tag{A.0.3}$$

with $\mathrm{p},\mathrm{q},\mathrm{r}\in\{\mathrm{s},\mathrm{d},\mathrm{c},\mathrm{n}\}$ and $\mathrm{np}\left(z,k\right)=1/\mathrm{pn}\left(z,k\right)$. Finally, it is also useful to also to define the (related) complete elliptical of the first kind $K(k)$ and the incomplete elliptical of the second kind $E(z,k)$, [110]

$$E(z,k)=\int_0^z\sqrt{1-k^2\sin^2\theta}\;\mathrm{d}\theta, \tag{A.0.4}$$

$$K(k) = \int_0^{\pi/2} \frac{\mathrm{d}\theta}{\sqrt{1 - k^2 \sin^2 \theta}}, \tag{A.0.5}$$

that are used in [50, 112].

Bibliography

[1] H. K. Onnes, Communications from the Physical Laboratory of the University of Leiden **124C**, 21 (1911).

[2] J. J. Hamlin, Physica C: Superconductivity and its Applications **514**, 59 (2015).

[3] J. G. Bednorz and K. A. Müller, Zeitschrift für Physik B Condensed Matter **64**, 189 (1986).

[4] M. K. Wu, J. R. Ashburn, C. J. Torng, P. H. Hor, R. L. Meng, L. Gao, Z. J. Huang, Y. Q. Wang, and C. W. Chu, Physical Review Letters **58**, 908 (1987).

[5] E. Snider, N. Dasenbrock-Gammon, R. McBride, M. Debessai, H. Vindana, K. Vencatasamy, K. V. Lawler, A. Salamat, and R. P. Dias, Nature **586**, 373 (2020).

[6] S. Hahn, K. Kim, K. Kim, X. Hu, T. Painter, I. Dixon, S. Kim, K. R. Bhattarai, S. Noguchi, J. Jaroszynski, and D. C. Larbalestier, Nature **570**, 496 (2019).

[7] E. Moser, E. Laistler, F. Schmitt, and G. Kontaxis, Frontiers in Physics **5**, 33 (2017).

[8] J. Minervini, M. Parizh, and M. Schippers, Superconductor Science and Technology **31**, 030301 (2018).

[9] E. D. Becker, Analytical Chemistry **65**, 295A (1993).

[10] J. Ongena, R. Koch, R. Wolf, and H. Zohm, Nature Physics **12**, 398 (2016).

[11] P. Bruzzone, Superconductor Science and Technology **28**, 024001 (2014).

[12] P.-H. Rebut, Fusion Engineering and Design **27**, 3 (1995).

[13] A. J. Creely, M. J. Greenwald, S. B. Ballinger, D. Brunner, J. Canik, J. Doody, T. Fülöp, D. T. Garnier, R. Granetz, T. K. Gray, and et al., Journal of Plasma Physics **86**, 865860502 (2020).

[14] D. Whyte, Philosophical Transactions of the Royal Society A: Mathematical, Physical and Engineering Sciences **377**, 20180354 (2019).

[15] M. Tinkham, "Magnetic Properties of Classic Type II Superconductors," in *Introduction to Superconductivity* (Dover Publications, New York, 1996) pp. 149–154, 2nd ed.

[16] H. Fröhlich, Physical Review **79**, 845 (1950).

[17] L. N. Cooper, Physical Review **104**, 1189 (1956).

[18] J. Bardeen, L. N. Cooper, and J. R. Schrieffer, Physical Review **108**, 1175 (1957).

[19] R. D. Parks, "Equilibrium Properties: Comparison of Experimental Results with Predictions of the BCS Theory," in *Superconductor Science & Technology*, Vol. 1 (Dekker, New York, 1969) pp. 119–191.

[20] Y. J. Uemura, Journal of Physics: Condensed Matter **16**, S4515 (2004).

[21] A. Bussmann-Holder and H. Keller, Zeitschrift für Naturforschung B **75**, 3 (2020).

[22] D. R. Tilley and J. Tilley, "Ginzburg-Landau Theory," in *Superfluidity and Superconductivity* (IOP, Bristol, 1990) pp. 296–302, 3rd ed.

[23] P. G. De Gennes, *Superconductivity of Metals and Alloys* (Perseus Books Group, Boulder, Colorado, 1999).

[24] C. P. Poole, H. A. Farach, and R. J. Creswick, "Zero-Field Case Near Superconductor Boundary," in *Superconductivity* (Academic Press Inc, San Diego, California, 2007) p. 149.

[25] V. L. Ginzburg and L. D. Landau, Zhurnal Eksperimentalnoj i Teoreticheskoj Fiziki **20**, 1064 (1950).

[26] L. P. Gor'kov, Soviet Physics JETP **9**, 1364 (1959).

[27] P. G. De Gennes, Reviews of Modern Physics **36**, 225 (1964).

[28] K. Maki, Physics **1**, 127 (1964).

[29] K. Maki, Physics **1**, 21 (1964).

[30] A. Schmid, Physik der Kondensierte Materie **5**, 302 (1966).

[31] L. P. Gor'kov and G. M. Eliashberg, Soviet Physics JETP **27**, 328 (1968).

[32] L. D. Landau and E. M. Lifshitz, *Statistical Physics Pt. 1*, 3rd ed., Course of Theoretical Physics (Pergamon Press, Oxford, 1980).

[33] M. Greiter, Annals of Physics **319**, 217 (2005).

[34] E. M. Lifshitz and L. P. Pitaevskii, *Statistical Physics Pt. 2*, Course of Theoretical Physics (Pergamon Press, Oxford, 1980).

[35] C. P. Poole, H. A. Farach, and R. J. Creswick, "Type II Superconductivity," in *Superconductivity* (Dover Publications, New York, 2007) pp. 337–384.

[36] B. Rosenstein and D. Li, Reviews of Modern Physics **82**, 109 (2010).

[37] A. V. Dmitriev and W. Nolting, Superconductor Science and Technology **17**, 443 (2004).

[38] O. Narayan and A. P. Young, American Journal of Physics **73**, 293 (2005).

[39] N. B. Kopnin, *Theory of Nonequilibrium Superconductivity* (Oxford Univ. Press, Oxford, 2009).

[40] A. A. Abrikosov, Soviet Physics JETP **5**, 1174 (1957).

[41] C.-R. Hu, Physical Review B **6**, 1756 (1972).

[42] E. H. Brandt, Physical Review Letters **78**, 2208 (1997).

[43] W. H. Kleiner, L. M. Roth, and S. H. Autler, Physical Review **133**, A1226 (1964).

[44] D. Saint-James and P. Gennes, Physics Letters **7**, 306 (1963).

[45] F. E. Harper and M. Tinkham, Physics Review **172**, 441 (1968).

[46] D. R. Tilley, Proceedings of the Physical Society **85**, 1177 (1965).

[47] L. Gor'kov and T. Melik-Barkhudarov, Soviet Physics JETP **18** (1964).

[48] R. Zaitsev, Zhurnal Eksperimental'noi i Teoreticheskoi Fiziki (USSR) For English translation see Sov. Phys.-JETP (Engl. Transl.) **50** (1966).

[49] T. Matsushita, Journal of the Physical Society of Japan **51**, 2755 (1982).

[50] H. J. Fink, Physical Review B **14**, 1028 (1976).

[51] M. Cyrot, Reports on Progress in Physics **36**, 103 (1973).

[52] C.-R. Hu and R. S. Thompson, Physical Review B **6**, 110 (1972).

[53] P. Lipavský, J. Koláček, K. Morawetz, and E. H. Brandt, Physics Review B **65**, 144511 (2002).

[54] I. A. Sadovskyy, A. E. Koshelev, C. L. Phillips, D. A. Karpeyev, and A. Glatz, Journal of Computational Physics **294**, 639 (2015).

[55] G. Wang, M. J. Raine, and D. P. Hampshire, Superconductor Science and Technology **30**, 104001 (2017).

[56] J. W. Ekin, *Experimental Techniques for Low-Temperature Measurements* (Oxford University Press, New York, 2007).

[57] D. Dew-Hughes, Philosophical Magazine **30**, 293 (1974).

[58] W. A. Fietz and W. W. Webb, Physical Review **178**, 657 (1969).

[59] E. J. Kramer, Journal of Applied Physics **44**, 1360 (1973).

[60] D. Dew-Hughes, Low Temperature Physics **27**, 713 (2001).

[61] T. Matsushita, "Flux Pinning Characteristics," in *Flux Pinning in Superconductors* (Springer, Berlin, Heidelberg, 2007) pp. 267–339.

[62] E. J. Kramer, Journal of Applied Physics **49**, 742 (1978).

[63] E. H. Brandt, Reports on Progress in Physics **58**, 1465 (1995).

[64] A. I. Larkin and Y. N. Ovchinnikov, Journal of Low Temperature Physics **34**, 409 (1979).

[65] W. D. Gropp, H. G. Kaper, G. K. Leaf, D. M. Levine, M. Palumbo, and V. M. Vinokur, Journal Comput Phys **123**, 254 (1996).

[66] Q. Du, Mathematics of Computation **67**, 965 (1998).

[67] Q. Du, Journal of Mathematical Physics **46**, 095109 (2005).

[68] *COMSOL Multiphysics Reference Guide* (2015).

[69] I. G. de Oliveira, Physics Letters A **379**, 1486 (2015).

[70] B. Oripov and S. M. Anlage, Physical Review E **101**, 033306 (2020).

[71] H. Gao and W. Sun, Journal of Computational Physics **294**, 329 (2015).

[72] A. R. Pack, J. Carlson, S. Wadsworth, and M. K. Transtrum, Physics Review B **101**, 144504 (2020).

[73] Q. Du and L. Ju, Journal of Computational Physics **201**, 511 (2004).

[74] T. Winiecki and C. S. Adams, Journal of Computational Physics **179**, 127 (2002).

[75] G. J. Carty and D. P. Hampshire, Superconductor Science and Technology **26**, 065007 (2013).

[76] G. J. Carty, M. Machida, and D. P. Hampshire, Physical Review B **71**, 144507 (2005).

[77] A. I. Blair and D. P. Hampshire, IEEE Transactions on Applied Superconductivity **28**, 1 (2018).

[78] W. F. Ames, *Numerical Methods for Partial Differential Equations* (Academic Press Inc., San Diego, 1992).

[79] O. Schenk and K. Gärtner, Future Generation Computer Systems **20**, 475 (2004).

[80] W. H. Press, B. P. Flannery, S. A. Teukolsky, and W. T. Vetterling, *Numerical Recipes in Fortran: The Art of Scientific Computing*, 2nd ed. (Cambridge University Press, 1992).

[81] G. J. Carty and D. P. Hampshire, Physical Review B **77**, 172501 (2008).

[82] I. A. Sadovskyy, A. E. Koshelev, W.-K. Kwok, U. Welp, and A. Glatz, Proceedings of the National Academy of Sciences **116**, 10291 (2019).

[83] J. Nickolls, I. Buck, M. Garland, and K. Skadron, Queue **6**, 40 (2008).

[84] G. P. Papari, A. Glatz, F. Carillo, D. Stornaiuolo, D. Massarotti, V. Rouco, L. Longobardi, F. Beltram, V. M. Vinokur, and F. Tafuri, Scientific Reports **6**, 38677 (2016).

[85] J. Barba-Ortega, A. Becerra, and J. Albino Aguiar, Physica C: Superconductivity **470**, 225 (2010).

[86] M. Machida and H. Kaburaki, Physical Review Letters **71**, 3206 (1993).

[87] J. J. Barba, C. C. de Souza Silva, L. R. E. Cabral, and J. Albino Aguiar, Physica C: Superconductivity and its Applications **468**, 718 (2008).

[88] M. Tinkham, *Introduction to Superconductivity*, 2nd ed. (McGraw-Hill Book Co., Singapore, 1996) pp. 110–147.

[89] G. R. Berdiyorov, A. R. de C. Romaguera, M. V. Milošević, M. M. Doria, L. Covaci, and F. M. Peeters, The European Physical Journal B **85**, 130 (2012).

[90] I. A. Sadovskyy, A. E. Koshelev, A. Glatz, V. Ortalan, M. W. Rupich, and M. Leroux, Physical Review Applied **5**, 014011 (2016).

[91] T. Boutboul, V. Abaecherli, G. Berger, D. P. Hampshire, J. Parrell, M. J. Raine, P. Readman, B. Sailer, K. Schlenga, M. Thoener, E. Viladiu, and Y. Zhang, IEEE Trans Appl Super **26**, 1 (2016).

[92] B. Josephson, Physics Letters **1**, 251 (1962).

[93] D. Jacobson, Physical Review **138**, A1066 (1965).

[94] J. R. Clem, Physics Review B **81**, 144515 (2010).

[95] M. Moshe, V. G. Kogan, and R. G. Mints, Physics Review B **78**, 020510 (2008).

[96] B. D. Josephson, Advances in Physics **14**, 419 (1965).

[97] P. A. Rosenthal, M. R. Beasley, K. Char, M. S. Colclough, and G. Zaharchuk, Applied Physics Letters **59**, 3482 (1991).

[98] C. S. Owen and D. J. Scalapino, Physical Review **164**, 538 (1967).

[99] A. Gurevich and L. D. Cooley, Physical Review B **50**, 13563 (1994).

[100] J. McDonald and E. Barzi, IEEE Transactions on Applied Superconductivity **11**, 3884 (2001).

[101] J. R. Clem, Physics Review B **84**, 134502 (2011).

[102] G. R. Berdiyorov, M. V. Milošević, L. Covaci, and F. M. Peeters, Physics Review Letters **107**, 177008 (2011).

[103] G. Kimmel, I. A. Sadovskyy, and A. Glatz, Physical Review E **96**, 013318 (2017).

[104] A. E. Koshelev, I. A. Sadovskyy, C. L. Phillips, and A. Glatz, Physical Review B **93**, 060508 (2016).

[105] F. S. Bergeret and J. C. Cuevas, Journal of Low Temperature Physics **153**, 304 (2008).

[106] J. C. Cuevas and F. S. Bergeret, Physical Review Letters **99**, 217002 (2007).

[107] J. C. Hammer, J. C. Cuevas, F. S. Bergeret, and W. Belzig, Physics Review B **76**, 064514 (2007).

[108] A. Volkov, Zh. Eksp. Teor. Fiz **66**, 758 (1974).

[109] F. Sols and J. Ferrer, Physical Review B **49**, 15913 (1994).

[110] F. W. J. Olver, D. W. Lozier, R. F. Boisvert, and C. W. Clark, *NIST Handbook of Mathematical Functions* (Cambridge University Press, 2010).

[111] A. Barone and G. Paterno, *Physics and Applications of the Josephson Effect* (Wiley, New York, 1982).

[112] S. V. Kuplevakhsky and A. M. Glukhov, Physical Review B **76**, 174515 (2007).

[113] F. Chiodi, M. Ferrier, S. Guéron, J. C. Cuevas, G. Montambaux, F. Fortuna, A. Kasumov, and H. Bouchiat, Physical Review B **86**, 064510 (2012).

[114] L. Angers, F. Chiodi, G. Montambaux, M. Ferrier, S. Guéron, H. Bouchiat, and J. C. Cuevas, Physical Review B **77**, 165408 (2008).

[115] A. A. Abrikosov, Soviet Physics JETP **20**, 480 (1965).

[116] C. Senatore, C. Barth, M. Bonura, M. Kulich, and G. Mondonico, Superconductor Science and Technology **29**, 014002 (2016).

[117] D. Dew-Hughes, Philosophical Magazine B **55**, 459 (1987).

[118] A. I. Blair and D. P. Hampshire, IEEE Transactions on Applied Superconductivity **29**, 1 (2019).

[119] T. Luther and C. Könke, Engineering Fracture Mechanics **76**, 2332 (2009).

[120] R. Quey, P. R. Dawson, and F. Barbe, Computer Methods in Applied Mechanics and Engineering **200**, 1729 (2011).

[121] J. Jordan, *pyvoro 2D and 3D Voronoi tessellations: a python entry point for the voro++ library* (`https://github.com/joe-jordan/pyvoro`, 2014).

[122] C. H. Rycroft, Chaos: An Interdisciplinary Journal of Nonlinear Science **19**, 041111 (2009).

[123] R. Quey and L. Renversade, Computer Methods in Applied Mechanics and Engineering **330**, 308 (2018).

[124] S. Posen, J. Lee, D. N. Seidman, A. Romanenko, B. Tennis, M. Oleksandr, and D. Sergatskov, Superconductor Science and Technology (2020).

[125] P. Sunwong, J. Higgins, Y. Tsui, M. Raine, and D. P. Hampshire, Superconductor Science and Technology **26**, 095006 (2013).

[126] L. A. Bonney, T. C. Willis, and D. C. Larbalestier, Journal of Applied Physics **77**, 6377 (1995).

[127] S. A. Keys and D. P. Hampshire, Superconductor Science and Technology **16**, 1097 (2003).

[128] W. Schauer and W. Schelb, IEEE Transactions on Magnetics **17**, 374 (1981).

[129] A. Glatz, I. A. Sadovskyy, U. Welp, W.-K. Kwok, and G. W. Crabtree, Journal of Superconductivity and Novel Magnetism **33**, 127 (2020).

[130] H. Hilgenkamp and J. Mannhart, Reviews of Modern Physics **74**, 485 (2002).

[131] S. Graser, P. J. Hirschfeld, T. Kopp, R. Gutser, B. M. Andersen, and J. Mannhart, Nature Physics **6**, 609 (2010).

[132] P. Garg, C. Muhich, L. D. Cooley, T. R. Bieler, and K. N. Solanki, Physical Review B **101**, 184102 (2020).